UNIVERSITA’ DEGLI STUDI DI PAVIA

Dottorato Di Ricerca in Ingegneria Elettronica, Informatica ed Elettrica

Ciclo XXXI
2015-2018

Tunable Microwave Components based on Few Layer Graphene

Doctoral Thesis of

MUHAMMAD YASIR

Tutor:
Professor Maurizio Bozzi

Dedicated to my wonderful family

Contents

Chapter 1
Introduction

1.1 Evolution of Graphene

Graphene in its current form has not been known until very recently. It is graphite that has long been in the use of mankind for several applications. Graphite is composed of several layers of graphene stacked on top of each other. It would not be wrong to say that graphene is a two-dimensional form of its 3D counterpart, graphite. Graphite has remained in use for thousands of years [1]. Graphite has been mined in the sixteenth century in England. The term graphite means writing in Greek, a name given to it by the German scientist, Verner in 1789. Graphite has been used in pencils since 18th century. Due to its layered morphology, graphite has been used as a solid lubricant. The different layers slide over each other because of weak dispersion forces between them. These individual layers are actually graphene layers.

Graphene is composed of carbon atoms attached to each other in a honeycomb like crystal lattice. It is a basic building block of several graphitic materials like fullerenes, carbon nanotubes and graphite. The bond length between adjacent atoms in graphene is 0.142 nm. The height of the graphene layer has been measured to be 0.33 nm as depicted in the Fig. 2. It is the thinnest and the strongest material known. The strength measures laterally along the individual layer since vertically it is very weak. Graphene is transparent to light and possess a structure so dense that even the smallest helium atom does not pass through it. It is a perfect heat conductor and have electrical conductivity parallel to that of copper.

Over the years graphene has advanced up to a great extent. The term graphene can be dated back to 1987, which was used to describe an individual sheet of graphite. Yet older in the year 1859 is when a British chemist, Benjamin Bordie prepared woven paper constituting graphene oxide layer. The study of this graphene oxide paper was completed by Kohlschutter and Haenni in 1919. By as old as 1930 as found by the scientist Landau, it was believed that thermodynamics prevent the formation of 2D crystal of graphene as a molecule with single atomic layer. The first study of the electronic properties of graphite was performed by Wallace in 1947 in which he proposed a band theory and found out that graphite was a semiconductor with zero activation energy. It was he who found out that the conduction is 100 times more in parallel as compared to across the planes. A year later, the first TEM (transmission Electron Microscopy) image of few layer graphene was published by Ruess and Vogt. In 1960, it was Ubbelohde and Lewis who isolated a single atom layer graphite to find that a monolayer of graphene possesses a high basal-plane conductivity.

They also found out that graphite is composed of layers, each consisting of hexagonal rings of carbon atoms. TEM and XRD(X-ray diffraction) was collectively used to study single graphene sheet by Hanns-Peter Boehm in 1961. The term graphene was formally given in a report to the international Union of pure and applied Chemistry (IUPAC) by Boehm. The forty years that followed were when a great expanse of theoretical and experimental research was performed in various directions but the main concern was the acquisition of superior electrical properties from thin graphite or graphene layers. In the forty years from the sixties to the end of the century several breakthroughs were made in order to grow monolayer graphite or graphene. Hess and Ban in 1966 were the first to use chemical vapor deposition (CVD) to grow graphene in which carbon atoms were provided through a gas source. However, epitaxial growth of graphene has been the most viable solution for electronic applications. The problem in epitaxial growth as identified theoretically by Semenoff in 1984 is that there is an alteration in the electronic structure due to charge transfer from the substrate.

Due to high electron mobility and very high thermal conductivity graphite was used in industrial furnaces in 2001. The first intercalation of graphite for individuating single graphene layers was performed by Dresselhaus in 2002. The intercalating substances could be removed by chemical reactions as demonstrated by Shioyama and Hirata in 2001 and 2004 respectively. It was in 2004 that Andre Geim and Novoselov [2] extracted single atom thick graphene layer. The extraction was done by the subsequent application of scotch tape to graphite until the number of layers of graphene have been reduced to a single layer. The scotch tape in the last step is detached by the help of acetone. Even with a single layer graphene there are no dislocations and empty vacancies in the crystal lattice. It can be termed as an almost perfect crystal lattice. This lets graphene have excellent electronic properties since in graphene the conducting electrons move with a velocity close to the speed of light. An electric field study was performed in [2] in which a backgate in the form of SiO_2 was used to change the charge density. It was also demonstrated that graphene acts as a zero-gap semiconductor and that it possesses a very simple electronic spectrum. A rapid increase in research on graphene follows since [2]. In electronics applications, one of the many reasons is the fact that silicon has reached its fundamental technological limits of almost 10 nanometers, graphene has always been looked to as a replacement to silicon for use in high frequency electronics. For the work performed in [2], a noble prize was awarded in 2010. Since 2010 a lot of various milestones have been reached in research on graphene.

In 2010, particularly important is the introduction of tunable electrical bandgap in graphene by IBM researchers. Graphene has been considered a bandgap-less material and unlike silicon has a very low on/off ratio. It is hoped that graphene would someday substitute conventional metal oxide-based field effect transistors. Attempts were also made to increase the operating frequency of graphene transistors, first up to 100 GHz and then 155 and 300 GHz by the help of nanowire as a back gate. The aim is to increase the frequency of graphene transistors up to 1THz. An explosion in Research in both RF and THz has occurred subsequently.

1.2 Potential

The interesting properties of graphene brings it great potential for a wide range of applications. It possesses a very high carrier mobility of almost 200000 $cm^2 V^{-1} s^{-1}$ compared to 1400 $cm^2 V^{-1} s^{-1}$ of silicon and 77000 $cm^2V^{-1}s^{-1}$ of indium antimonide. This is the highest carrier mobility among all the semiconductors. It can also support very large current density of up to 10^8 A cm^{-2}. This enables it to be employed in transistors and various sensing applications [3]. There is a small overlap between the conduction and valence band at ambient condition which enables graphene to control both positive and negative charge carriers of very high concentrations. Added to this is the fact that it has a very distinctive electronic structure. The fermi energy level lies between the conduction and valence band which means a very low conductivity. However, an electric field can be used to make graphene n-doped or p-doped according to the polarity of the applied field. This makes it highly conductive [4] and hence tunable and bipolar. Another interesting feature of the 2D honeycomb lattice of graphene in which carbon atoms are tightly packed to each other is that it makes electrons move at the speed of light and they behave as if they are massless [5]. A combination of the atomic properties of graphene as discussed formerly brings it great potential in the fields of Terahertz and Microwaves.

1.3 Applications

1.3.1 Terahertz

As formerly described, graphene carries very interesting electronic properties. These properties are mainly due to the 2D nature and the distribution of carbon atoms in a particular manner. Conventionally, semiconductors are used in electronics which are bulky and do not have a linear relation between the energy and momentum (E-k). In graphene, however the E-k relation is linear and charge carriers behave as massless dirac fermions. In addition to these remarkable electronic properties, graphene also possesses very interesting optoelectronic properties, one of the main of which is its broadband optical absorption. This optical absorption can be used to excite the intraband transition of graphene thus providing a possibility to tune its conductivity in the terahertz regime [6], [7]. A combination of the optoelectronic properties with its very unique electronic properties tends to give it a wide range of terahertz applications.

Graphene has been widely used as terahertz modulator due to a wide variation in its conductivity. Graphene has been used in both Electrically and optically excited configurations in the terahertz regime. In the case of electrically excited terahertz modulators, a gate voltage is applied between graphene layer and silicon substrate in the form of an FET (field effect transistor) to tune the fermi energy level and a modulation depth of 15% is acquired [8]. In the case of optically excited modulator [9], graphene is deposited on silicon and higher values of modulation are achieved at a broad band.

At Terahertz frequencies graphene is also used in emitters. Conventionally at terahertz frequencies, the different emitters proposed are based on photoconductive antennas, nonlinear electro optic crystals and air plasma [7]. These emitters are limited by their intensities and efficiency. Therefore, graphene has been used in novel emitters in three basic configurations. The use of Graphene in hetero structure to optically pump terahertz radiation by the help of an optical cavity. Multiple graphene layered structure has been used to optically pump terahertz radiation through metal slot line or dielectric waveguide. In a third configuration, tunable and adjustable plasmons generated by the help of electron hole recombination in suspended graphene layers through metallic stripline electrodes.

At terahertz, detectors are generally characterized by their noise equivalent power (NEP) and detectivity values. Conventional Terahertz detectors face problems of sensitivity to background radiations, temperature fluctuations, mechanical vibrations and electrical interference. Furthermore, there is performance degradation in the upper terahertz range. These issues can be sorted out by deploying mono and bi-layer graphene FET devices. A top-gate coupled antenna configuration is used in which excitation of overdamped waves is detected [7].

1.3.2 Microwaves

At the microwave and millimeter wave frequency unlike the terahertz frequencies, there is an increase in the sample size. This increase in sample size from micro to mm and cm increases the mean free path and hence the ballistic condition is no more valid. This drastically reduces the carrier mobilities at such frequencies. Even though there is this drawback of the reduced carrier mobility at microwave frequencies, still the interesting property of bipolarity and tunability of conductivity remains intact. The phenomenon of taking the fermi energy level from the conduction to the valence band by the application of a voltage bias is still present. The electron and hole start to overtake the current transport and hence the resistance of the sample is drastically reduced. This phenomenon has been widely exploited in several microwave applications [10].

Silicon has already been considered to hit its limits in the quest for going higher and higher in frequencies. This makes it highly desirable to look for alternative materials for devices and transistors. Graphene based FET have reached a cutoff frequency of 300GHz in the case of GaN nanowire-based gate [11]. Formerly GFETs have achieved cutoff frequencies of 160GHz using conventional semiconductor fabrication techniques. Graphene, however have been deemed unsuitable for use in digital electronics due to an absence of bandgap. This drawback can be overcome by cutting graphene nanoribbons of a smaller dimension to introduce a bandgap in graphene. High frequency graphene FETs have already been produced by this technique [12].

In antenna applications in the microwave/mm range of frequencies the use of graphene is a bit tricky. In such applications multiple wavelength dimensions are required. Conventional methods of graphene fabrication produce smaller dimensions which are hard to cover such requirements but CVD (chemical vapor deposition) grown graphene can be used to cover larger areas. Another problem in implementing graphene directly for antenna applications is its low conductivity values as compared to copper. This can degrade the efficiency of antenna applications. An attempt in making such antennas has been made in [13] The antenna efficiency is low but it covers a large bandwidth. Graphene, however can be used in combination to other microwave passive circuitry in order to produce tunable or steerable antennas. An attempt of tunable antenna based on graphene has been reported in [14].

Graphene can be easily implemented in other passive microwave applications for instance attenuators, phase shifters and modulators. For these applications, since large quantities of depositions of graphene are required therefore graphene nanoflakes have been used. Here like other microwave applications the tunable conductivity has been exploited since it is also applicable at the micro/mm wave range of frequencies. In [15] a wideband tunable attenuator based on microstrip lines and graphene is shown. It is shown that the conductivity of graphene can be electronically tuned to vary the insertion loss of the attenuator. Several attempts were made afterwards to improve the characteristics of the attenuator.

Exploitation of novel properties of graphene in EMI shielding applications is not new. It is a high impact area ranging from automotive to aerospace and electronics. Graphene is usually deployed in the form of nanocomposites for such application since the production of vast dimensions as required by such application in its pure state is impractical. Graphene can be used as a filler since it bears excellent electrical properties. It has a high aspect ratio, large surface area since it is 2D and possess very good thermal and mechanical properties which is an added benefit [16].

1.4 Summary of this thesis

In this doctoral thesis an effort is made to advance the state of the art of the microwave applications of graphene. The tunable resistive properties of graphene at microwave frequencies are exploited in order to propose microwave passive components. Several microwave passive components are designed, optimized and fabricated. Graphene flakes are deposited on the fabricated microwave components and they are characterized for their respective applications. The measured data is compared to conventional microwave components and it is demonstrated that graphene-based components does prove to have parallel if not better functionality.

A chapter wise breakdown of this thesis is as follows.

In the second chapter a profound discussion on graphene is provided. The physics behind graphene, its molecular structure and atomic distribution is discussed. A brief discussion on synthesis and properties of few layer graphene is provided. The interesting electrical, mechanical and thermal properties resulting from the atomic structure is provided. Electronic properties of graphene are briefly discussed and based on it, the terahertz and microwave applications are discussed in detail. In terahertz, a detailed description of terahertz emitter, detector and modulator is provided. Finally, the microwave applications of graphene are discussed in detail with specific emphasis on graphene FETs, microwave components and EMI shielding applications.

The third chapter revolves around tunable attenuators based on few-layer graphene. A preliminary design of the attenuator based on a simple microstrip line with gap is discussed. The properties including insertion loss and return loss are discussed. An improvement in the attenuator based on a change in its topology is described. This improved version is based on graphene flakes attached to parallel grounded vias on the side of a microstrip line. An improvement in the insertion loss and return loss is reported. A detailed analysis based on the number of vias and the length and width of the mid-section of the microstrip line is reported subsequently and results for each configuration are reported.

An effort is made to analyze the change in the resistance of graphene and translate it into a change in reactance in the fourth chapter. The change is reactance is a result of an optimum length and width of a stub so as to mitigate the resistance change and accentuate the reactance change caused by the stub. The stub is connected to a two port microstrip line through a tapered line. This concept has been used in designing phase shifter. Multiple such configurations are connected in parallel to maximum the phase shift.

In the fifth chapter, the concept of reactance changed is applied to a patch antenna. The reactance change can mimic a varactor diode, which is conventionally used to tune the radiating frequency of patch antennas. To this aim, a patch antenna is designed, which is connected to a stub through graphene. The current flowing through the stub is controlled by the help of graphene to electronically tune the radiating frequency of the patch antenna. It is made sure to minimize the effects of the proposed design on the gain efficiency values of the antenna.

Finally, in the last chapter a conclusion is derived based on the concepts of the attenuator and phase shifter. A combination of the two could result in a complete system in the form of a modulator. A desired phase and amplitude can be achieved by biasing specified points on a circuit. In this way a grid with specified amplitude and degrees can be completed. A detailed description of the modulator design is also provided in the Appendix A. Since microwave applications are discussed therefore, a description of an energy harvester based on graphene self-switching diode is discussed in detail in the Appendix B.

Chapter 2

Graphene: State of the Art

2.1 Physics

Graphene is a single layer of carbon atoms attached to each other in a honeycomb lattice. The carbon atoms in the honey comb lattice are sp^2 hybridized. Carbon has six electrons and is the sixth element of the periodic table. The distribution of electrons in the various orbitals henceforth results as: $1s^2\ 2s^2\ 2p_x^1\ 2p_y^1\ 2p_z^0$. The energy levels of all the p orbitals are the same but the p_z is shown even though it is empty, just for the sake of convention. The energy level distribution is as shown in the Figure 1 [1]. The four electrons in the valence shell result in *sp*, sp^2 and sp^3 hybridizations, which is very unique of carbon. The different hybridizations of carbon are as shown in Figure 2 [1]. Carbon forms a range of various organic compounds. It has the unique property of combining with various

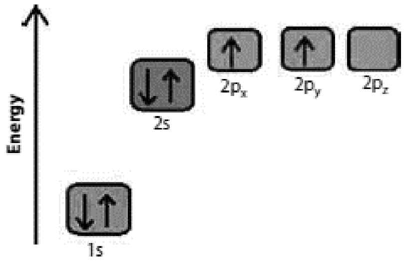

Figure 1: Energy levels with electrons in Carbon atoms *[1]*.

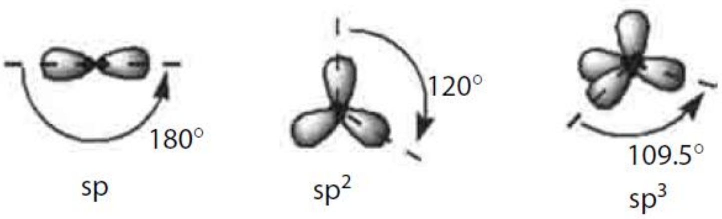

Figure 2: Hybridization types in carbon atoms *[1]*.

other elements in a range of different ways. That is one of the reasons why it is an essential part of living things.

Multiple layers of graphene stacked on each other form graphite [1] while graphene is a single layer of carbon atoms arranged in its honeycomb crystal lattice. Graphite have been in use for centuries before graphene was known since it was mined and found naturally in its ore form. The atomic structure of graphene and graphite is as shown in the Figure 3. The distance between adjacent carbon atom in graphene is 0.142 nm while the height of an individual graphene layer in graphite is 0.33 nm. There is a very deep relation between graphene and other forms of carbon forms. This correlation is as depicted in the Figure 4. Single sheet of carbon atoms in the honeycomb lattice is graphene, stacks of graphene on each other is what forms graphite, rolls of graphene are referred to as carbon nanotubes while spheres of graphene sheets are called fullerenes. Out of the different forms, fullerenes are supposed to have a zero-dimension, graphene is two dimensional while carbon nanotubes are one dimensional. It would not be wrong to say that these forms of carbon cover a wide range of different dimensions.

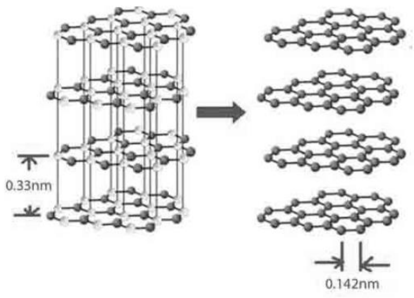

(a) *(b)*

Figure 3: Atomic structure: *(a)* Graphite *(b)* individual graphene layers *[1]*.

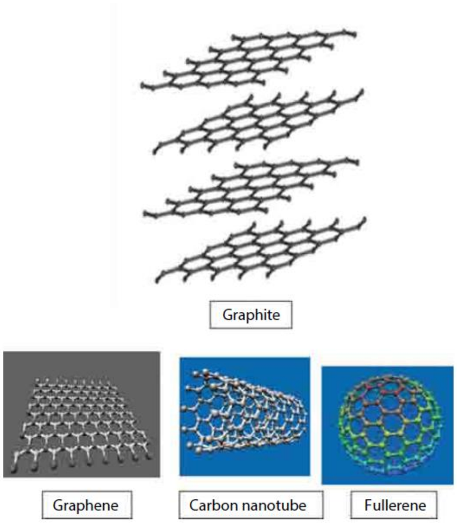

Figure 4: Different forms of carbon and their structural relationship *[1]*.

In graphene, the carbon atoms are *sp^2* hybridized and each is covalently bonded to three other carbon atoms, thus forming the honeycomb structure as shown in the Figure 5 *(a)* [17]. Each carbon atom in graphene is attached to another carbon atom with a different sublattice. The different sublattices are depicted as A and B. There are two different types of bonds that come into play in graphene, namely, the σ and π bonds. While the σ bonds are responsible for the overall strength of the material since they are the strongest, there is no contribution whatsoever due to this bond due to a lack of free electrons. The bond responsible for the electrical conduction are the π and π * bonds. This is as shown in the Figure 5 *(b)* [17].

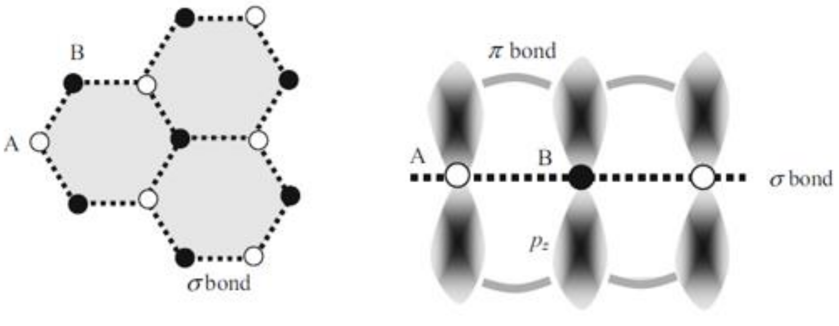

(a) *(b)*

Figure 5: Graphene atomic structure: *(a)* Honeycomb structure of graphene with different sublattices of carbon atoms; *(b)* orbitals depicting σ and π bonds [17]

The very unique molecular arrangement tends to give graphene its signature mechanical, thermal, optical and electrical properties. A combination of these properties gives graphene a wide range of different applications in a variety of fields which has deemed graphene to be one of the most studied material of the century. In the following the characteristic properties of graphene are briefly discussed.

Mechanically, graphene is one of the strongest materials with very high elasticity. It can be stretched extensively and yet withstand pressures of the order of multiple atmosphere. It doesn't allow even the smallest of atoms like helium which deems it impermeable. It has a very fracturing strength of 130 GPa which makes it 200 times stronger than steel yet is very light with density equating 0.77mg/m^2. It has a tensile high young modulus of 1.0 TPa [18].

The thermal properties are also not modest. Graphene is very highly thermally conductive with conductivity values reaching 5000 W/mK^{-1} at 27 °C [19]. These high thermal conductivity values are as a result of very strong carbon bonds due to which there is negligible phonon scattering. The thermal conduction in graphene hence is due to low energy phonons which are responsible for such high values of conductivity. In modern day electronics there is a large amount of heat produced by electronic devices due to a continuous demand of increase in the operating frequency. It is because of these high thermal conductivity values that graphene has found various applications in electronics for heat dissipation.

Graphene also posses' magnificent optical properties which is why it has found a range of different applications in photonics. Graphene is optically transparent and transmits 97.7% of light impinging on its surface. The optical properties changes with the increase in the number of graphene layers. A measure of graphene transmittance at different wavelengths for different number of layers is as shown in Figure 6, which is reported according to [20]. The transmittance of graphene is sufficiently flat for wavelengths ranging from 500 nm to 1000 nm and there is a reduction in the transmittance with increase in the number of layers. Graphene also possess very low value of optical resistivity of the order of 10^{-6}Ωcm along with mechanical flexibility as formerly reported making it viable for use in displays as compared to more expensive conventional devices.

The triangular sublattices of the honeycomb structure in graphene penetrate each other, thus forming a spinor wave function of the charge carriers. This is similar as other semiconductors, which also have a spinor wave function and not a scalar one. The energy dispersion relation based on a tight binding approximation in which only the nearest charge carriers' interaction is considered is as follows [21]

$$E(k) = \pm\sqrt{3 + 2\,cos(\sqrt{3}k_y a) + 4\,cos(\frac{\sqrt{3}k_y a}{2})\,cos(3k_x a/2)} \qquad (1)$$

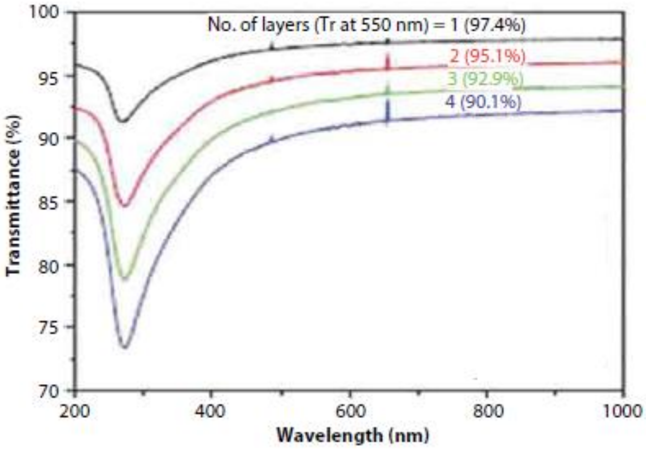

Figure 6: Transmittance of graphene versus wavelength for multiple layers *[20]*.

In the equation, *t=2.75 eV* is the energy required charge carrier to change sublattice to the nearest location, referred to as nearest neighbor hopping energy and *a=0.142 nm*, is the distance between adjacent carbon atoms. The two energy bands, π and π* are represented by the positive and negative sign. This dispersion relation is as depicted in the Figure 7.

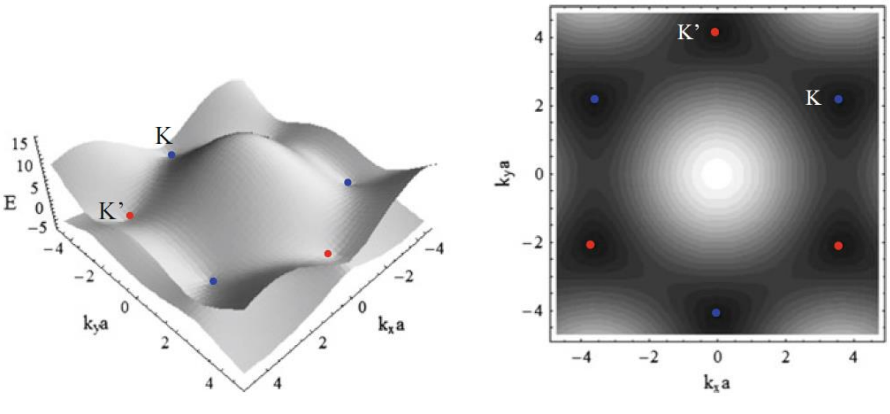

Figure 7: Plot of the dispersion relation of graphene (left), top view (right) *[17]*.

The dispersion relation for the low energy values around the dirac points can be simplified as:

$$E = \pm \hbar |k| v_f \qquad (2)$$

Here, the fermi velocity, $v_F = 3ta/2\hbar \approx c/300$ and k is the wave vector with, $|k| = \sqrt{k_x^2 + k_y^2}$. It can be seen from the plot of the dispersion relation of graphene that the energy bandgap is zero at the dirac points as represented by K and K' in the Figure 4. The dispersion relation also shows that the effective mass of charge carriers around the dirac point is negligible, which is in contrast to other semiconductors. It is also pertinent to note here that the transport properties for each of the charge carriers i.e., the electrons and the holes are identical, which is due to the symmetry of the dispersion relation around this dirac point. This is why graphene is referred to as ambipolar.

The linear dispersion relation for monolayer graphene means that the charge carrier in graphene bears zero effective mass and thus propagate without any collisions. This is also referred to as ballistic propagation. The charge carrier in graphene in case are called fermions. A similar phenomenon exists in the case of photons propagating in vacuum. The speed of fermions, however, in the case of graphene is $v_F=3ta/2=10^6 m/s=c/300$. The propagation of fermions in graphene is different than the propagation of photons in vacuum in that the photons propagate in vacuum by the speed of light whereas the fermions in graphene propagate with a velocity several orders of magnitude lower than the speed of light therefore the propagation in graphene can be referred to as a slow wave.

For tuning purposes, it is important to study the graphene FET configuration as shown in the Figure 8. Electrical doping is a characteristic property of graphene. Graphene is deposited on SiO_2 which is placed on top of doped silicon. The doped silicon has metal-like properties and acts as a back-gate. The carrier density of the graphene layer can be modulated by the help of the applied gate voltage. The relation of the carrier charge density is as follows according to [2].

$$n = \in_0 \in_d {}^{V_G}/_{t_e} \qquad (3)$$

Here, V_G is the gate voltage, $\in_0$ is the permittivity of air and $\in_d$ is the permittivity of SiO_2. The applied voltage at the gate is what drives the fermi energy level of the graphene layer. The electrical doping for the two types of carriers is depicted in the Figure 9. It is evident that the fermi energy level, that is at the dirac point is zero. Depending upon the applied gate voltage the fermi energy level can be taken to either the upper part (governed by the electrons) or the lower part (driven by holes). It is also evident from the Figure 9 that the electrical doping for both the carrier types is identical, a phenomenon referred to as ambipolarity. The shift in fermi energy levels and the electrical doping behavior is what shapes the conductivity of graphene. This phenomenon in graphene monolayer is as follows.

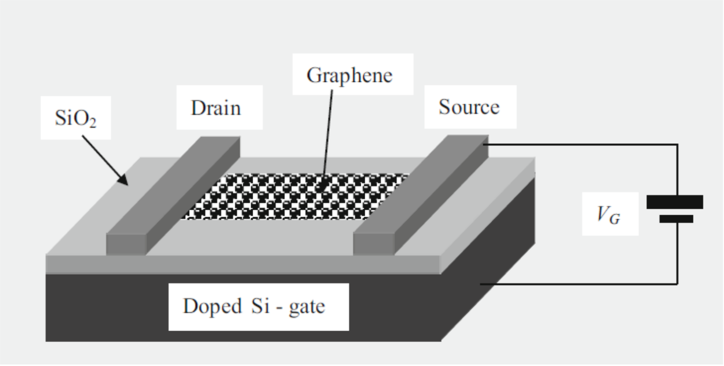

Figure 8: Graphene FET configuration for studying tunable conductivity of graphene *[17]*.

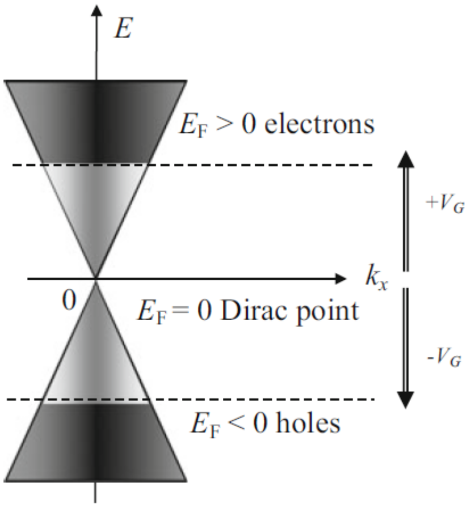

Figure 9: Ambipolar transport in graphene *[17]*..

The conductivity of graphene is dependent on the gate voltage applied to the configuration shown in the Figure 8. For positive applied gate voltage, the conductivity increases in the positive side while for the negative applied gate voltage it drastically reduces. The conductivity relation to the applied gate voltage is also ambipolar as is evident from the Figure 10. The conductivity in graphene is not strictly related to temperature and there is a very slight change with respect to a change in temperature. Hence the relation of gate voltage versus the conductivity holds true for a range of different temperatures. The conductivity of graphene is also important since it can help in calculating several other parameters, for instance mobility of charge carriers, the scattering rate and mean free path among several others.

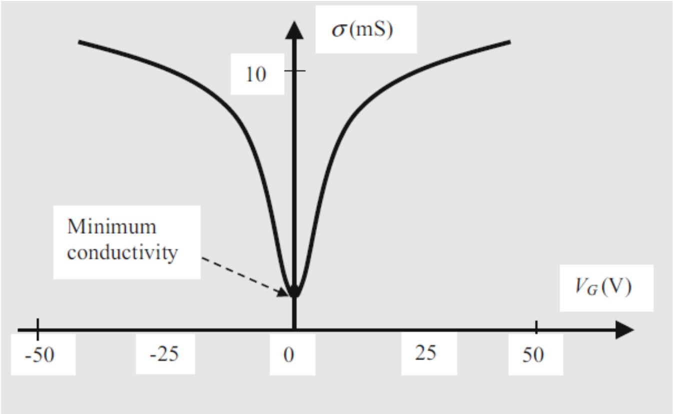

Figure 10: Applied gate voltage versus conductivity of graphene *[17]*.

2.2 Application at Terahertz Frequencies

Graphene possesses unique quantum electromagnetic properties as experimentally shown in 2005 in [22], [23]. The dispersion relation of energy and momentum in graphene is linear, which is an added advantage over most conventional semiconductors [24]. The electron-hole generation in graphene is gate controllable at all frequencies which makes graphene tempting for use at all such frequencies. Interest in graphene in the optoelectronic area is vastly due to its optical absorption characteristics in a wide band of frequencies going down to as low as the THz [7]. Among its other optical properties is the light excitation of collective oscillation of carriers [25] and the inversion of its conical electronic band by optical excitation [26]. A combination of these intriguing properties enables graphene to obtain application in various terahertz communication systems. The optical conductivity of graphene comprises of two different transitions: the interband and intraband transition. These act as two individual components as depicted in the equation below according to [27]:

$$\sigma(\omega) = \sigma_{intra}(\omega) + \sigma_{inter}(\omega) \qquad (4)$$

For High frequency values, both the interband and intraband conductivities have significant contributions towards the total conductivity since short wavelength photons posses enough energy to trigger band to band transitions. However, at lower frequencies or frequencies of interest to THz, the long wavelength photons lack the energy to excite band to band transitions and hence the only significant contribution comes from the intraband transition. The negligible contribution of interband conductivity due to photon excitation can be ignored and hence the total optical conductivity is:

$$\sigma(\omega) = \frac{\sigma_{DC}}{1+j\omega\tau} \qquad (5)$$

In the above equation, σ_{DC} is the electrical conductivity of graphene at DC, τ is the electron momentum relaxation time and ω is the angular frequency. As formerly described, the conductivity of graphene is gate tunable and can be tuned by changing its carrier density. A wide range of tunable terahertz devices and structures can be designed on the said phenomenon. These devices can have novel applications in a wide range of future communication systems. In the following some of the applications are briefly discussed.

Based on the its properties at terahertz described above, graphene is a strong contender for terahertz modulators. Conventionally, metal gates are used in terahertz modulators. These metal gates have the disadvantage of not only limiting the modulation depth but also greatly attenuating the terahertz signal. These problems can be countered by incorporating graphene in place of metal gates [28]. Graphene has been used in combination with a number of metamaterials for designing novel modulators with improved functionality in terms of higher modulation depth, less attenuation and broader bandwidth by exploiting its variable carrier density [29-35]..

2.2.1 Graphene Terahertz Modulator

The first electro-optical absorption-based terahertz modulator was reported in [8] but the modulation depth achieved was 15%. With system requirements much higher, such a low modulation depth was seemingly useless. A novel technique in order to increase the modulation depth is to use reflection mode structures as in [8]. The distance between graphene and reflector is fixed at an odd multiple of quarter wavelength in such structure and electric field is enhanced [8]. The device as depicted in Figure 11 *(a)*, is comprised of silicon substrate with top layer of SiO_2. Graphene monolayer is deposited on top of the SiO_2 substrate. Terahertz are impinged through the graphene monolayer and reflected back by the metal layer underneath, distances between graphene and reflector with even multiples of the quarter wavelength result in zero absorption while odd multiples result in maximum absorption. The electric field variation is also depicted in the top right of Figure 11, where the variation in the fermi energy level is what shows the maxima and minima of the reflectance in the modulator. The maximum in the case of [8] is attained at 0.62 THz with 64% of modulation depth and 2dB insertion loss. The frequency band is low because of its dependence on the physical dimensions of the structure.

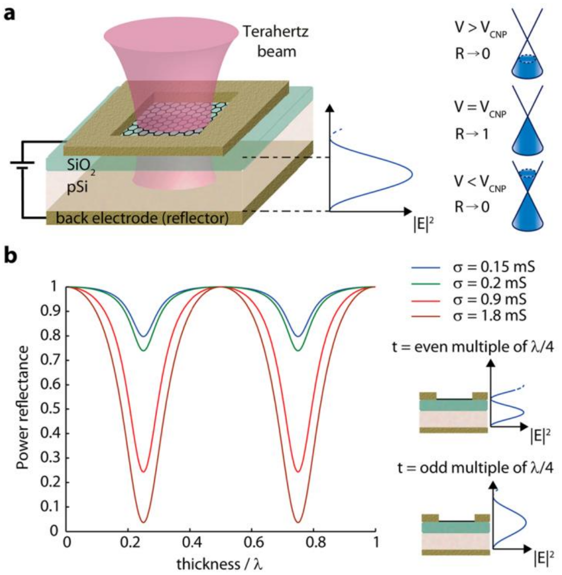

Figure 11: Electro optical absorption-based terahertz modulator; *(a)* schematics of the modulator; *(b)* Power reflectance. Figure taken from *[8]*.

Another technique by which terahertz modulation can be performed is by the help of graphene plasmonic structures [36]. Amplitude modulation is achieved by changing carrier density by shifting geometric plasmonic resonance in graphene stripes. Since CVD grown graphene has high resistance value and thus lower conductivity therefore the extinction levels attained are about 14%. In order to counter this problem, graphene periodic structures can be combined with reflection mode configurations as in [37].

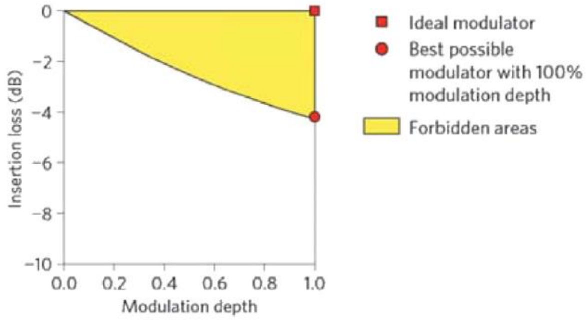

Figure 12: Functionality limits of Graphene modulators *[31]*.

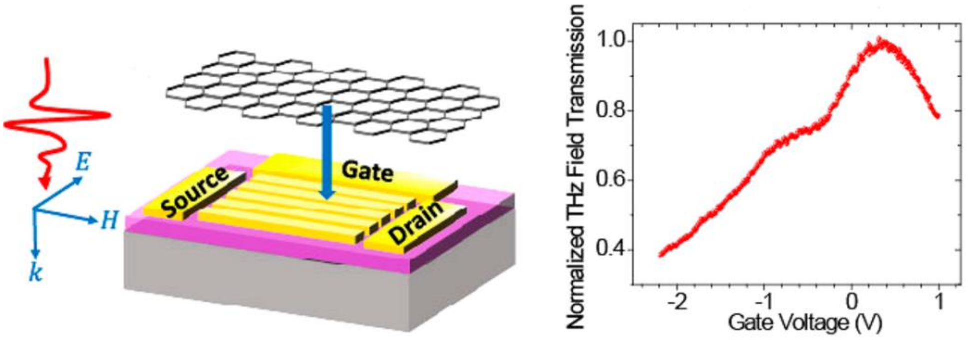

(a) (b)

Figure 13: Hybrid graphene-metamaterial terahertz modulator: (a) design of the modulator; (b) Gate voltage versus Normalized THz transmission *[38]*.

In order to further improve the functionality of terahertz modulator and thus increase light-matter interaction in graphene, metamaterials can be used. The use of metamaterials is particularly beneficial in supplementing the electric field. However, there is always a tradeoff between the modulation depth, insertion loss and bandwidth. A theoretical study performed in [31] demonstrates all the three possibilities. The real modulators lie outside the area of the best possible modulator while going beyond best possible is practically impossible to attain. The ideal modulator is when the insertion loss is zero and there is a 100% modulation depth. *Figure 12* shows a representation of this phenomenon. The limits of modulation thus specified are a 100% modulation depth with less than 4dB insertion loss which cannot be attained. In the following an example of a terahertz modulator based on metamaterials is briefly discussed.

A proposed design of metamaterial-based graphene terahertz modulator was shown in [39]. It was subsequently experimentally demonstrated in [38]. The modulator is based on arrays of periodic gold slits and graphene is used in the design as a tunable conductive load as shown in *Figure 13(a)*. In the gold slits, the localized in-plane field is enhanced, which is coherently radiated towards the graphene layer. This radiation in turn results in the field enhancement in the graphene layer. The field transmission vs gate voltage is as shown in the *Figure 13(b)*. A decoupling of the field enhancement in graphene layer results in preserving broadband terahertz modulation unlike the previously discussed design. In this design, the terahertz absorption is very strong and so is the local field enhancement, a combination of which result in a modulation depth as high as 90%. Another technique that can be used to further increase the modulation depth is to increase the number of graphene layer but as discussed in the tradeoff of the functionality limits, it will increase the insertion loss further.

Another innovative technique in graphene terahertz modulators is the use of optical pumping of graphene along with incident terahertz in a hybrid structure. The properties of graphene are engineered to acquire higher modulation depth. In [40], single layer graphene is deployed on top of germanium, which is driven optically by a 1550 nm laser as shown in the *Figure 14*. As a result, a modulation depth of 94% is attained in the frequency band of 0.25-1 THz. It is also claimed that the terahertz modulation in the proposed structure is due to the third order nonlinearity of the graphene monolayer conductivity. Based on a similar principle, a quantum cascade laser integrated graphene modulator was produced in [41]. A monolithically integrated graphene modulator modulates light intensity of the terahertz radiation from the terahertz quantum cascade laser. This design as shown in *Figure 15*, although complicated shows improved modulation depth along with an increased modulation speed greater than 100 MHz, which is almost three orders of magnitude higher than other graphene terahertz modulators. It even claims 100% of modulation depths at specified regions of pumping currents. All these added advantages are due to the very strong and close interaction between laser field and graphene layer due to its proximity in the cascade.

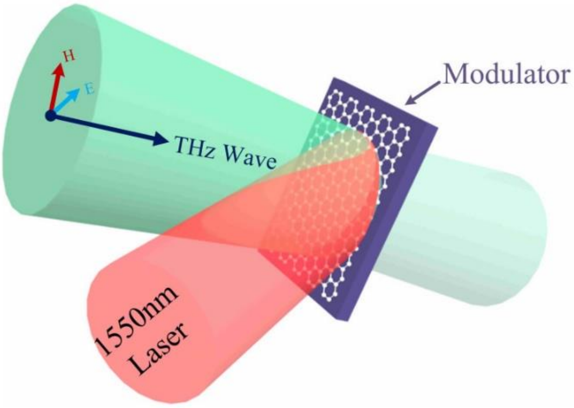

Figure 14: Graphene terahertz modulator based on optical pumping *[40]*.

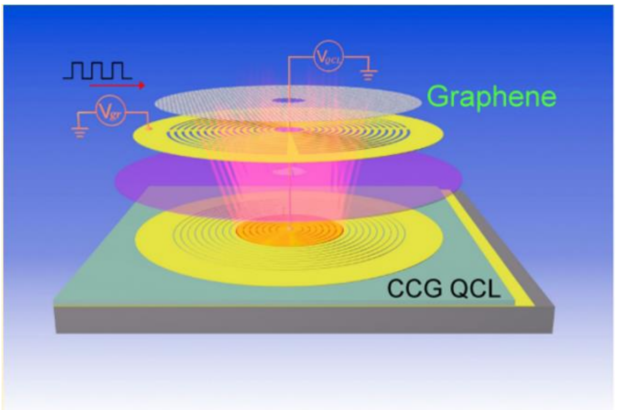

Figure 15: Integrated Terahertz Graphene Modulator *[41]*.

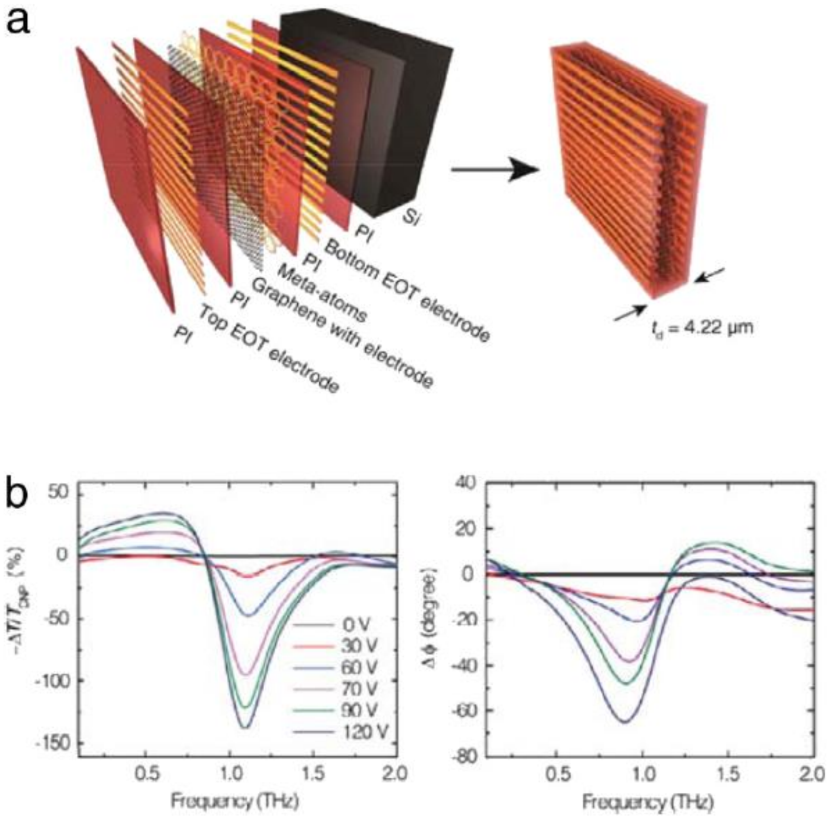

Figure 16: Terahertz graphene Phase modulator: *(a)* design; *(b)* Amplitude and phase change respectively *[42]*.

It is also pertinent to mention here that the optical excitation methodologies as previously discussed can be combined with dc excitation for actuation purposes. In [43] a graphene-silicon hybrid device has been proposed. The device is simultaneously excited by DC and photo-excitation. The device has been termed as an active diode and transmits terahertz wave with a positive applied bias while attenuates terahertz signal at a negative applied bias. It has a fairly good modulation depth of 83% at an applied bias voltage of 4V.

Phase modulation is of equal importance to amplitude modulation for a wide range of terahertz applications. The proposed devices for terahertz phase modulation typically comprised of a hybrid graphene-metal structure [44]. The metallic meta surface would provide peaks of resonances while the graphene layer would provide the tunable characteristics. The problem with phase modulation usually is its dependence on the amplitude. The minimum the change in amplitude when there is a phase change, the better. The advantage at terahertz is that the amplitude and phase change can be related to each other by the KK (kramers-kronig) relation as demonstrated by [45]. According to the relation, at frequencies which provides high amplitude change there is a very limited phase change and at frequencies where there is a high phase change the amplitude change is negligible. Therefore, the later frequencies, at which there is a minimum amplitude change and a maximum phase change, can be exploited for phase modulation purposes. According to [46], in order to achieve phase change at desired frequencies, the phase change can also be shifted to those frequencies by planar graphene plasmonic waveguide. In [42], phase modulation was achieved by a multilayer structure comprising of graphene attached to metallic meta surface with two electrodes on each side for gating purposes as shown in *Figure 16(a)*. A phase shift of 65° was achieved at a frequency of 0.9THz. The resulting amplitude shift is as shown on the left in *Figure 16(b)* while the phase shift is as shown on the right in *Figure 16(b)*.

2.2.2 Graphene Terahertz Sources and Emitters

Sources and emitters are another very important part of communication systems and terahertz is no exception. Terahertz emitters can be broadly classified into three kinds: Diode based sources also called electronic sources, microtube sources and quantum lasers. All these emitters have certain drawbacks. Diode based electronic sources are limited by their maximum frequency of operation since at higher frequencies output power reduces due to transient electron time. Microtube sources are based on proximity principle and hence require significantly large fields. Quantum lasers need to be cooled down and are limited by their efficiency at room temperature. Alternative to generating sources at their intrinsic frequency is to convert the frequency of a source either by down conversion from a higher frequency source or by frequency multiplication from a low frequency source to a high frequency source. The use of novel materials for such applications is inevitable in order to overcome all the disadvantages of conventional terahertz sources. Graphene therefore is a good contender for such applications.

The basic principle is to either optically pump graphene monolayer or inject carriers. The main hurdle in both optical pumping and carrier injection is the limited quantum conduction in graphene. A single graphene layer absorption is limited by $e^2/4\hbar=2.3\%$ [47]. Increase in the number of layers of graphene is one way to counter this problem, which is not so effective since with number of graphene layers as high as 20 yet the absorption coefficient is 1 cm^{-1} as demonstrated in [48]. Another approach is to avoid normal incidence directly on graphene and use waveguide structures so as to increase gain. A much innovative method, however is to use surface plasmon polaritons [49]. When a plasmonic wave is excited in graphene as shown in *Figure 17(top)*, the resultant group velocity is smaller than the group velocity in free space. This drastically increases the light-matter interaction at excitation of a plasmonic wave in graphene. Thus, the resultant gain is very high as compared to photonic devices. The absorption and gain values versus frequency is as shown in the *Figure 17(bottom)* for the different values of quasi fermi energy values.

Another technique is to use P-I-N junctions with multiple graphene layers incorporated in the intrinsic layer as shown in *Figure 18* [50]. Carrier population is inverted by the application of a voltage between drain and source. This result in a recombination of electrons and holes by the help of optically assisted interband transition. When the voltage is increased by some mV, there is a spontaneous scattering of terahertz photons. The same principle can also be applied to suspended graphene as in [51] with limits of electromagnetic radiations as high as 1THz.

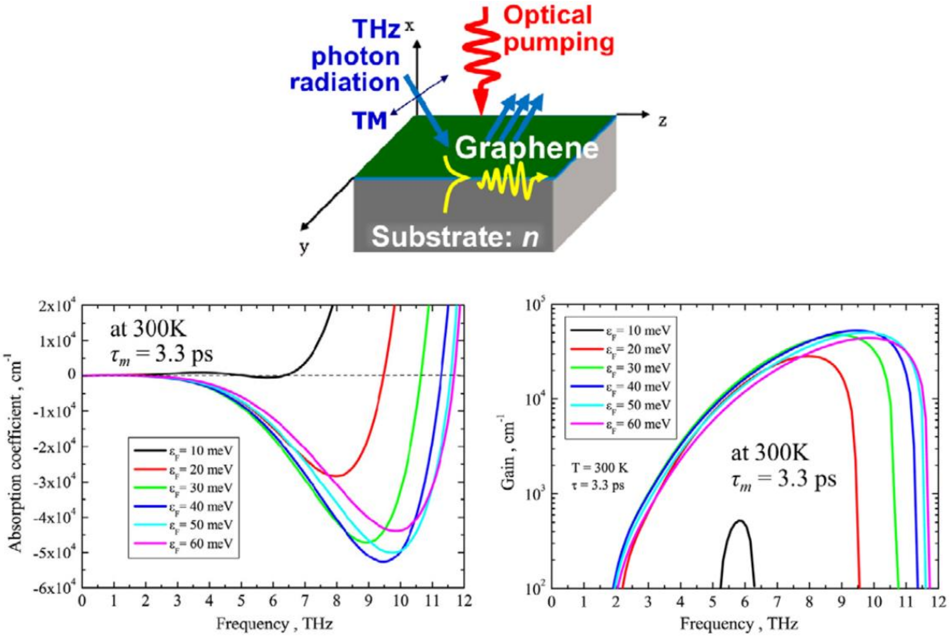

Figure 17: Surface Plasmonic Polaritons for terahertz sources*: (Top);* topology of the emitter; *(bottom):* absorption coefficient and gain versus frequency. *[49]*

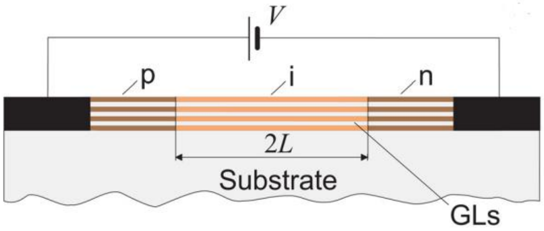

Figure 18: Cross-sectional view of multi-layer graphene-based PIN terahertz laser *[50]*.

2.2.3 Graphene Terahertz Detector

Detection at terahertz is very critical for a wide range of applications ranging from defense and military to biomedical and pharmaceuticals. Conventional terahertz detection systems are based on a variety of principles ranging from bolometers to heterodyne mixers and schottky diodes. All these have drawbacks like very high sensitivity to interference or temperature, loss of functionality at higher frequencies and poor mechanical stability. In general, the two parameters used to characterize the functionality of detectors are: Noise equivalent power (NEP) and detectivity. NEP shows the sensitivity of the detector and is the power of the detected signal with the value of the signal to noise ratio (SNR) of one at one hertz output bandwidth. Detectivity is also related to the NEP but also incorporates the area of the detector. Graphene based detectors can broadly be classified into three types: i.) detectors based on Tunnel FET with single layer graphene, bilayer graphene and GIG (graphene insulator graphene), ii.) top gate antenna coupled GFET and iii.) detectors exploiting thermal and photo thermal (PTE) effects of graphene [6].

It was first demonstrated in [52] that DC voltage is induced from source to drain by rectification of plasma wave generated by modulation of carrier density and velocity of an incident terahertz wave on an antenna. Furthermore, the time it takes plasma wave to travel from the source terminal to the drain terminal is usually less than the electron momentum relaxation time. This would induce a resonant condition in the FET. In order to cause overdamping of the plasma wave in the FET either very high values of electron mobility or very long channels are required. The NEP of this setup can be increased by biasing the gate terminal and applying zero voltage from source to drain when detecting at the drain. In short, very high mobility values are critical for the functionality of this setup. Graphene bears very high electron mobility is thus a very good contender for such applications. Another discriminating factor for graphene in these applications is it supports weakly damped plasma waves [53]. Based on these principles several detectors have been produced comprising of single layer graphene, bilayer graphene and graphene insulator graphene FETs. Among these, the GIG TFET based detector is very promising as reported in [54]. A schematic of the design is as shown in the *Figure 19 (a)*. The graphene layer used in such detector can either be monolayer or bilayer, both demonstrating negative differential conductance as shown in *Figure 19 (b)*. The grating gate as shown in *Figure 20* can be used to efficiently couple the terahertz radiation with plasmons [55].

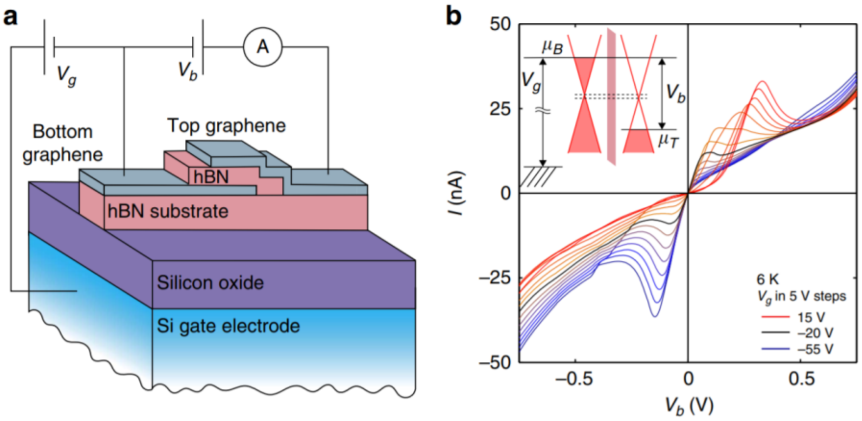

Figure 19: Graphene-insulating-graphene tunnel FET: (a) schematic design; (b) current voltage relation showing negative differential conductivity, inset showing positions of the Fermi energies of the doped Si substrate gate *[54]*.

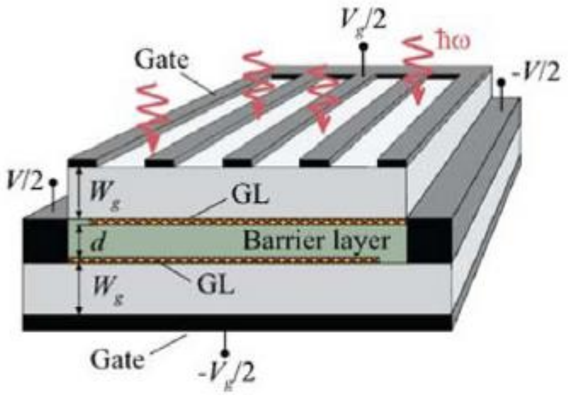

Figure 20:Grated gate terahertz GIG TFET detectors *[55]*

The second type of terahertz detectors are the antenna coupled GFET detectors. An example of which is the periodic circular-toothed antenna in which the arms of a low shunt capacitive antenna are connected to the gate and source of a GFET [56]. The application of a terahertz signal on the antenna directs the signal towards the channel. The nonlinearity of the transfer characteristic rectifies the signal inducing a DC signal between the source and the drain. The topology is as shown in *Figure 21*. The angle between the beam polarization axis of the impinging terahertz signal and the antenna axis is critical to the responsivity values as shown in the *Figure 22* (only single layer case shown for example.)

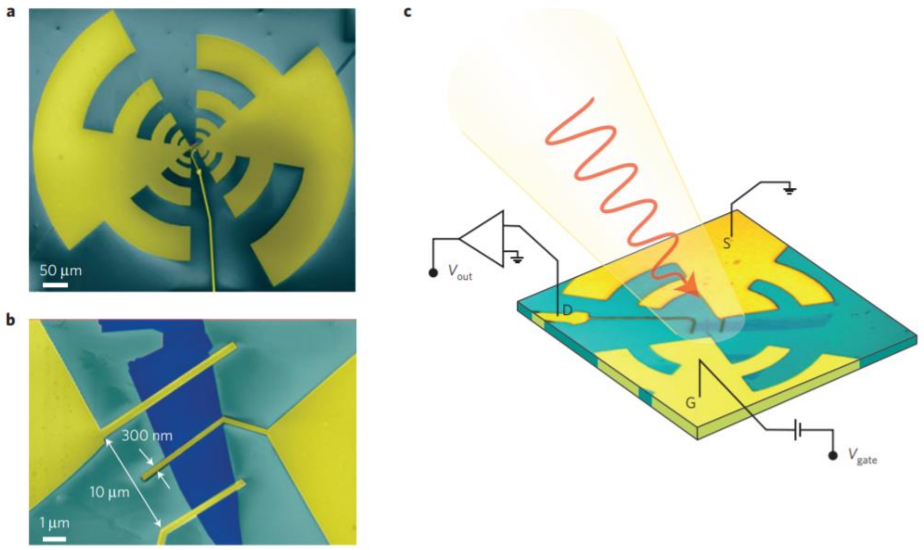

Figure 21: Antenna coupled GFET-THz detector: (a) top view; (b) source and gate attachments to the antenna; (c) source, drain and gate with connections *[56]*.

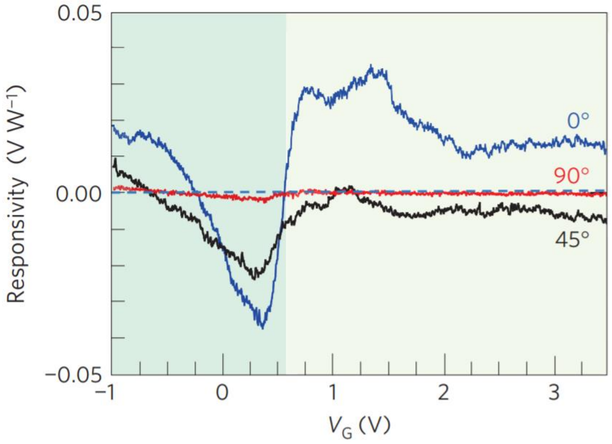

Figure 22: SL GFET THz Detector responsivity for different beam polarization axis and antenna axis *[56]*.

The third kind of terahertz graphene detectors exploiting the thermal or photothermal properties of graphene are based on either the photo induced bolometric effect or the photo thermoelectric seebeck effect.

As the name suggests, the bolometric graphene terahertz detector works on the principle of thermally induced change in resistance of the device when excited by terahertz waves in the mid infrared range. In graphene based bolometric detectors, incident terahertz radiation augments the temperature of graphene. As a result, the resistance of the graphene layer is changed varying the current at a given applied bias voltage. In [57] dual gated bilayer graphene is deployed in hot-electron bolometer. In Figure 23, the topology of the device is shown along with the photo response and the resistance dependence on the temperature. In detail, the bilayer graphene causes the absorption of light inducing a temperature change due to a varying electron temperature by two factors: small electron heat capacity and weak electron-phonon coupling. The dual gate in the device helps in creating tunable bandgap resulting in graphene conductivity that is dependent upon electron temperature. The detector has a voltage responsivity of $2x10^{5}VW^{-1}$ and NEP of $33fWHz^{-1/2}$ at 5K. Regarding the thermoelectric effect, the principle of operation of the device is the generation of a thermoelectric current by a combination of laser spot creating a temperature gradient augmented by a doping asymmetry. In graphene, photoexcited electrons lose energy slowly into the lattice causing temperature gradient. A net current is then generated by asymmetric metal contacts from the temperature gradient (temperature change caused by the laser). This phenomenon is commonly used in detectors and is termed as the seebeck effect therefore these detectors can also be termed as graphene-based photo-thermoelectric seebeck detectors. In [58] the graphene photo-thermoelectric detector proposed is based on single layer exfoliated graphene. The voltage responsivity of the device is 700 VW with NEP of 20pWHz-1/2.

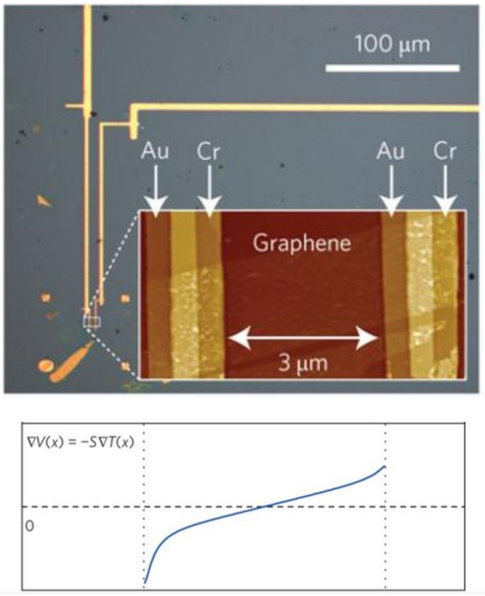

Figure 23: Graphene photothermoelectric detector: (top) micrograph; (bottom) voltage responsivity *[57]*.

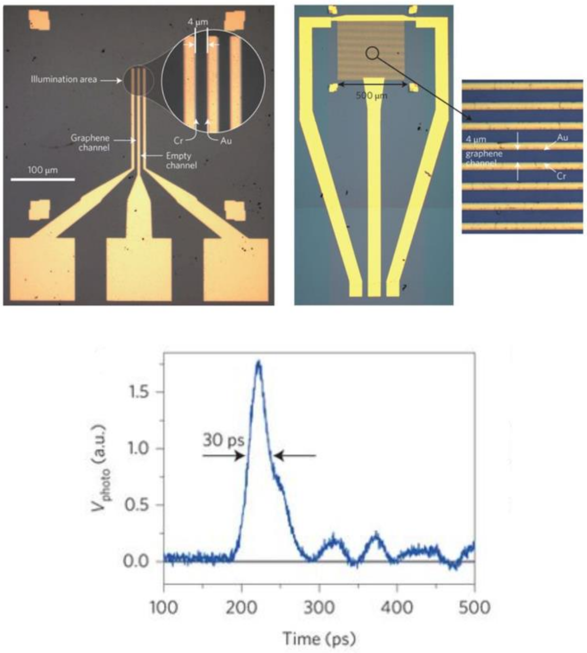

Figure 24:Graphene photothermoelectric detector with multiple graphene channels: (top) micrograph; (bottom) photoresponse showing device speed *[58]*.

The schematic of the proposed device along with the voltage responsivity is as shown in the *Figure 23*. In order to increase the speed of the device, multiple graphene channels are deployed as shown in the*Figure 24*. The resultant electrical excitation from terahertz after a pulsed excitation occurs is as shown in the *Figure 24*. [58].

2.3 Applications at Microwaves/mm-waves.

A combination of mechanical, thermal and electronic properties makes graphene suitable for use in the microwaves/RF frequency applications. As formerly discussed graphene exhibits extraordinary electronic properties like very high carrier mobility coupled to tunable conductivity and ambipolarity. Graphene is a single atom thick sheet of carbon atoms attached to each other in a honeycomb lattice. Out of the four valence electrons of graphene, three are bonded to theirs neighbors via the σ bond while the fourth one is bonded with the π bond. The parallel along the crystal lattice are the σ bonds in graphene which give it a very high mechanical stability. The π bond in graphene is perpendicular to the graphene sheet and hence delocalized giving it its unique electronic properties. The charge carriers in graphene can therefore be described by the dirac equation unlike in usual solids in which they are described by the Schrodinger equations. The linear dispersion relation means that graphene’s carriers behave as massless fermions. Thus, they propagate without any collisions with the lattice and the propagation is ballistic. The propagation velocity of carriers in graphene is $v_F=c/300$. The two energy bands in graphene touch each other at zero energy and does not possess any bandgap making graphene unsuitable for switching applications. A graphical representation of the dispersion relation of graphene is depicted in *Figure 25*.

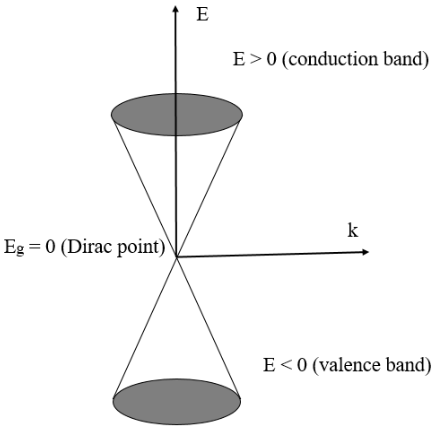

Figure 25: E-k band structure of graphene.

The size of graphene samples drastically increases as we move in the microwave/mm-wave range of frequencies and as a consequence reduction in the electron mobility occurs due to non-ballistic conduction. More important at such frequencies thus is the tunable conductivity and the ambipolar behavior of graphene. The tunable conductivity of graphene occurs due to the shift in the fermi energy level. When a voltage bias is applied there is an increase in the surface charge density which shifts the fermi energy level into the conduction or valence band resulting in an electron/hole dominated conduction increasing conductivity (or reducing resistivity). This is as depicted in the *Figure 26*, where charge density versus surface resistivity is shown [10].

Unlike usual metallic materials which are represented by classical Maxwell's equations, Graphene monolayer is represented by a conductivity surface arising from a semiclassical intraband mode and quantum dynamical interband mode. As discussed in the section 2.2, in the lower THz frequencies, the intraband conduction in graphene is what dominates its conductivity. The same is true for micro/mm-wave frequencies. The surface conductivity of a mono-graphene layer as a function of frequency is thus given by the kubo's formula. Applying the drude model, which simplifies the kubo's

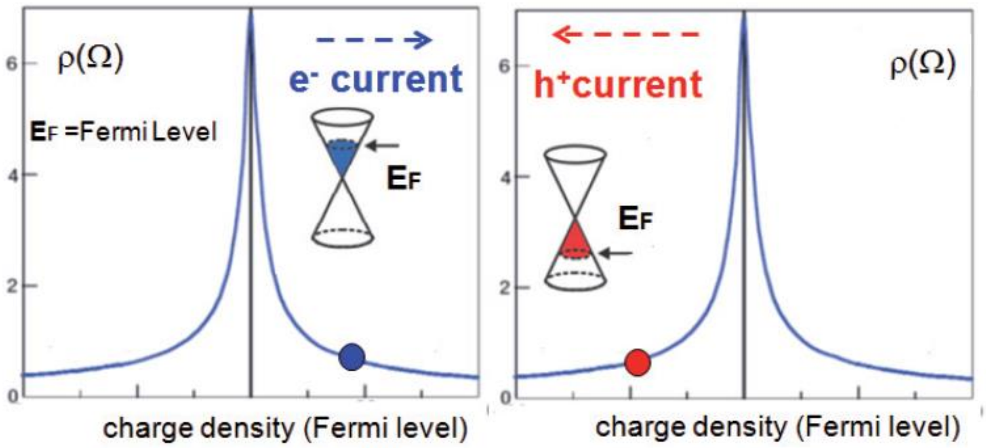

Figure 26: Graphene's shift in fermi level/changing charge density causing change in its resistivity; (left) electron contribution; (right) hole contribution. *[10]*

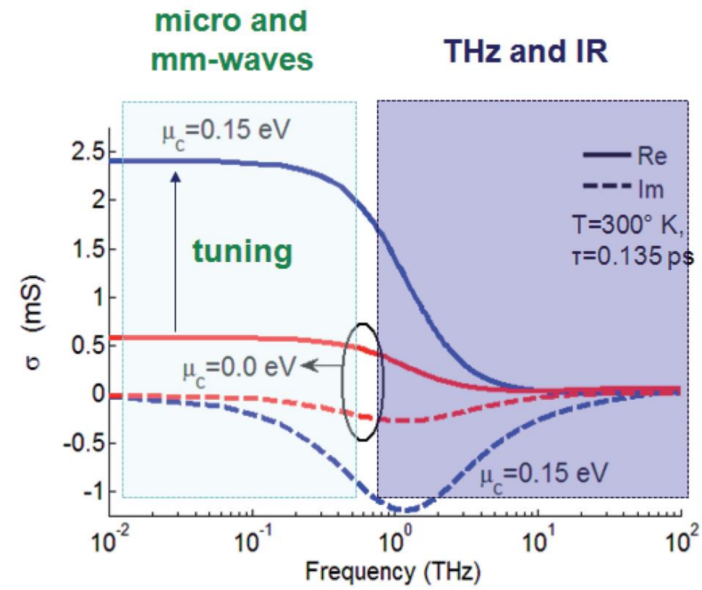

Figure 27: Graphene's surface conductivity for different frequencies. *[10]*

formula for the condition, $\mu_c >> \hbar\omega$, where $\mu_c > 0.05\ eV$, is the fermi level of graphene, $\hbar$ is the reduced planck constant and ω is the angular frequency, the surface conductivity, σ is given by below [59].

$$\sigma = \frac{2e^2\tau}{\pi\hbar^2} k_B T \, log\left(cosh\frac{\mu_c}{2k_BT}\right)\frac{1}{1+j\omega\tau} \tag{6}$$

With τ as the scattering time, k_B as the Boltzmann constant, T as the temperature, with μ_c for graphene satisfying the relation $\mu_c >> \hbar\omega$ for microwave frequencies and beyond. The relation thus yields the curves of *Figure 27*. It can be notices that the behavior of surface conductivity of graphene changes with frequency. At the micro/mm-wave frequencies graphene's the real part of surface conductivity is high as compared to terahertz frequencies when it reduces drastically. It is also noteworthy that the real part of the surface conductivity changes with the fermi level, μ_c. This change can not be seen for frequencies exceeding 1 THz. The imaginary part of the conductivity behaves differently, in that it shows very slight variation with changing fermi levels at micro/mm-wave frequencies [10]. These intriguing properties of graphene makes it suitable for use in a variety of microwave applications. One of the first attempts in the RF and microwave frequency was an FET with microwave cutoff frequency. A range of applications followed afterwards with antennas, attenuators and various other shielding applications.

2.3.1 Graphene RF FET

The first attempt of the graphene FET was done as early as 2004 [2] but the RF performance of epitaxially grown graphene FET has been only demonstrated in 2009 [60] and mechanically exfoliated graphene in the same year [61]. The research on FET in the microwave regime exploded afterwards with several different works. The goal is to achieve higher and higher value of the cutoff frequency. The cutoff frequency of an FET is dependent on the gate length. It is important to consider the relation between the gate length and the respective cutoff frequency that it provides in order to check the functionality of a particular technology and the material that it adopts. A comparison of the different types of FETs and their gate length/cutoff frequency as depicted in [62] is as shown in *Figure 28*. In the *Figure 28*, the type A is the InP HEMT, B is the Si MOSFET, C is the GaAs pHEMT, the rest are as indicated. It is clear from the figure that the graphene FET shows significantly good values of cutoff frequency as compared to silicon MOSFET. The graphene MOSFET as reported in [63] provides 100 GHz cutoff for gate length of 240 nm while the silicon MOSFET [63] provides cutoff of 53GHz for gate length of 550 nm. The details of the GFET are described in the following.

Graphene is epitaxially grown on SiC by thermal annealing. A polymer layer based on a derivative of Poly-hydroxystyrene is spin coated on graphene with an atomic layer of HfO_2 on top, cumulatively forming the top gate. A schematic representation of the FET is as shown in the *Figure 29*. The graphene layer deposited bears an electron carrier density of about $3x10^{12}$ cm^{-2} with mobilities ranging from 1000 to 1500 $cm^2V^{-1}s^{-1}$. The gate dielectric deposition however reduces the mobility values with new values ranging from 900 to 1520 $cm^2V^{-1}s^{-1}$. The device figures of merit include the drain current for various gate voltages, the transconductance g_m which is dI_D/dV_G, and the current gain defined by the ratio of small signal drain and the gate currents (I_D/I_G).

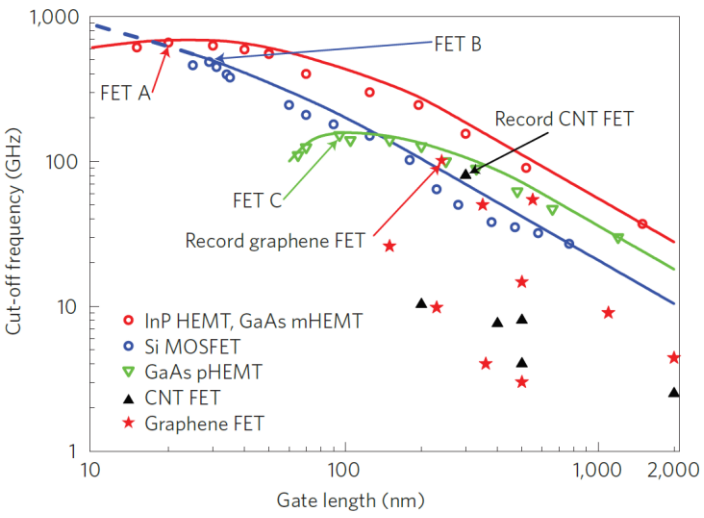

Figure 28: Gate Length versus cut-off frequency for various FETs *[62]*

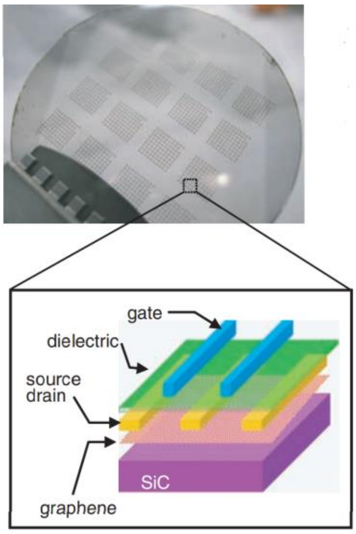

Figure 29: Schematic representation of GFET with topgate, dielectric and graphene layer in the inset, wafer on top [63].

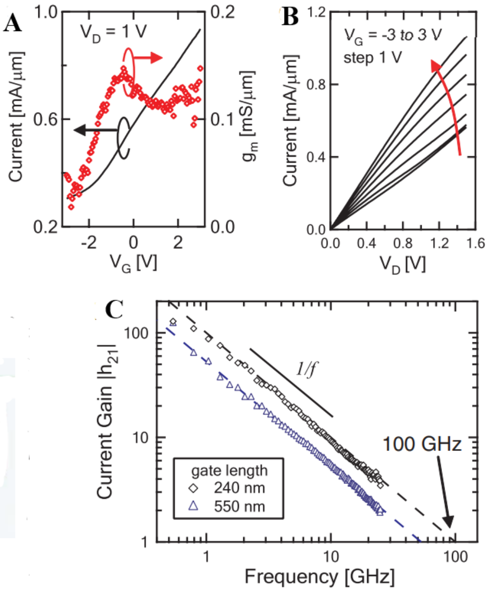

Figure 30: Graphene FET; (A) current gain and transconductance versus gate voltage; (B) Drain current versus Drain voltage at different gate voltage; (C) current gain versus frequency for two gate lengths [63].

These parameters for the GFET are as shown in the *Figure 30*. The drain current shows an n-type behavior when plotted versus the gate voltage as shown in *Figure 30(A)*. This is also plotted against the transconductance on the right which shows flat response for varying V_G. The drain current continuously increases with increasing drain voltage and does not show any saturation as in conventional FETs due to a non-existent bandgap. The behavior is shown with varying gate voltage in the *Figure 30(B)*. Finally, the most important is the cutoff frequencies for a wide range of different gate lengths and its relation to the current gain. As shown in the *Figure 30(C)*, the cutoff frequency is inversely related to the gate length with values of 53 GHz for 550 nm and 100 GHz for 240 nm, both at a drain voltage of 2.5 V. The current gain two exhibit an inverse relation to the cutoff frequency. This is one of the highest cutoff frequency reported for graphene-based FET devices. Devices based on GNR, however demonstrates higher performance characteristics.

The device performance of conventional graphene devices is usually degraded due to the damage caused to the monolayer graphene during the fabrication process. The graphene lattice is modified as a result and thus the values of carrier mobility and other important characteristics are lost. In order to counter this problem and thus enhance the device performance an innovative technique is reported in [64]. A schematic design of the device is as shown in the *Figure 31*. A self-aligned nanowire gate is deployed to avoid lattice damage. A $Co_2Si–Al_2O_3$ core shell nanowire is used as a gate. The channel length is the diameter of the nanowire and the drain and source are assigned through self-alignment.

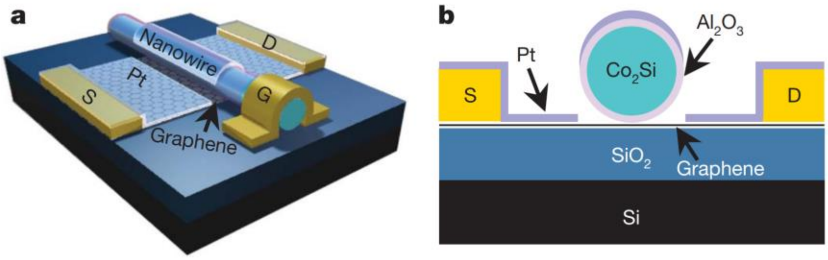

Figure 31: High Frequency RF Graphene nanowire FET: (a) top view with visible gate connection; (b) side view with nanowire cross section *[64]*.

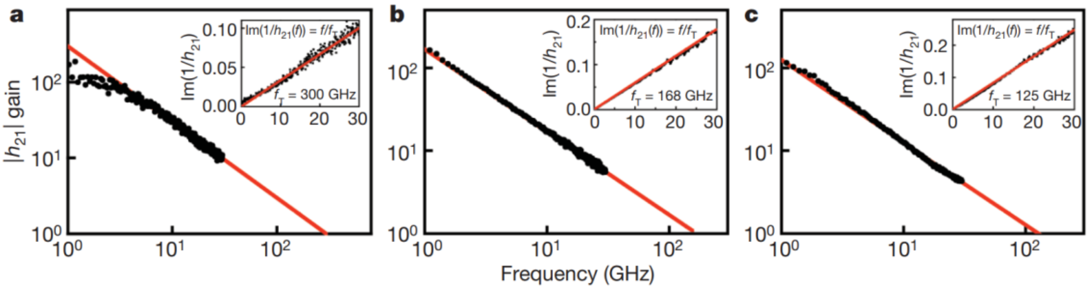

Figure 32:High Frequency RF Graphene nanowire FET cutoff frequency for different gate lengths: (a) 144 nm cutoff at 300 GHz; (b) 182 nm cutoff at 168 GHz; (c) 210 nm cutoff at 125 GHz. inset cutoff calculation by Gummel's method *[64]*.

Overlapping of the drain, source and gate terminals are avoided and there is sufficient gap in between them thus ensuring no degradation in carrier mobility and consequent device performance. The channel length of the device is 140 nm with cutoff frequency as high as 300 GHz. The device functionality is comparable with other high performance HEMT transistors with similar gate length. Other device performance characteristics are state of the art too. The most important frequency cutoff as measured for a variable small signal current gain is as shown in the *Figure 32*. It is evident from the figure that the gate length reduction result in a lower cutoff frequency.

Larger bandgap is always desirable for digital applications which does not exist in graphene. Graphene’s conduction and valence band overlaps and therefore there is no bandgap. One of the several methods to introduce bandgap in graphene is by making graphene nanoribbons. Graphene nanoribbons are thin strips of graphene usually of the order of tens of nanometers. The energy gap and width of nanoribbon are inversely related to each other and thus the smaller the width of the nanoribbon, the higher the energy gap. High frequency graphene nanoribbon FET has been reported in with frequency cutoff values as high as 30 GHz. In the FET, an array of parallel graphene nanoribbons of 100 nm and 50 nm wide is deployed [12].

2.3.2 Graphene Antennas

The use of antennas and passive microwave devices require dimensions multiple of the operating frequency. At microwave/mm-waves, it means very large dimensions usually of the order of several centimeters. Acquisition of nanomaterials in general and graphene in particular over such large dimensions has been very hard to obtain initially using conventional methods. This is the reason why graphene has not gained much interest in microwave passive devices including antennas. It was later that chemical vapor deposition was used, which ensured deposition of large dimensions of graphene usually of the order of several centimeters. Another very important setback for the use of graphene as an alternative to copper is that graphene is a moderate conductor with typical values of resistivity as high as 60 Ω/square. Copper on the other hand bears surface resistance equal to 0.03 Ω/square. Graphene, however is a very thin material (one atomic layer), assuming such a thin layer of copper (even though physically impossible) would provide similar if not worse values of resistivity.

Graphene has the ability to vary its conductivity values upon the application of a voltage bias. This provides a significant advantage over conventional materials for tunable antennas. An analysis of a patch antenna based on graphene was performed in [65]. It was shown through simulation results that even though graphene conductivity is not very high as compared to conventional metals still considerably good antenna performance could be achieved. The antenna was simulated in the frequency range 8-18 GHz. The resistance value of 2 KΩ, which is the resistance of graphene without any applied bias voltage is first considered. Simulation results show poor performance of the patch antenna for such values. Since graphene's resistance can be reduced by the application of a voltage bias therefore lower value of graphene resistance of 250Ω (assuming an applied voltage bias) are considered subsequently. Improved antenna performance and radiation characteristics are seen as a result. The simulated antenna efficiency reported is 0.73, which is comparable to conventional patch antennas.

In [13], the first prototype of graphene antenna is presented. The antenna is a slot antenna and is electronically tunable by an applied DC voltage bias. The antenna is coplanar fed which is connected to a graphene patch that is separated from the surrounded gold by the help of a slot. The topology of the antenna is as shown in *Figure 33*. The substrate used is a 500µm thick high resistivity silicon (HRSi) with a SiO_2 layer of 300 nm on top. The graphene used in the antenna is CVD grown commercially obtained with results of RAMAN spectroscopy showing very little defects. The antenna radiation characteristics are measured and the results obtained are impressive for a first attempt. The antenna reflection scattering shows wideband performance in the X band (8-12 GHz). For different values of applied bias voltage of 0V, 50V and 250V, there is a change in the S11. An improvement can be seen going from zero to 50V, while a further increase result in a reduction in

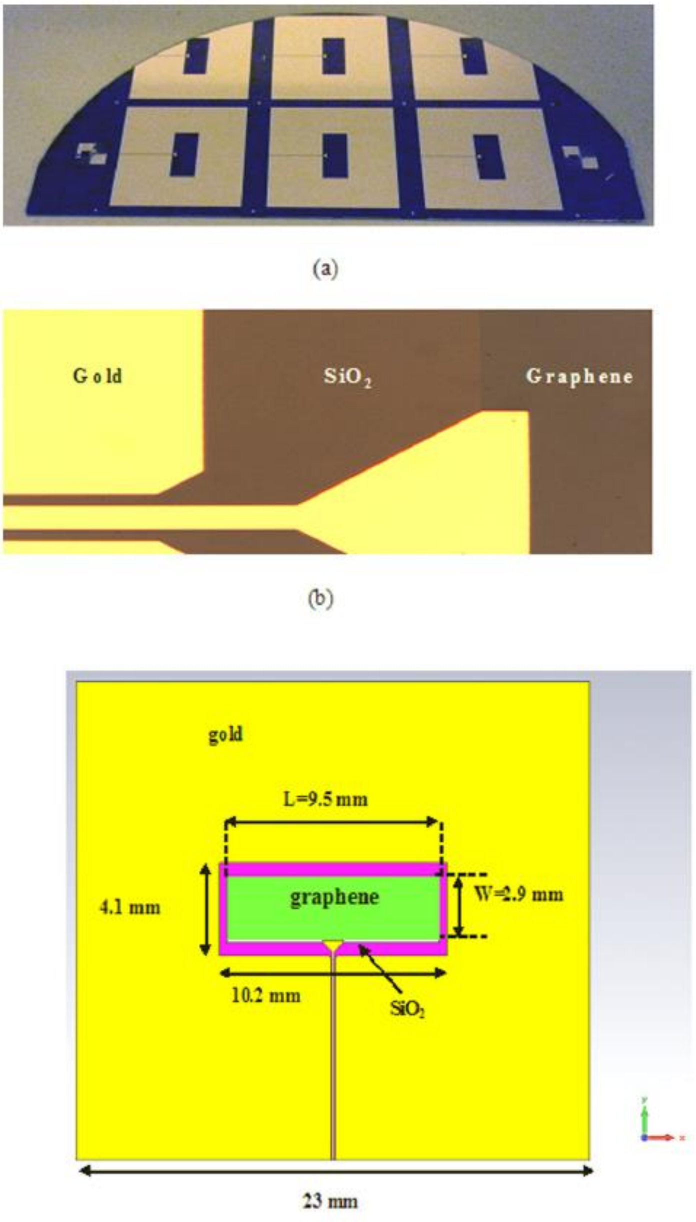

Figure 33: Graphene slot antenna: (a) silicon wafer with multiple antennas; (b) closeup showing graphene and coplanar connection to the antenna; (c) Topology of the antenna with dimensions *[13]*.

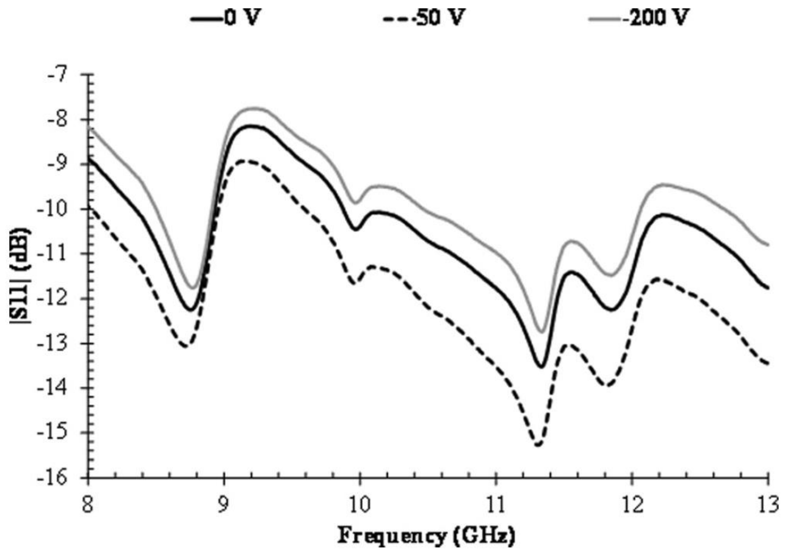

Figure 34: Graphene slot antenna reflection loss at different applied bias voltage *[13]*.

performance as shown in the *Figure 34*. The calculated sheet resistance from the measured results report that the corresponding sheet resistance for the unbiased case is Rs = 120Ω. The two main resonances fall at 8.74 GHz and 11.34 GHz. Comparing the performance to a similar metallic antenna, it is concluded that even though the performance of graphene antenna is slightly inferior to its counterpart yet the graphene antenna ensures wideband functionality unlike similar metallic antenna.

The tunable properties of graphene have also been exploited in several other antennas. Graphene can be incorporated in microwave passive circuitry along with antenna to tune frequency of radiation of planar antennas. For instance, in [14], which is a part of this thesis and will be discussed in detail later, graphene’s resistance change has been translated to a change in its reactance in order to mimic varactor diodes which are conventionally used to tune the radiating frequency of antennas. Graphene is put next to a radiating stub and the length and width of the stub had been modified so as to maximize a reactance change upon changing graphene’s surface resistance which can be performed by the help of an applied DC bias voltage.

2.3.3 Graphene EMI shielding Applications

Electromagnetic Interference (EMI) is a problem that effects a wide range of electronic applications ranging from automotive to aerospace and telecommunications. Shields are devices that avoid electromagnetic interference and are therefore of primary importance to all these applications. Novel materials have been exploited for acquiring superior shielding effectiveness parameters and graphene being one of the most important materials is no exception. Graphene is usually used as a binder in the form of composites in shielding applications. The composites are then tested for their percolation threshold values, a value that indicates the interconnection of the filler inside the matrix. The desirable behavior for a shield is to absorb electromagnetic wave impinging on it irrespective of its angle of incidence. Frequency bandwidth at which the shield works is also an important parameter to consider. Monolayer freestanding graphene is hard to obtain and using it as a binder in composites is not practical therefore it is desirable to use few layer graphene (FLG) and other thick graphene variations for composite production.

In [16], Exfoliated graphite and thick graphene has been used as filler in nanocomposite. It has been demonstrated that exfoliated graphite tends to form less agglomerates as compared to thick graphene and is well dispersed in the polymer matrix. Higher values of EMI shielding were obtained by using quantity of filler as low as 1-2%. An added benefit of EG nanocomposites is that they are extremely light and a very good alternative for conventionally used metals which are heavy and not suitable for used in aerospace applications. It has been shown that a 2% of EG nanocomposite of 0.5 cm thickness is capable of transmitting only 10% of the microwave signal impinging on it at 30 GHz.

Graphene has also been incorporated in heterostructures composed of pure monolayer graphene along with a polymer layer. In [66], it was demonstrated that CVD grown graphene on PMMA (poly methyl methacrylate) can give significant results for EMI shielding. In the study multiple layers of PMMA on graphene were considered. It was also demonstrated theoretically that the conductivity of alternate layers of graphene add up resulting in very high values of shielding effectiveness and electromagnetic absorption. A structure with six layers of graphene on PMMA demonstrated maximum absorption of 55% at 30 GHz. In experimental results, the absorption for 4 layers of graphene and PMMA is 40% with 30% transmission, the remaining 30% of the microwave power is reflected. An added benefit of this structure is that both PMMA and graphene are not only optically transparent but are also mechanically flexible, thus very good and practical contenders for microwave shielding applications. The study was performed for a number of layers ranging from one to twenty and it was shown that the maximum absorption is attained at six layers after which the performance degrades.

2.3.4 Graphene Microwave Attenuators

Attenuators are resistive components used to reduce gain in a circuit. Graphene being resistive and having the ability to change its resistance by the help of an applied bias voltage has been an excellent contender for use in microwave attenuators.

The larger dimensions of components at microwave frequencies like in the case of the antennas have been a bottleneck in the design of microwave attenuators with graphene. It was with the innovative technique of deploying the use of few layer graphene (FLG) flakes that this bottleneck can be easily overcome. With the increase in the number of graphene layers and their dimensions, the higher carrier mobility is lost since beyond ballistic regime comes into play. The interesting properties of ambipolarity and tunability, however remains intact. An added benefit of FLG is that they are easily produced and does not require any sophisticated and expensive equipment. In [15], a broadband graphene attenuator is proposed with prototype and measurements.

The attenuator topology comprises of a 50Ω microstrip line with a gap in the middle. The FLG are located deposited in the gap. The circuit is made by the help of a micro-milling machine and in this case the cutter used is of conical type which makes sure that the cut is made with a 45° slope. This makes sure that the FLG deposited afterwards are in contact with the microstrip line. A schematic representation of the attenuator is as shown in the *Figure 35*. It can also be seen that for biasing the FLG, broadband biastees are used on either side of the attenuator. With an increase in the applied bias voltage there is a reduction in the resistance of graphene resulting in a lower attenuation of the transmitting signal. Conversely, in the absence of any applied bias voltage, the resistance of graphene is high and the resultant attenuation is also high. In this way desired value of attenuation can be achieved by applying the right DC bias voltage. Graphene resistance can be simultaneously measured through the current drawn by the attenuator for each value of the applied bias voltage.

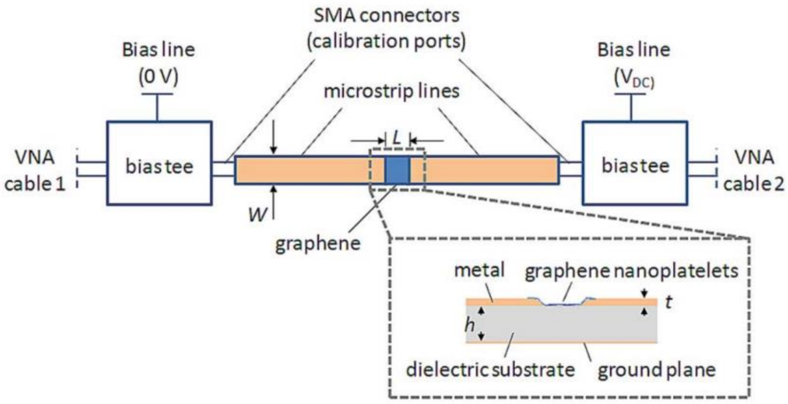

Figure 35: Measurement setup of Few layer Graphene Broadband Microwave attenuator. inset shows the side view where the cut with 45° slope is visible *[15]*.

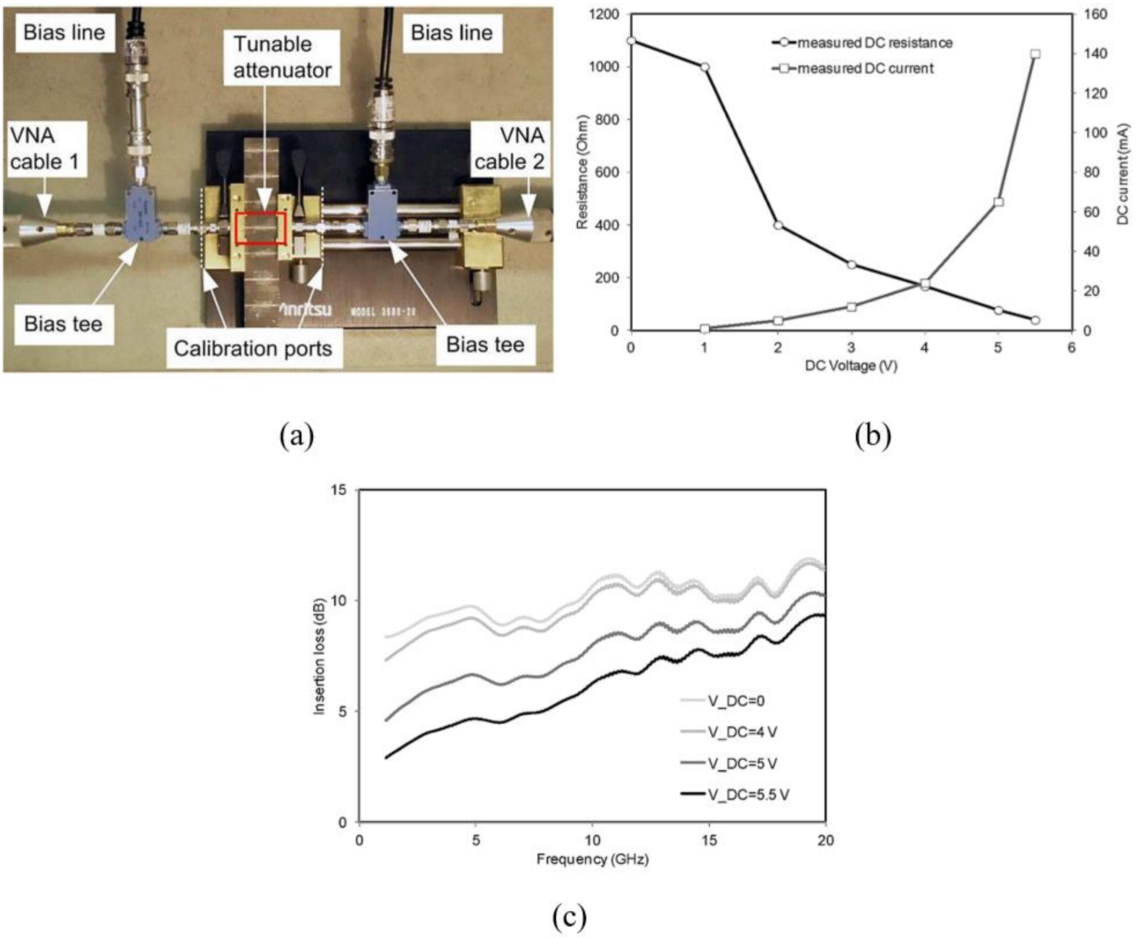

(a) (b)

(c)

Figure 36: Measured results of broadband graphene attenuator: (a) measurement setup; (b) DC applied bias voltage with resistance and respective current; (c) insertion loss at different applied DC bias voltage *[15]*.

Measurement setup of the attenuator can be seen in the *Figure 36 (a)*. The two important figures of merit of an attenuator are its insertion loss and reflection loss. It is always desired that the insertion loss is maximum with limited reflection loss. The minimum insertion loss and the dynamic range is also important. The DC resistance of graphene is measured from the current drawn by the attenuator and the applied bias voltage (Rs=V/I). It can be seen in the *Figure 36(b)* that as the bias voltage is increased there is a reduction in the resistance. The dynamic range of the resistance change is very wide. The insertion loss for the different applied bias voltage can be seen in the *Figure 36(c)*. The attenuator operates in a very wide band ranging from 1-20GHz and the tunability of the insertion is visible throughout the frequency band. Several improvements have been made to attain higher insertion loss and minimum reflection as a part of this thesis, which will be discussed in the following chapter.

More recently another type of graphene attenuator has been proposed in [67], which is based on a substrate integrated waveguide structure with graphene sandwich structure. The mode of operation is similar to the FLG attenuator in that the GSS SIW attenuator also exploits the change of graphene resistivity by an applied bias voltage in order to ensure tunable attenuation. The attenuator is composed of two parallel GSS structures inserted in a substrate integrated waveguide structure longitudinally as shown in the *Figure 37*. The two GSS are used as an E-plane septum in order to dissipate the electromagnetic field inside the SIW structure. The resulting transmission and reflection values are as shown in the *Figure 38*. The attenuator operates in the frequency band of 7-15 GHz with transmission ranging from -4 to -20 dB. It also ensures good values of reflection with maximum value of S11 below -15dB throughout the frequency band.

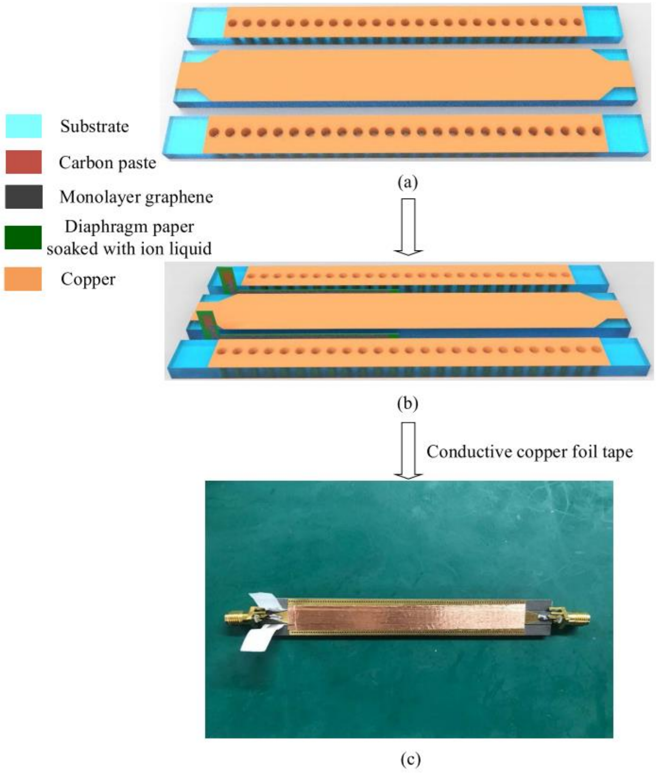

Figure 37: Graphene sandwich structure substrate integrated waveguide graphene attenuator: (a) top view with three sections;(b) side view topology of the attenuator with visible monolayer graphene; (c) Fabricated prototype *[67]*.

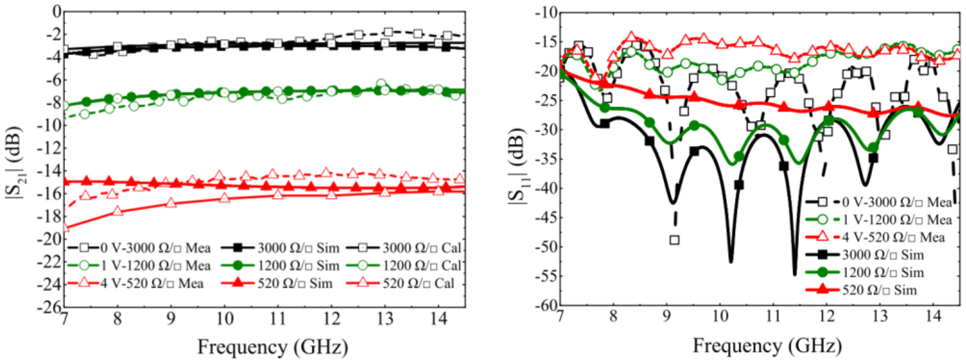

(a) (b)

Figure 38: Measured (dotted) and simulated (solid) values of GSIWA: (a) transmission; (b) reflection *[67]*.

Chapter 3

Tunable Graphene Attenuator

Among the very basic and important microwave components is the attenuator. Microwave Attenuators are components used to reduce the power of microwave signal. Attenuators are essential part of a number of other communication system components including modulators, gain control devices and radars. It is highly desired for attenuators to have a flat response so as the attenuated signal is least distorted. There are several types of attenuators including resistive line attenuators, π attenuators, Bridged-T attenuators hybrid coupled attenuators. The simplest among all these is the resistive line attenuator, which will be dealt with in this chapter.

Conventionally, in planar technology, the attenuators used are thin film resistors and PIN diodes. The use of novel materials including carbon-based materials have caught significant attention in the recent years. Among the carbon materials one of the most important is graphene. Apart from its high resistivity which is essential for attenuators, graphene has the property of changing its resistivity with a change in the surface charge density, which can be induced by the application of a DC voltage bias. This property can be exploited for use in tunable microwave attenuators. Conventional fabrication methods of graphene include exfoliation, epitaxial growth and chemical vapor deposition (CVD). Exfoliation is the mechanical separation of monolayer graphene from its 3D counterpart graphite. It was the first method used in the discovery of graphene. Epitaxial growth involves the thermal extraction of carbon from SiC. In this method the silicon atoms are sublimed from the surface of SiC. The third technique involves monolayer graphene is deposited by a chemical reaction on a metallic substrate. Graphene can then be transferred to other desired substrates.

Free standing single layer graphene is not only hard to obtain but also technologically demanding. However, the tunable resistive characteristics of graphene are present in multiple graphene layers with up to ten graphene layers [21], which has made multilayer graphene a very good contender for use in making cheap electronic and microwave circuits and systems. A very cheap and fast method to obtain multilayer graphene is by mechanical exfoliation. This is very attractive since mass production of components and systems has to be kept in mind in order to propose novel materials and methods. In the following the innovative and cheap technique for obtaining multi-layer graphene is described in detail.

3.1 Few Layer Graphene Flakes Fabrication

The method as first described in [68] involves the microwave irradiation of expandable graphite. The graphite obtained is commercially available and supplied by Asbury. It is a common practice to use expandable graphite for obtaining nanoplatelets of graphene. Expandable graphite contains sulfates and nitrates among the individual layers of graphene. Upon the introduction of a sudden thermal shock the intercalated substances tend to vaporize impacting the layers of graphene. The pressure exerted on the sides tends to expand the gap between the layers. A significant separation of the layers is caused resulting in exfoliated graphite material. In the procedure adopted here, the thermal shock is introduced by a microwave oven. The result is an increase in the temperature of up to 1000°C.

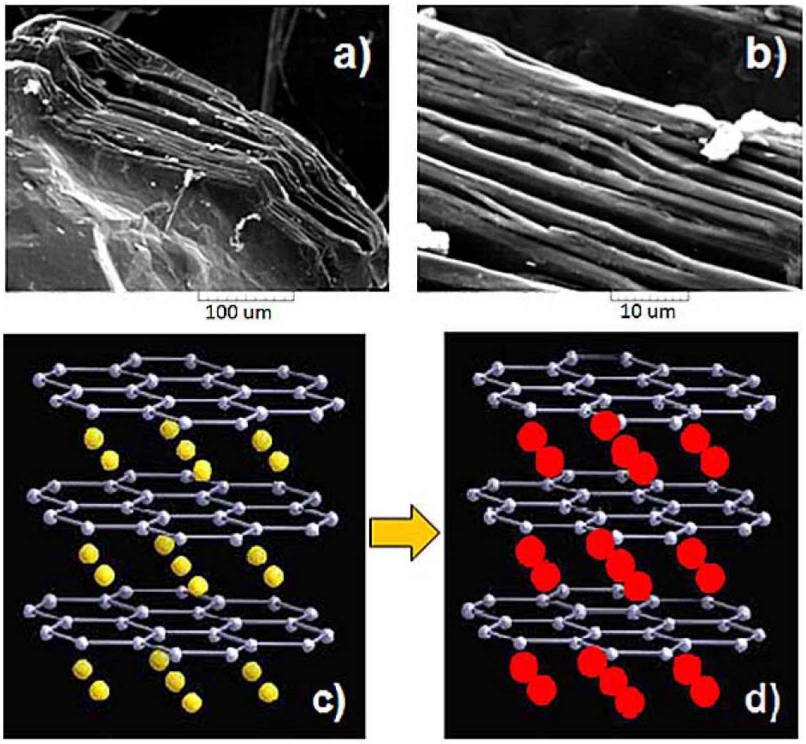

Figure 39: Microwave irradiation of expandable graphite: (a) SEM image before; (b) SEM image after; (c) schematic representation before; (d) schematic representation after *[15]*.

The vaporization of the intercalated substances tends to change the dielectric properties of air resulting in visible sparks. The sparks result in self feeding process inducing the acquired thermal process.

The use of microwave for heating and thus obtaining the exfoliated graphite is very advantageous in that it is a very fast and effective process besides being green. Green in a sense that no solvents or other heavy chemicals are required. Only 10 seconds of microwave irradiation is required to initiate thermal expansion. A description of the process along with the before and after microwave irradiation scanning electron microscopy (SEM) images are as shown in the *Figure 39*.

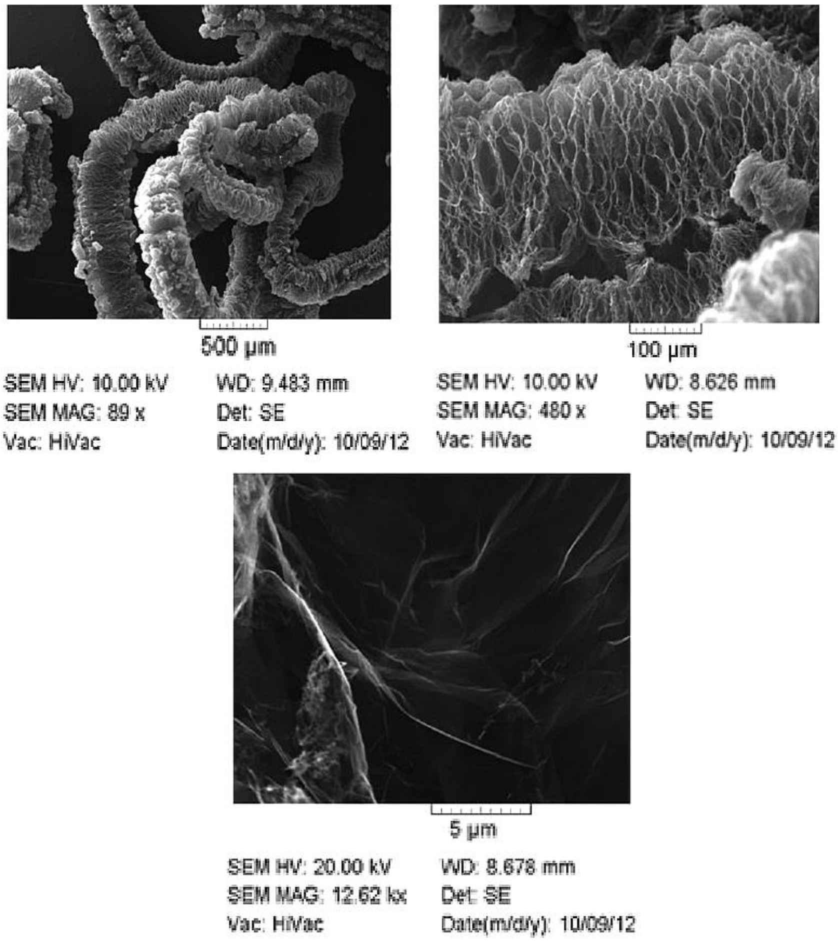

Figure 40: SEM images of worm like structures obtained after microwave irradiation of intercalated Graphite *[15]*.

After the microwave irradiation and the resulting thermal expansion, the intercalated graphite turns into worm like structures, which is a result of the contact of one side of the planes to the structure. The worm like structures are as shown in the *Figure 40*: the expansion of the intercalated graphite and the planes are also visible.

The next step is to ultrasound treat these worm-like structures in order to free the few layer graphene (FLG) from these worm-like structures. The first step in the ultrasound treatment is to mix the worm like structures in isopropyl alcohol followed by passing the solution through an ultrasound. The resulting mixture contains the quasi 2D flakes with planar dimensions of the order of tens of micrometers while the thickness is of several graphene layers typically less than 5nm. SEM images of free-standing flakes are as shown in the *Figure 41*. The last step in the process is to separate the flakes from the isopropyl alcohol in order to deposit them on a desired substrate. The solution containing both the isopropyl alcohol is drop casted on substrate. Isopropyl being volatile can be either left to evaporate at room temperature or the substrate on which the deposition is desired can be heated up to 100°C in order to speed up the process.

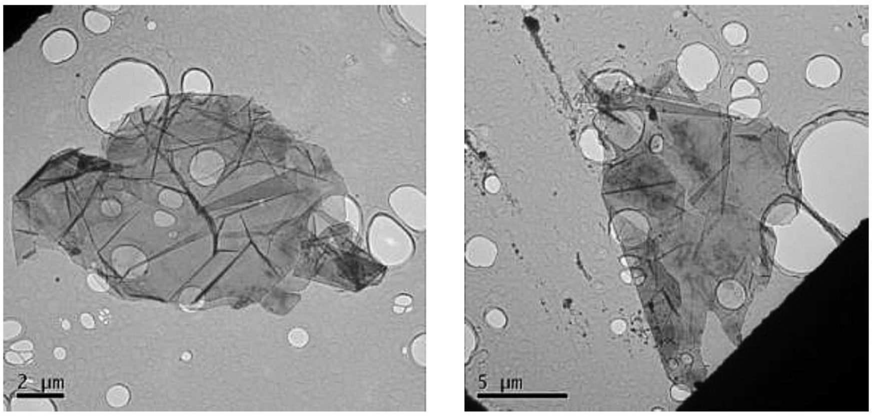

Figure 41: SEM images of free-standing graphene flakes with dimensions at the bottom for the sake of comparison *[15]*.

3.2 2-Post Shunt Graphene Attenuator.

The design of the attenuator as described in detail in the section 2.3.4 , (ref [15]) is based on a microstrip line with a cut in the middle. The cut or gap in the middle of the microstrip is where FLG are deposited. In order to better understand the mechanism a circuital representation of the topology is as shown in *Figure 42*. The working principle of the design is based on the graphene in the middle of the two 50Ω microstrip lines which acts as a variable resistor.

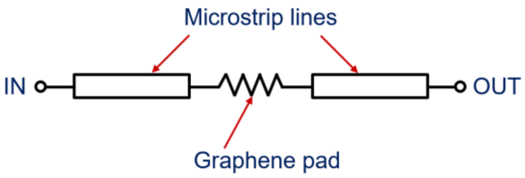

Figure 42: Series graphene Attenuator circuit topology

The signal passing through the microstrip line can be altered by changing the resistance of graphene. In absence of any voltage bias, graphene bears high resistance and as a result the signal passing through it is highly attenuated. When a DC voltage bias is applied to the graphene, the resistance of graphene is reduced and so is the attenuation of the signal. To sum up:

Low DC voltage → high R_g → high attenuation, and high DC voltage → low R_g → low attenuation.

The attenuator bears low dynamic range of insertion loss. The measured dynamic range of the insertion loss is 5.5 dB (from ~4.5 dB to ~10 dB). When the maximum DC voltage bias of 5.5 V is reached there is a breakdown of the FLG, which are able to dissipate a maximum DC power of 0.77 W (5.5 V with I_{max}=140 mA). After this breakdown the resistance of FLG return to their initial high value of ~1KΩ. The signal at this value is highly attenuated. Considering a case in which the maximum DC voltage is applied (either by human error or otherwise), the attenuator would always bear high attenuation and only a replacement could be the solution and not the addition of another attenuator to the current one. An improvement in the dynamic range of the insertion loss, analysis of the reflected and dissipated signal (as a part of the total attenuation) and to avoid highly attenuated signal in case of breakage it was desired to consider a parallel configuration of the *Figure 43*.

The functionality of the attenuator in this shunt configuration would be that initially without the application of a DC voltage, the resistance of FLG would be high. This high resistance would mean that the signal passing from port one to two would not be attenuated. When the applied DC voltage is increased the resistance of the FLG is reduced and the signal instead of passing through the microstrip from port 1 to port 2 tend to pass through the FLG into the ground causing attenuation in the signal. To sum up:

Low DC voltage → high R_g → low attenuation, and high DC voltage → low R_g → high attenuation.

In order to realize the shunt design a symmetrical structure is adopted in which the graphene pads consisting FLG are located between the microstrip line and a pair of grounded metal vias (*Figure 44*) [69]. At zero bias voltage across graphene, the pads exhibit high resistance and behave almost as open circuits, thus ensuring an almost complete transmission of the signal from port 1 to port 2.

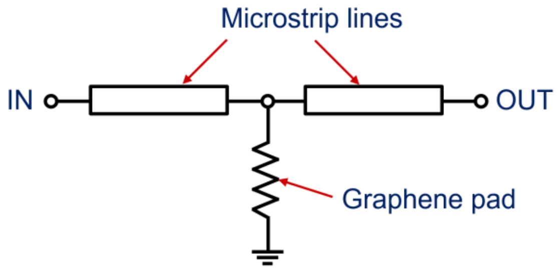

Figure 43: Shunt Attenuator circuit topology.

Increasing the bias voltage across graphene reduces its resistance, hence allowing more current to pass through it. This, in turn, attenuates the signal traveling through the microstrip line.

. The proposed topology of the graphene-based tunable microstrip attenuator is shown in *Figure 44*. The symmetrical mirrored configuration and dimensions of the graphene pad ensures higher and more stable attenuation in the frequency band of operation. The circuit is designed on CER-10 Taconic dielectric substrate with dielectric permittivity ε_r = 10, loss tangent tan δ = 0.0035 and thickness h = 1.27 mm. The microstrip line width was set to 1.17 mm in order to get a 50-**Ω** line. The dimensions graphene pads are: length=1.40 mm, width=0.66 mm, the radius of the metal via is 0.4 mm and the metallic pad around the via is a square of side 1.4 mm.

The proposed structure was simulated by the help of Ansys HFSS(commercial finite element modelling tool) in the frequency range of 0.01 GHz-5 GHz. In the simulations, the graphene pad has been modeled as single layer impedance. The simulations were performed for resistivity values ranging from 40 Ω/☐ to 1500 Ω/☐, similar to as done in [15].

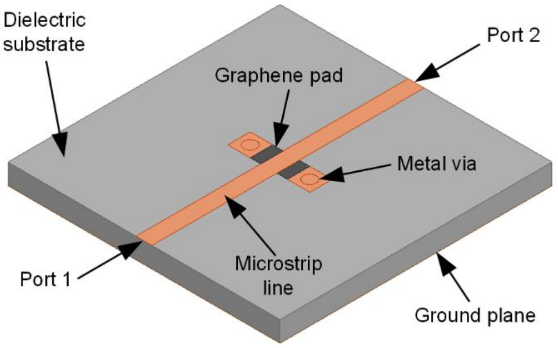

Figure 44: Graphene shunt attenuator-2 post design *[69]*.

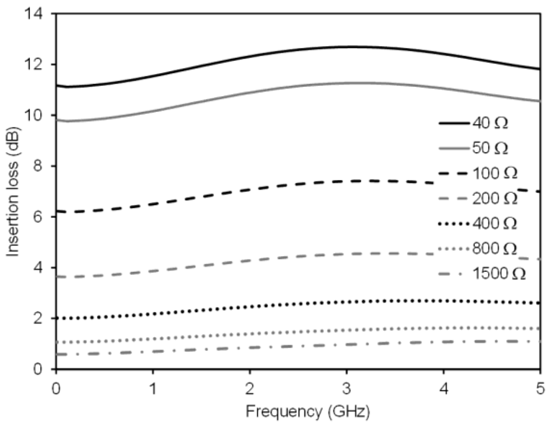

Figure 45: Simulated Values of Insertion loss for a number of Graphene resistance values *[69]*.

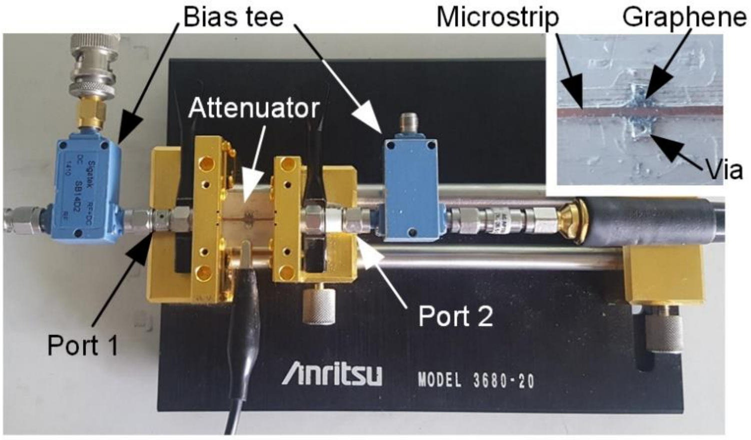

Figure 46:Photograph of the measurement setup with the tunable microstrip attenuator (close-up of the prototype in the top right corner) *[69]*.

As described in the modelling results, lower values of graphene resistivity results in higher insertion loss and vice versa., as shown in *Figure 45*. According to simulations, the maximum achieved insertion loss with a resistivity of 40 Ω/☐ is almost 12 dB while with a high value of resistivity of graphene equating 1500 Ω/☐ the minimum insertion loss of less than 1 dB is achieved.

Simulation results were promising and thus a prototype of the tunable microstrip attenuator was fabricated. The prototype is as shown in the inset of *Figure 46*. The prototype was fabricated by the help of an LPKF micro milling machine, with the metallic vias filled with conductive paste and then let to dry. The FLG was obtained by microwave exfoliation method as explained in detail in [15] and in the section 3.1. The testing of the prototype was performed by an Anritsu test fixture as shown in the *Figure 46* . The biasing of the FLG was done with the help of Commercial bias tees. Since the FLG are attached to the grounded vias therefore the bias voltage across the FLG was applied between the ground plane and the microstrip line.

Graphene resistance was calculated from the value of the current, I_{dc} drawn (measured using a DC multimeter) for an applied bias voltage, V_{bias}. The resulting graphene resistance is given by $R=V_{bias}/I_{dc}$. Graphene resistance plotted versus applied bias voltage is as shown in *Figure 47*. As expected, higher applied bias voltage results in reduced graphene resistance. Graphene resistance ranges from 1525 **Ω** at an applied bias voltage of 0 V (measured initially by ohm meter) to a minimum of 27 **Ω** at a maximum applied bias voltage of 6.5 V. Further increasing the bias voltage results in a breakdown of the FLG.

RF measurements were carried out along with the DC measurements as described above. The measurements were carried out by the help of a vector network analyzer in the frequency band of DC to 5 GHz at each value of applied bias voltage. The calibration of the vector network analyzer was performed at the ends of the connectors of the Anritsu test fixture in order to exclude any effects of the biastees. The measurement setup is as shown in *Figure 46*. In order to differentiate between the impact of the reflected and the dissipated insertion loss, the insertion loss at the frequency of 3 GHz is as shown in the *Figure 48* for each of the bias voltage applied across the FLG. There is a noticeable increase in the insertion loss with the applied bias voltage as expected in the simulation results. The dissipative insertion loss as a result is higher than the reflective one. The insertion loss ranges between 15 dB (at an applied DC voltage of 6.5 V) and 0.3 dB (at an applied DC voltage of 0 V).

Simulations post measurements were performed for measured values of graphene resistance in order to compare the simulated and measured results. The graphene resistance at each of the applied bias voltage is as shown in the inset of *Figure 47*. The measured insertion loss is compared to the simulated insertion loss, both at the frequency of 3 GHz as depicted in the *Figure 49*.

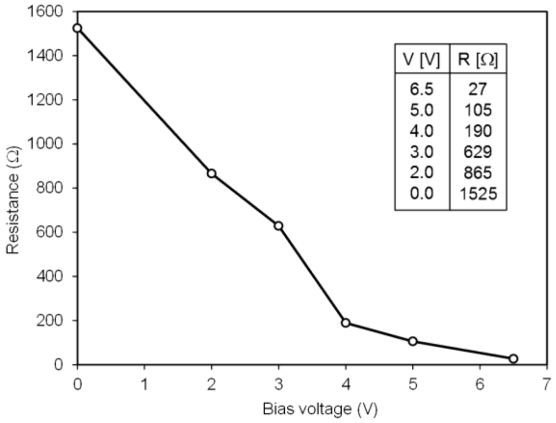

Figure 47: Measured graphene resistance versus bias voltage *[69]*.

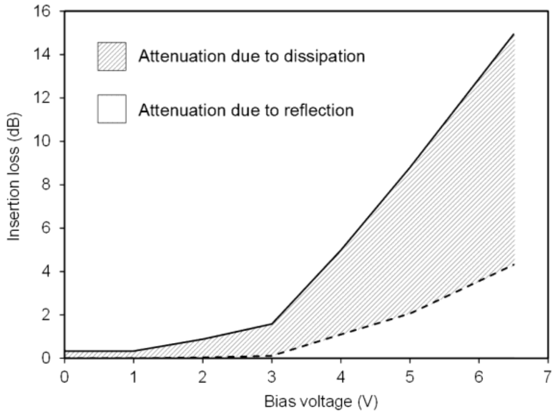

Figure 48: Measurement of the insertion loss vs. bias voltage at the frequency of 3 GHz *[69]*.

Finally, *Figure 50* shows the performance of the tunable attenuator over the entire frequency band from DC to 5 GHz. In particular, *Figure 50a* show the measured results versus frequency, for different values of bias voltage, and *Figure 50b* reports the simulation data computed for the resistance values corresponding to the set of voltages used in the measurements. It can be observed that the structure exhibits a stable wideband attenuation.

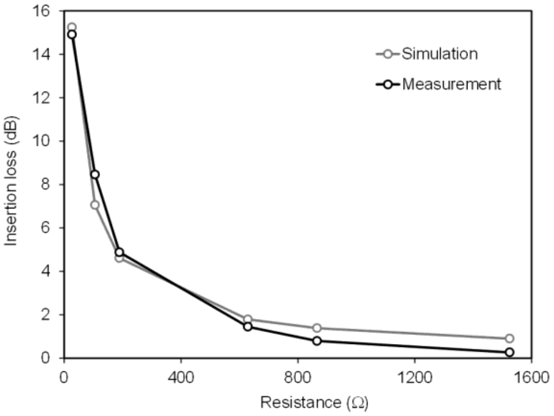

Figure 49: Comparison of simulated and measured insertion loss vs. graphene resistance at the frequency of 3 GHz *[69]*.

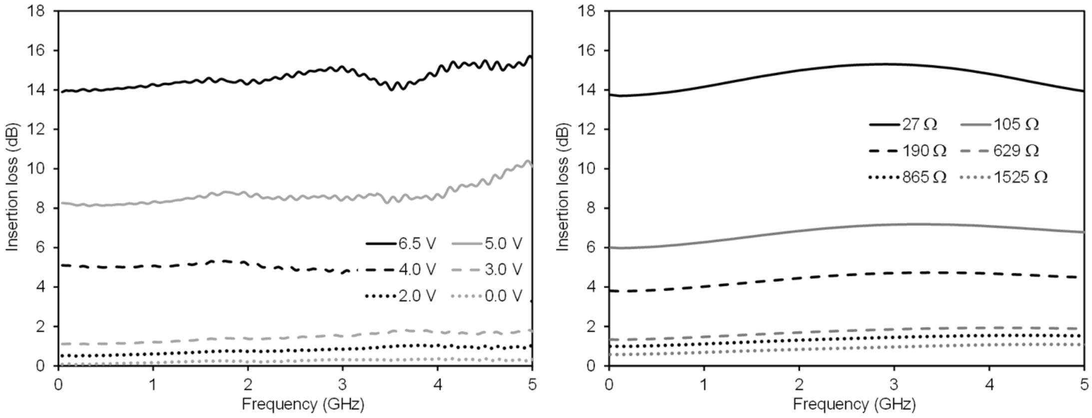

(a) *(b)*

Figure 50: Insertion loss vs. frequency: (a) measured results for different values of bias voltage; (b) simulation results for different values of graphene resistance (corresponding to the values of bias voltage adopted in the measurement) *[69]*.

3.3 4-post Shunt Graphene Attenuator

Going from the series to the shunt configuration was the first step in the acquisition of higher parameters of the figures of merit. One of the reasons why there has been a significant improvement in insertion loss is the increase in the total dimensions of FLG deposited which resulted in higher power dissipation. The number of graphene posts (depositions of FLG) were doubled going from the series to the shunt configuration. It is therefore suspected that a further increase in the number of posts would yield a further increase in the performance of the attenuator. It is pertinent to mention here that with the increase in the number of posts from 2 to four there is another complexity that comes into play, which is the length of the middle section of the line between the two couples. The length of the middle section thus needs to be optimized. The attenuator with four posts is as shown in the *Figure 51*.

The attenuator was designed on the Taconic Rf-60 dielectric substrate with thickness, h=0.64 mm with ε_r=6.15 and loss tangent, $\tan\delta$=0.0028. Simulations were performed with graphene flakes modelled as infinitely thin resistive sheets. The width of the microstrip line was kept at 0.94 mm in order to have a characteristic impedance of 50 **Ω**. The posts are grounded vias with length 1.40 mm and width 0.66 mm.

The 4-post attenuator is composed of two couples of grounded vias, one on each side of the microstrip line as shown in *Figure 51*. The vias need to be strategically placed in order to have a specific attenuation and a band of operation. For this purpose, three different values for the distance between each pair along the microstrip line have been chosen. Since the desired band of operation for the attenuator was chosen to be from 1 to 10 GHz, therefore the lengths were chosen to be multiples of the wavelength at the center frequency of 5GHz.

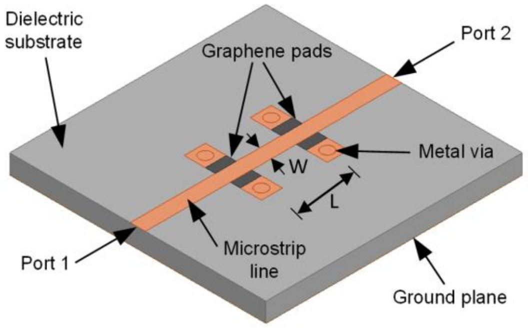

Figure 51: Microstrip attenuator with two pairs of graphene pads, spaced by a microstrip line section.

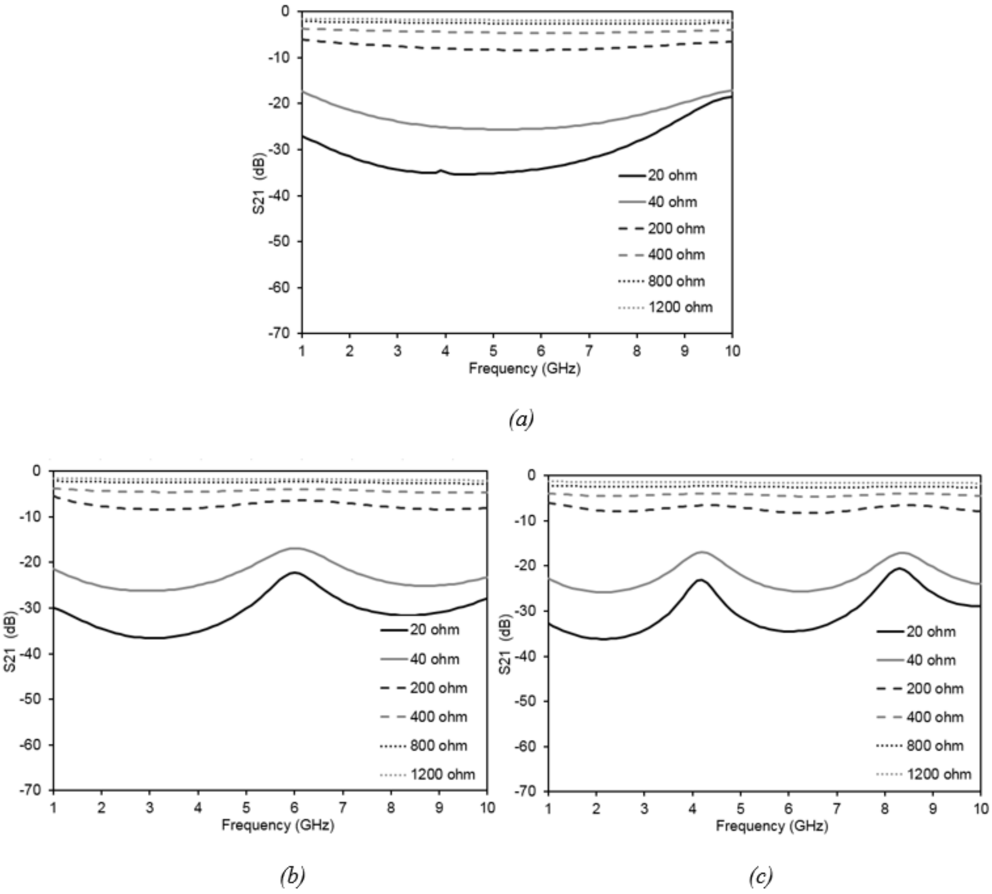

Figure 52: Simulation results of the midline length, L: (a) 5 mm; (b) 10 mm; (c) 15 mm

The values chosen were 5mm(λ/120), 10 mm(λ/60) and 15 mm(λ/40) respectively as shown in the *Figure 52*. Graphene flakes, here modelled as infinitely thin resistive sheet was assigned different values of resistance in the range of the actual graphene resistance in order to see the impact of the distance along the line on the transmission. It was observed that the case with the lowest distance of 5mm (λ/120) provides a flat and ripple free transmission in the complete band of operation as shown in the *Figure 52*.

In order to optimize the operation of the tunable attenuator, it was necessary to check the impact of the line impedance (in other words, the thickness, W, as indicated in *Figure 51*) of the central part of the microstrip line on the attenuation. The outer parts of the transmission line could not be different from 50 Ω to ensure matched connection to the ports. Three different thickness values, each corresponding to line impedance, 50 Ω, 75 Ω and 100 Ω were used for the central part of the microstrip line.

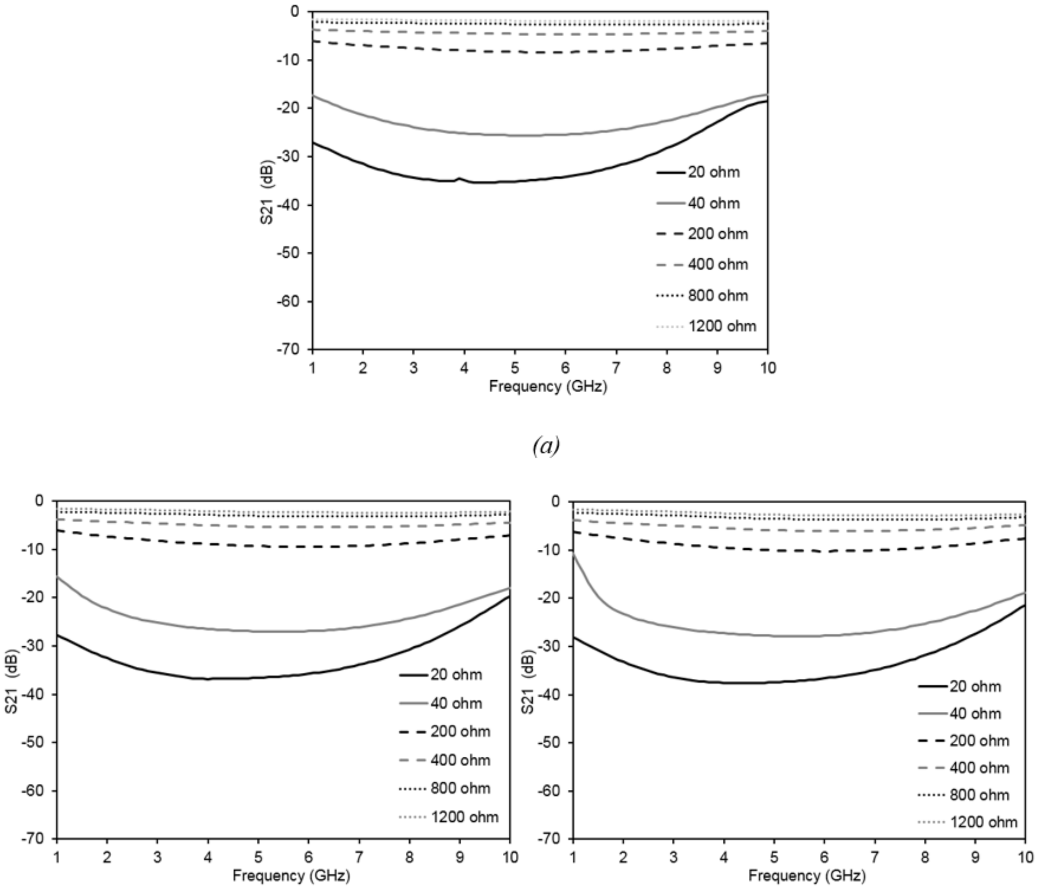

(a)

(b) *(c)*

Figure 53: . Simulation results of the midline impedance(width) variation: *(a)* 50 Ω, *(b)* 75 Ω *(c)* 100 Ω

The transmission scattering of each of which is as shown in the *Figure 53*. It can be seen that the thickness of the central microstrip lines have a very minimal impact on the complete operation of the attenuator and it only reduces the attenuation slightly, while keeping the dynamic range constant. As a result, going from a 50 Ω middle line to a 100 Ω middle line, the minimum attenuation is slightly increased and so is the maximum attenuation for the different values of the graphene resistance. Added to that is the fact that the distribution of the attenuation for the different graphene resistance values in the 50 Ω case is more uniform as compared to the other two cases. Since it is desired to keep the minimum attenuation low and the attenuation distributed evenly therefore, the optimum design of a uniform thickness of line impedance of 50 Ω was chosen for the entire microstrip line.

The analysis as shown in the *Figure 52*. and *Figure 53*, suggests that the distance between the vias be kept 5mm (λ/120) with uniform width of the microstrip line of impedance 50Ω in order to get least minimum attenuation that is evenly distributed for all the resistance values in the required band of operation.

Before the fabrication of the attenuator it was desired to compare it to the attenuator with two posts of the section 3.2. This comparison is as reported by the author in [70]. Looking at the simulated insertion loss results of the *Figure 54* of the two and four posts respectively, it can already be deduced that the functionality of the four posts is already superior to the one with the two posts. In the case of the 2-post design, the insertion loss of the attenuator ranges from 1 dB for a maximum graphene resistance of 1500 Ω to 12 dB at graphene resistance of 40 Ω. This gives 11-dB tunability in the frequency band from DC to 5 GHz. In the case of the 4-post design the minimum attenuation in the simulated results shows a value of 1.5 dB for a value of graphene resistance equivalent to 1500 Ω, while the maximum attenuation at a graphene resistance of 40 Ω is 25 dB. Hence, the total tunability in this case, as demonstrated by the simulations results in 23.5 dB. In this case, the frequency response is fairly constant from DC to 10 GHz, which is twice as that of the previous 2-post design.

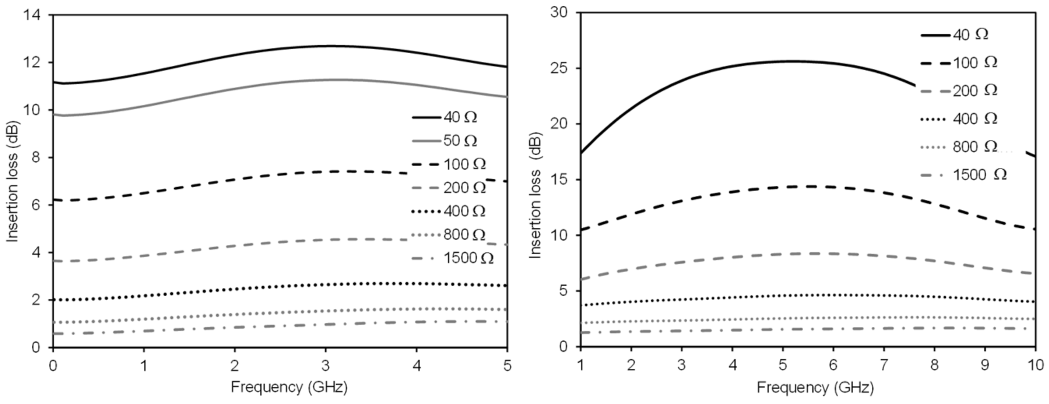

(a) *(b)*

Figure 54: Insertion loss versus frequency: (a) 2-post (b) 4-post *[70]*.

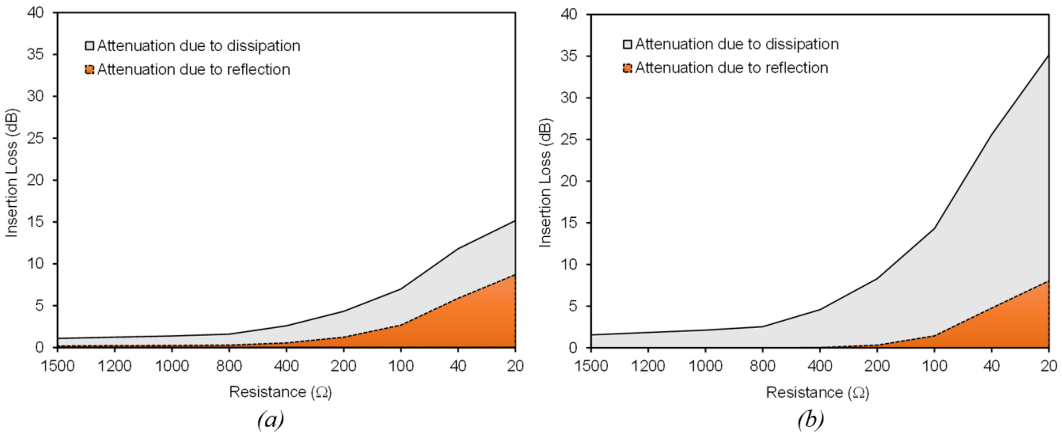

Figure 55: Reflected and dissipated power vs the graphene resistance at the frequency of 5 GHz: (a) simulated results for the 2-post design; (b) simulation results for the 4-post design *[70]*.

It is not yet known whether the insertion loss is due to reflection or dissipation. It is always desired that the dissipative part of the reflection of an attenuator be higher that its reflective part. Therefore, a comparison of the reflective and dissipative parts of the total insertion loss for the two cases was necessary before the fabrication of the prototype. Simulations were performed with Graphene flakes modelled as infinitely thin resistive sheet with assigned values of resistances in the range of actual values. The insertion loss at a common frequency if 5 GHz for a range of different graphene resistance is as shown in the *Figure 55*. The independent contribution of the reflective and dissipative attenuation is also evident. It is notable that even though the total insertion loss has been significantly increased yet the reflective part is kept low and the major contribution is from the dissipative part.

As shown in the *Figure 55*, in the 2-post design, at lower resistance of 20 Ω (where the insertion loss is maximum), the total attenuation is 14 dB, with 6 dB dissipation and 8 dB reflection. While in the case of the 4-post design, a total attenuation of 14 dB is achieved with a resistance of 100 Ω. In this condition, the contribution of dissipation is 12.6 dB and the contribution of reflection is only 1.4 dB. Moreover, the total attenuation can be further increased by further reducing the value of graphene resistance to 20 Ω: in this case the total attenuation is 35 dB, with 27 dB dissipation and 8 dB reflection.

Hence the prototype was fabricated with the design parameters formerly mentioned. The Prototype is as shown in the *Figure 56* Graphene flakes were deposited after the fabrication of the prototype and measurements were carried out by the help a VNA (vector network analyzer) as in the case of the 2-post attenuator. The graphene flakes were biased by the help of a bias-tee and the change in resistance as expected was observed, which resulted in a change in the attenuation of the transmission parameters.

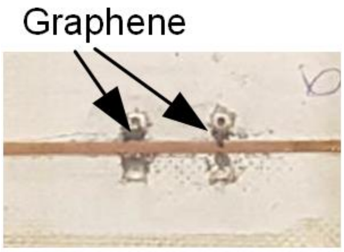

Figure 56: Prototype of the graphene-based microstrip attenuator with two pairs of graphene pads (4-posts) *[70]*.

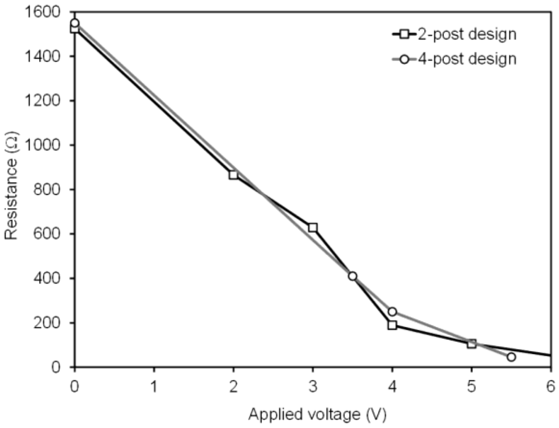

Figure 57: Comparison of the DC resistance versus applied voltage for the 2-post design and the 4-post design *[70]*.

The change in resistance was calculated from the current drawn for each applied voltage bias. It was noticed that with an increase in the applied voltage bias the resistance of graphene reduced, thus increasing the attenuation of the signal on the microstrip line. In order to have comparable resistance values for simulations to that of the measured resistance. *Figure 57* shows the measured graphene resistance versus DC bias voltage, for the attenuators with 2 posts and 4 posts. Increase in the bias voltage results in a decrease in the graphene resistance. It can also be noticed in *Figure 57* that there is a good agreement in measurements for 2-post attenuator and the 4-post attenuator.

The measurement results of the insertion loss versus frequency, for different values of bias voltage, are reported in the *Figure 58*. In particular, *Figure 58(a)* shows the data for the 2-post design, whereas *Figure 58(b)* shows the new data related to the 4-post design. The measured values are in good agreement with simulation data for both types of the tunable microstrip attenuators. While measured data are parametrized with voltage (*Figure 58*) and simulation data are parametrized with resistance, the two sets of curves can be compared by using the results of *Figure 57*.

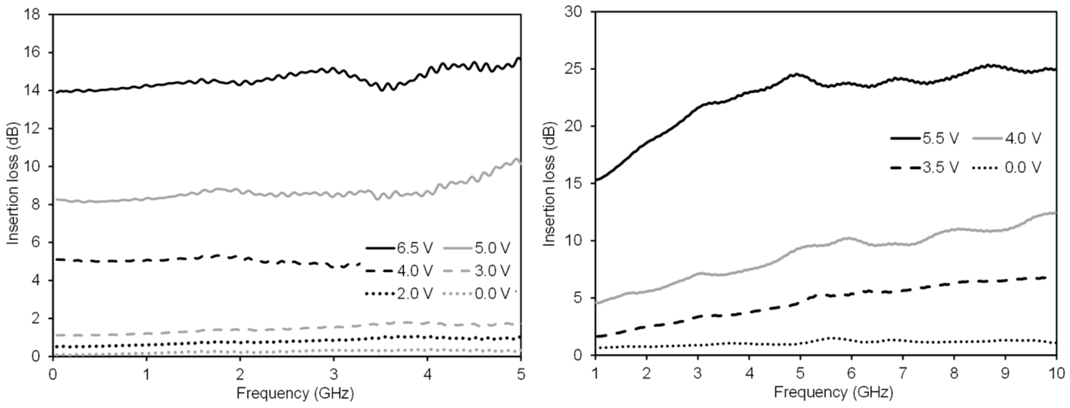

(a) *(b)*

Figure 58: Insertion loss vs. frequency: (a) measured results for different values of the applied bias voltage in the 2-post design; (b) measured results for different values of applied bias voltage in the 4-post design *[70]*..

The attenuator with 4-post, proposed in this work, exhibits a tunability of 23 dB as compared to 14 dB of the 2-post attenuator of section 3.2. Moreover, the 4-post attenuator operates in a band of 10 GHz, twice as wide as that of the 2-post attenuator. In conclusion, a general comparison of the performance of the two attenuator is shown in *Figure 59*, which report Simulated and measured insertion loss and reflection loss versus resistance at the frequency of 5 GHz. It results that, for a similar value of graphene resistance, the insertion loss in the case of the 4-post design is clearly higher than that of the 2-post design.

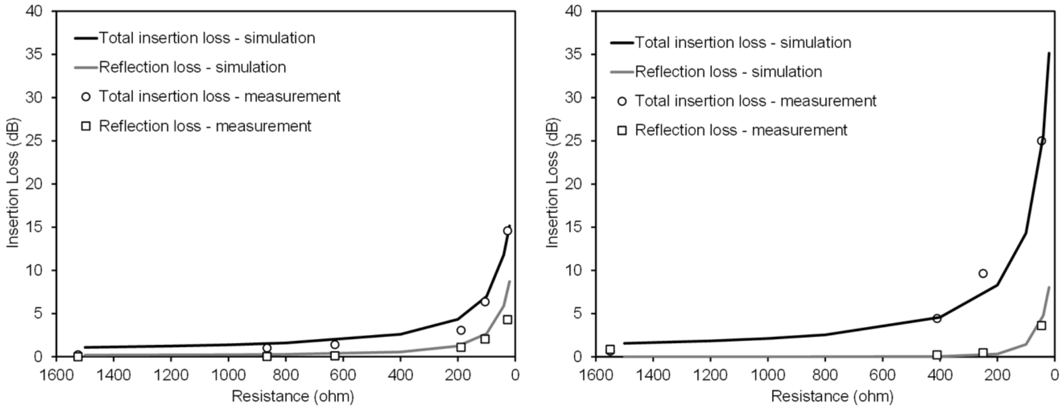

(a) *(b)*

Figure 59: Simulated and measured insertion loss and reflection loss vs. resistance at the frequency of 5 GHz: (a) 2-post design; (b) 4-post design *[70]*.

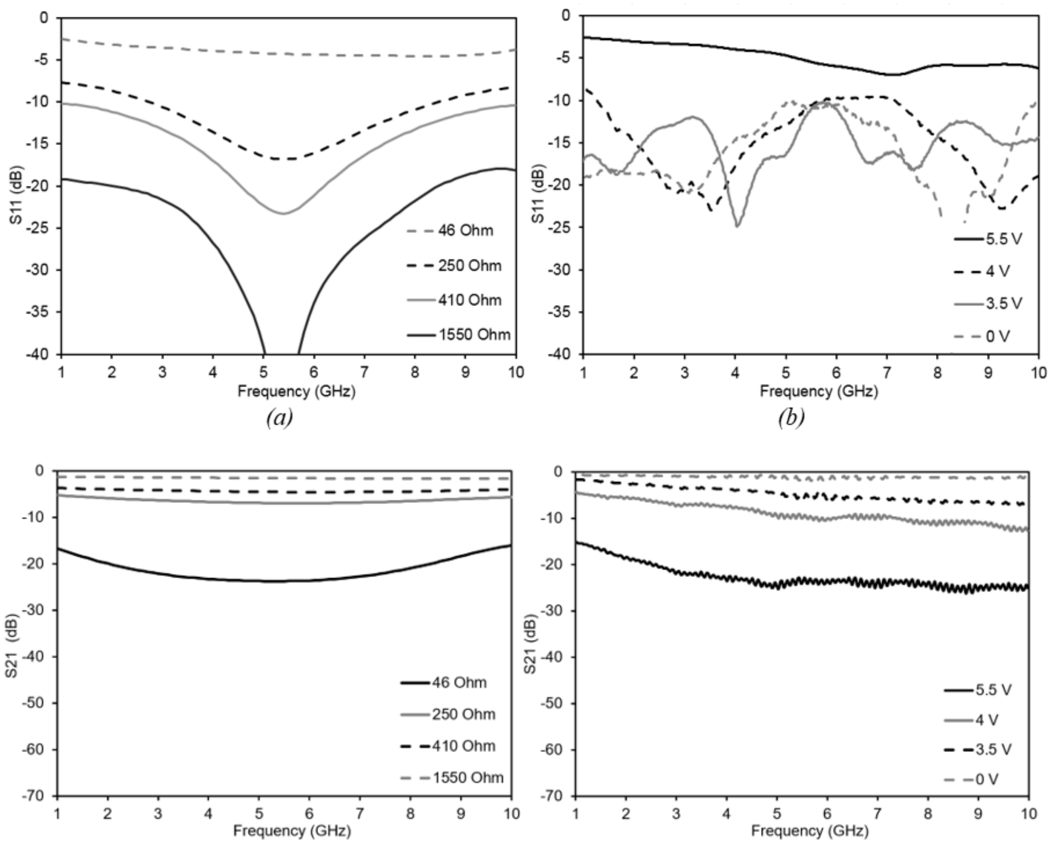

(a) (b)

(c) (d)

Figure 60: 4-post Graphene attenuator simulated and measured results: *(a)* Simulated S11; *(b)* Measured S11; *(c)* Simulated S21; *(d)* Measured S21.

To sum it up, the simulated and measured values of both the reflection and transmission scattering parameters for the 4-post attenuator are as shown in *Figure 60*. For sake of comparison among the simulated and measured results, the resistances for which the simulated results are shown are the corresponding values of graphene resistances at the applied voltages for which the measured results are demonstrated. There is a good agreement between the simulated and measured results. It is worthwhile to see that the S11 throughout the entire band remains below -10 dB except for the high applied voltage of 5.5 V. The maximum achieved S21 is almost 20 dB and the response is almost flat over the entire band.

3.4 6-post Shunt Graphene Attenuator

It was expected that an increase in the number of posts would result in an even higher attenuation in the transmission scattering parameters of the graphene attenuator. Therefore, the number of posts were increased to a total of 6 (3 pairs), three on each side of the microstrip line as shown in the *Figure 61*. The lengths and widths of the central section of the microstrip line have been optimized for the 4-post design and they are kept as such.

In this case the lateral dimensions of the graphene pads: g1, g2 and g3 as shown in the *Figure 61* will be optimized. The effect of the dimensions of the graphene pad on the transmission scattering parameters needed to be analyzed. Reduction of 80%, 60% and 40% in the values of *g1* and *g3* i.e., for 80%, *g1=g3=0.8g2*, for 60%, *g1=g3=0.6g2 and* for 60%, *g1=g3=0.6g2* was performed as a first case. and its effect analyzed. It can be seen in the *Figure 62* that the decrease in the *g1* and *g3* result in an increase in the total attenuation. It is pertinent to mention here that the minimum attenuation is also gradually increased going from 80% to 40%. In short a decrease in *g1* and *g2* (while keeping *g3* constant) result in an increase in the maximum attenuation but doing so also increases the minimum attenuation. It is however desirable for minimum attenuation to have a least value possible with overall high dynamic range for the attenuation. The change in in the dimensions for the 40% case induces a sort of asymmetrical S21 with the least value shifted to a lower frequency as evident from *Figure 62 (c)*.

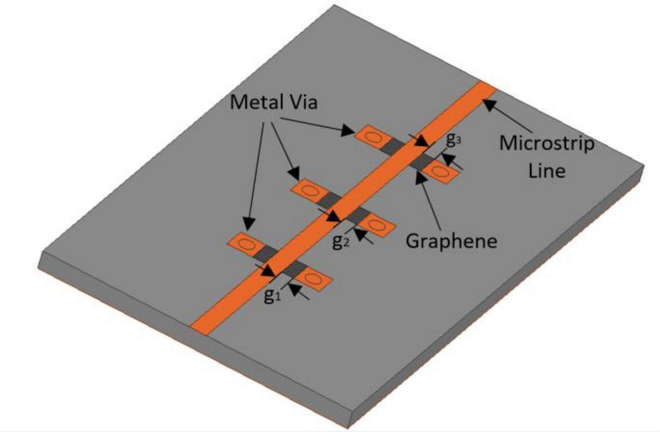

Figure 61: 6-Post Graphene attenuator.

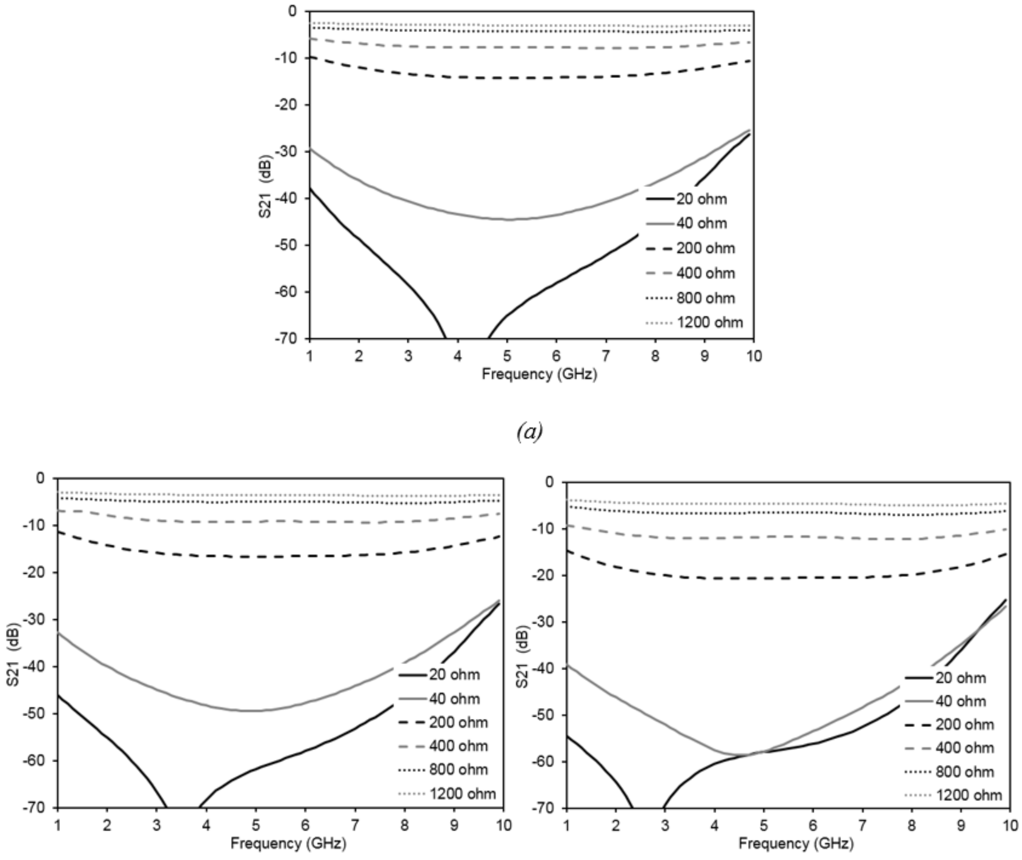

(a)

(b) (c)

Figure 62: Simulation results of the transmission scattering parameter S21 of the outer graphene pads dimensions (g1 ang g3) reductions (a) 80% of the central pad, g2; (b) 60% of the central pad,g2; and (c) 40 % of the central pad, g2.

In order to check the impact of the inner graphene pad's dimensions, the reduction in dimensions of the inner pad (*g2*) needed to be analyzed as well, and for that, a similar method was adopted i.e., to perform a reduction in size of 80%, 60% and 40%, where $g2=0.8g1=0.8g3$, for the case with 80% reduction, $g2=0.6g1=0.6g3$, for the case with 60% reduction and $g2=0.4g1=0.4g3$, for the case with 40% reduction. The results of the transmission scattering parameter for the three different cases for various graphene resistances are as shown in the *Figure 63*. The impact of the central pad lateral size, *g2* reduction is similar to the outer pads (*g1* and *g3*) size reduction in that both increases the maximum signal attenuation while increasing also the minimum attenuation (S21 at least value of graphene resistance). In both the cases a slight asymmetry is also caused in the S21, which is not desirable.

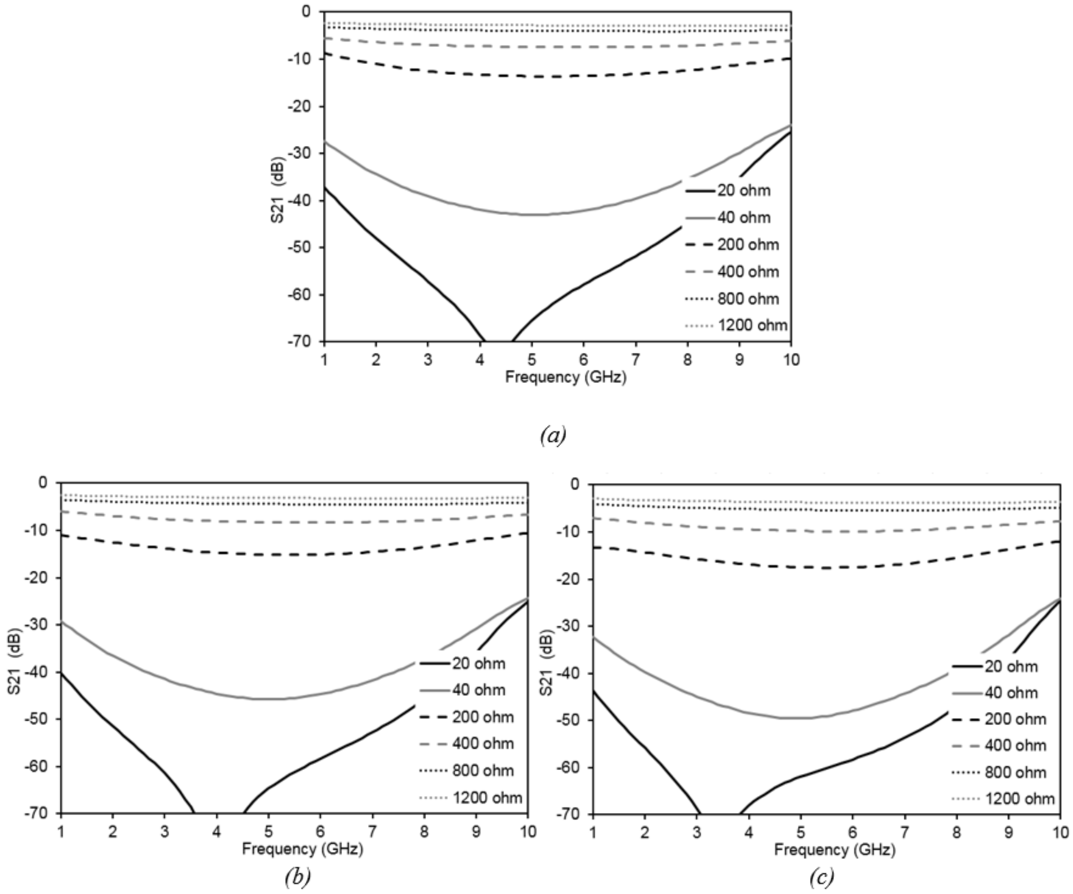

(a)

(b)

(c)

Figure 63: Simulation results of the transmission scattering parameter S21 of the inner graphene pad dimensions, g2 reductions (a) 80% of the outer pads, g1 & g3; (b) 60% of the outer pad,g1 & g3; (c) 40 % of the outer pad g1 & g3.

The size reduction or reducing *g2* causes slightly less impact on the attenuation, which is because the impact is caused to only two pads while in the case of the outer (g1 and g3) reduction causes the 4 Pads to have smaller dimensions. Hence it is concluded that the number of pads with reduced size has a higher impact on the minimum and maximum attained attenuation than its postion along the microstrip line. Since the reduction in dimensions caused higher values of the minimum attenuation, hence the reduction in pad size was not performed for the prototype fabrication. As a result all the dimensions of graphene depositions were kept of the same size.

The prototype of the 6-post attenuator was fabricated as shown in the *Figure 64* and measurements were performed. Since the reduction in dimensions caused higher values of the minimum attenuation, hence the reduction in pad size was not performed for the prototype fabrication.

Figure 64: Prototype of the tunable attenuator with 6-posts.

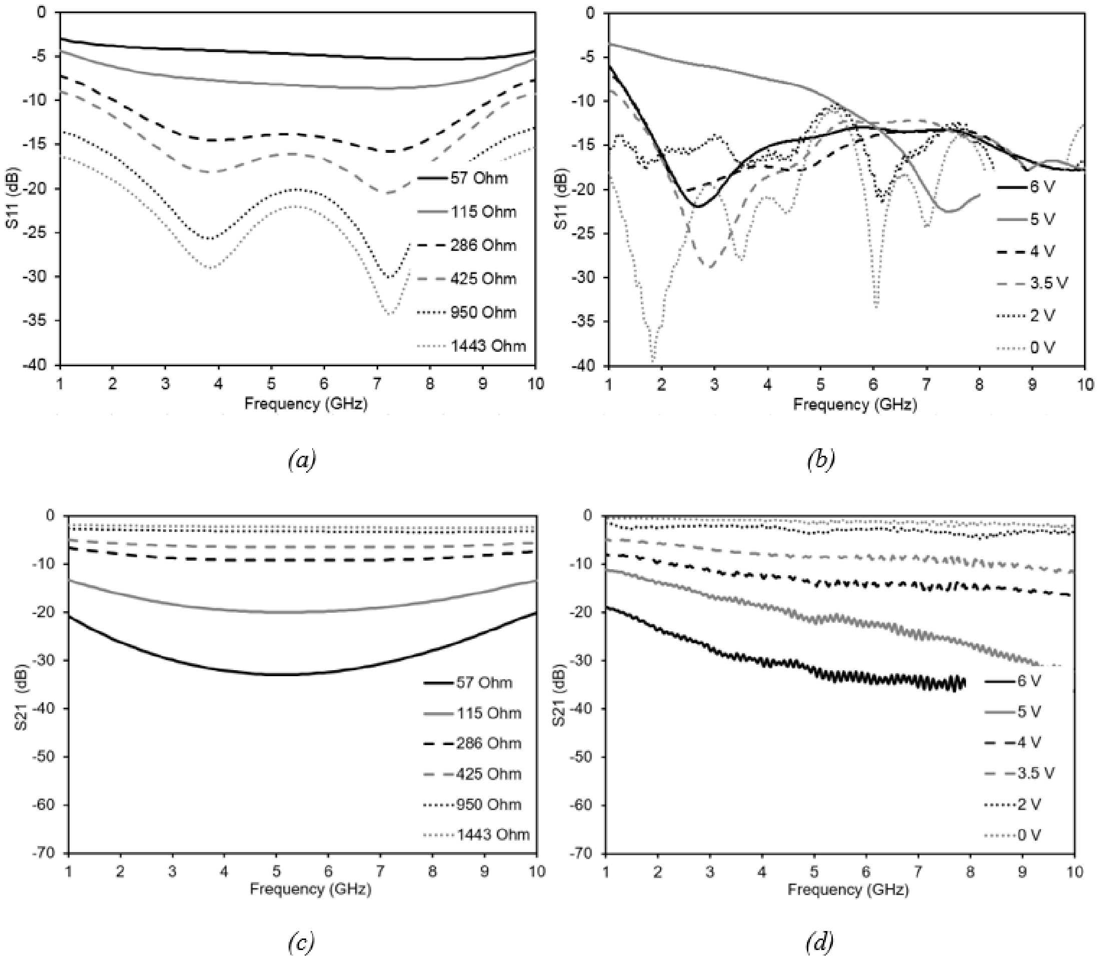

(a)

(b)

(c)

(d)

Figure 65: Simulated and measured results of 6-post attenuator: (a) simulated S11; (b) Measured S11; (c) Simulated S21; (d) Measured S21.

The measurements of the transmission scattering parameters are as shown in the *Figure 65* along with the simulations with the assigned graphene resistance values for the corresponding voltage values. It can be seen that the measured and simulated values are comparable. In comparison to the attenuator with two pair posts, the attenuation has further been increased. The values of the reflective scattering as shown in the *Figure 65(a)&(b)* shows low values, which for most of the frequency band and most applied voltages is below -10 dB. The transmission scattering of the *Figure 65(c)&(d)* for the simulated and measured values respectively show an almost 30 dB of maximum attenuation in transmission.

In order to get a clearer picture of the dissipative and reflective contributions of the total insertion loss, the values of the respective contributions should be plotted at a single frequency for a range of different applied voltage bias in case of measured results or assigned graphene resistances in case of measured results. To this aim, the reflective and dissipative power loss has been plotted in the *Figure 66* at the centre frequency of 5 GHz.. It can be noticed that even though the attenuation has been increased, the reflective power is still kept low and is just a very small fraction of the total power loss. The maximum measured insertion loss in this case is around 35 dB with the maximum reflection as low as 5dB.

The results from simulation and measurements indicate that the increase in the number of vias and the graphene pads not only increased the total attenuation but also helped in dissipating most of the attenuated power. This is enough motivation to further increase the number of vias carrying the design as optimized for the 6-post and the 4-post. In the following a graphene attenuator with a similar design and increased number of vias and graphene pads will be discussed.

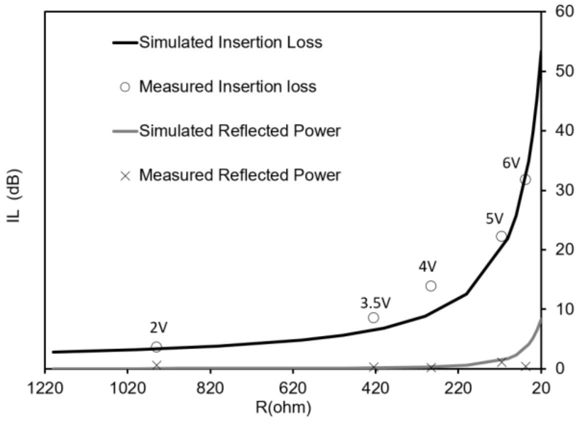

Figure 66: Insertion loss versus graphene resistance with both reflective and total insertion loss. Applies Bias voltage values indicated.

3.5 8-post shunt Graphene Attenuator

Having obtained an optimum configuration through rigorous analysis based on various design parameters of both the microstrip line and the graphene deposition it was expected to attain even further attenuation keeping reflections low by increasing the number of posts. A structure along similar lines was thus simulated with 8 total number of grounded, four on each side of a 50Ω microstrip line, all connected to the microstrip line via pads where few layer graphene is to be deposited. The proposed structure is as shown in the *Figure 67*. For simulations of the said structure, the graphene flakes were modelled as infinitely thin resistive sheets just as in the previous case of the 6-post attenuators. Simulation results were promising and showed an even further increase in the attenuator performance parameters.

As a result, a prototype of the proposed simulated structure was fabricated and graphene flakes were subsequently deposited. The fabricated structure is as shown in the *Figure 68*. The attenuator was fabricated by the help of the micromilling machine as in the previous cases. Graphene flakes were also deposited by a similar method as in the previous cases. For measurements, the prototype was measured by the help of a VNA. The ports of the VNA are connected as indicated in *Figure 67*. The graphene flakes resistance was measured by measuring the current drawn by the structure at an DC applied voltage bias *(R=V/I)*. Simultaneous measurements of the scattering parameters were also performed. A comparison of the measured and simulated scattering parameters is as shown in the *Figure 69*.

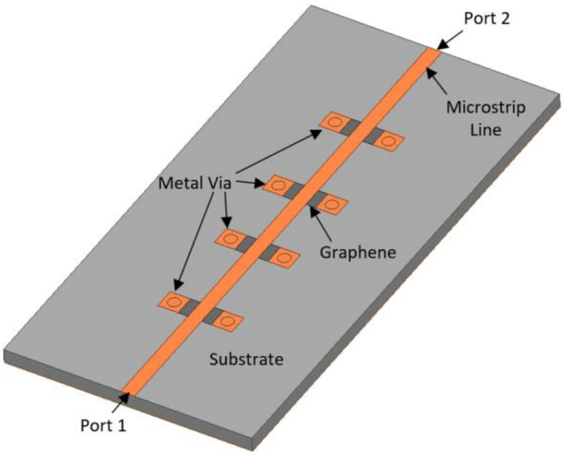

Figure 67:Topology of Graphene Tunable Microstrip Attenuator with 8 posts.

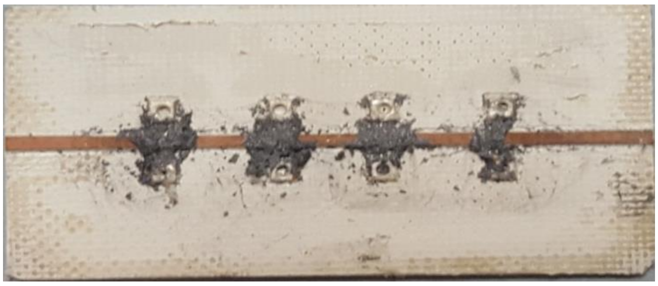

Figure 68: Prototype of the tunable attenuator with 8- posts.

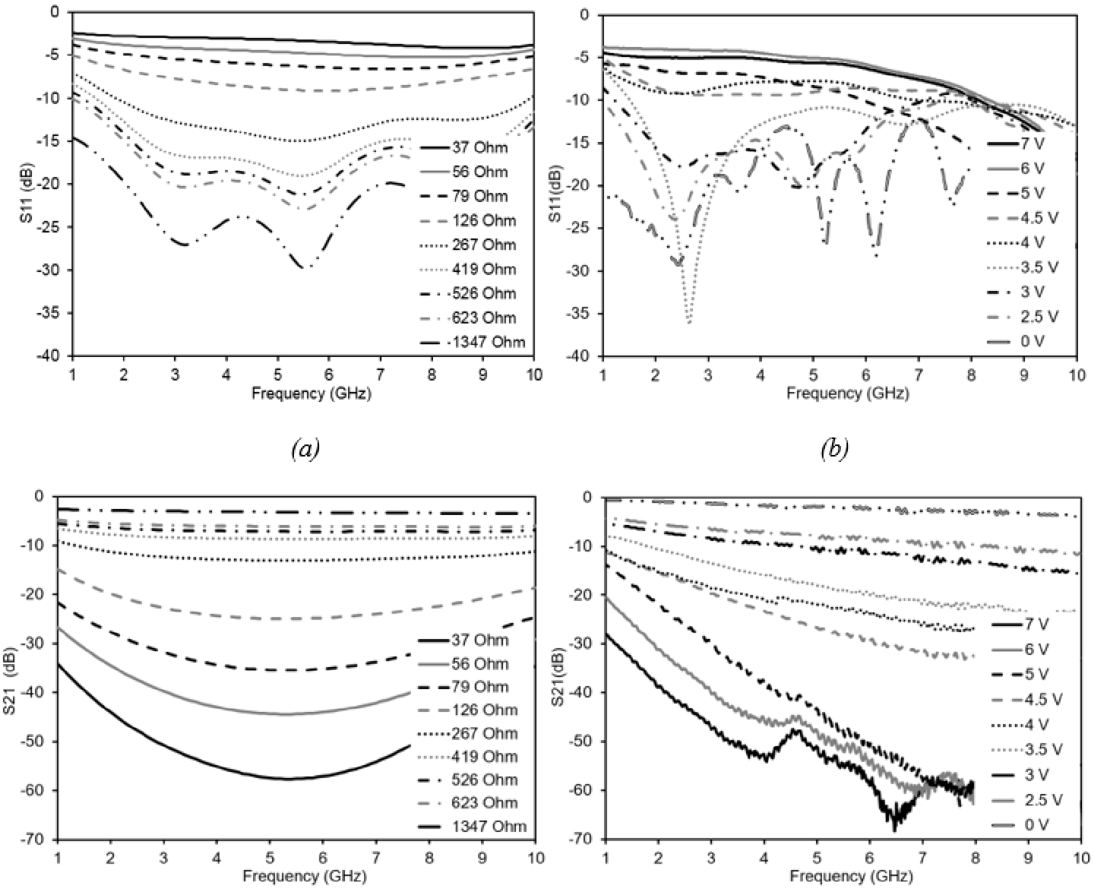

(a) *(b)*

(c) *(d)*

Figure 69: 8-post Attenuator measured and Simulated results: (a) Simulated S11; (b) Measured S11; (c) Simulated S21; (d) Measured S21.

The values of the resistances in the simulated S11 and S21 of the *Figure 69* are the values of graphene resistance at the applied DC bias voltages as shown in the measured results. It is noteworthy to see that the values of S11 are considerably low for a range of applied DC bias voltages and the values go above -5dB only when the DC applied bias voltage is as high as 6V. At the same applied bias voltage the S21 has a considerably higher value of more than 25dB. These are extremely high values for such attenuators. It means that for a desired minimum reflection still decent amount of attenuation can be obtained. These are very significant improvements over the previous case of the 6-posts as shown in the section 3.4. Maximum attenuation that is measured is more than 50dB for more than half of the bandwidth for applied DC bias voltage of 5,6 and 7V. The values are as predicted in the simulation results. The least reflection simulated and measured is less than -25dB which is at an applied DC bias of 0V corresponding to graphene resistance of 1347Ω.

Finally, in order to compare the value of the insertion loss at a single frequency, which in this case is taken at the centre of the bandwidth and is 5GHz, the value of insertion loss is plotted against the resistance as shown in the *Figure 70*. Both simulated and measured values are indicated. The applied bias voltage for the insertion loss values are also indicated. The maximum measured insertion loss at an applied bias volatgr of 7V is almost 65dB corresponding to a graphene resistance of 37Ω. The most interesting thing to notice here is the almost invisible reflective part of the total insertion loss, which maximizes at less than 10dB for a simulated graphene resistance of 20 ohm. The maximium reflective insertion loss measured at 7V corresponding to 37 ohm graphene resistance is 2dB.

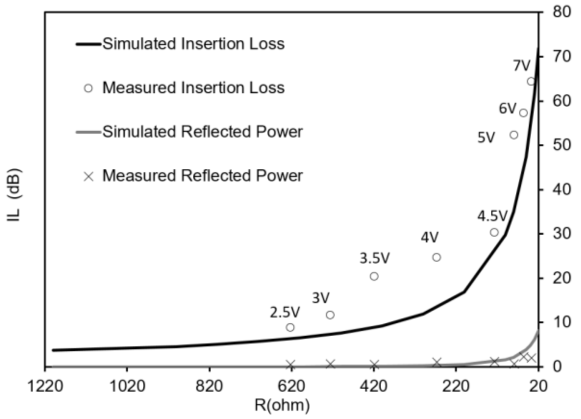

Figure 70:Insertion loss versus graphene resistance of the 8-post attenuator, measured and simulated values indicating the reflected power as well as the applied DC bias voltage.

3.6 Comparison of Attenuator Topologies and their performance

The four different topologies as proposed in this chapter are a form of evolution of the graphene attenuator with the performance of each newly proposed attenuator better than the previous one in terms of not only the maximum and minimum attenuation but also the reflective attenuation as demonstrated from the measured results of each of the attenuators. Since with each newly proposed attenuator a new parameter of dimension emerges, be it the length of the middle section of the microstrip line or the dimension of graphene pads, therefore the optimization of the new design parameter with increase in complexity has been performed.

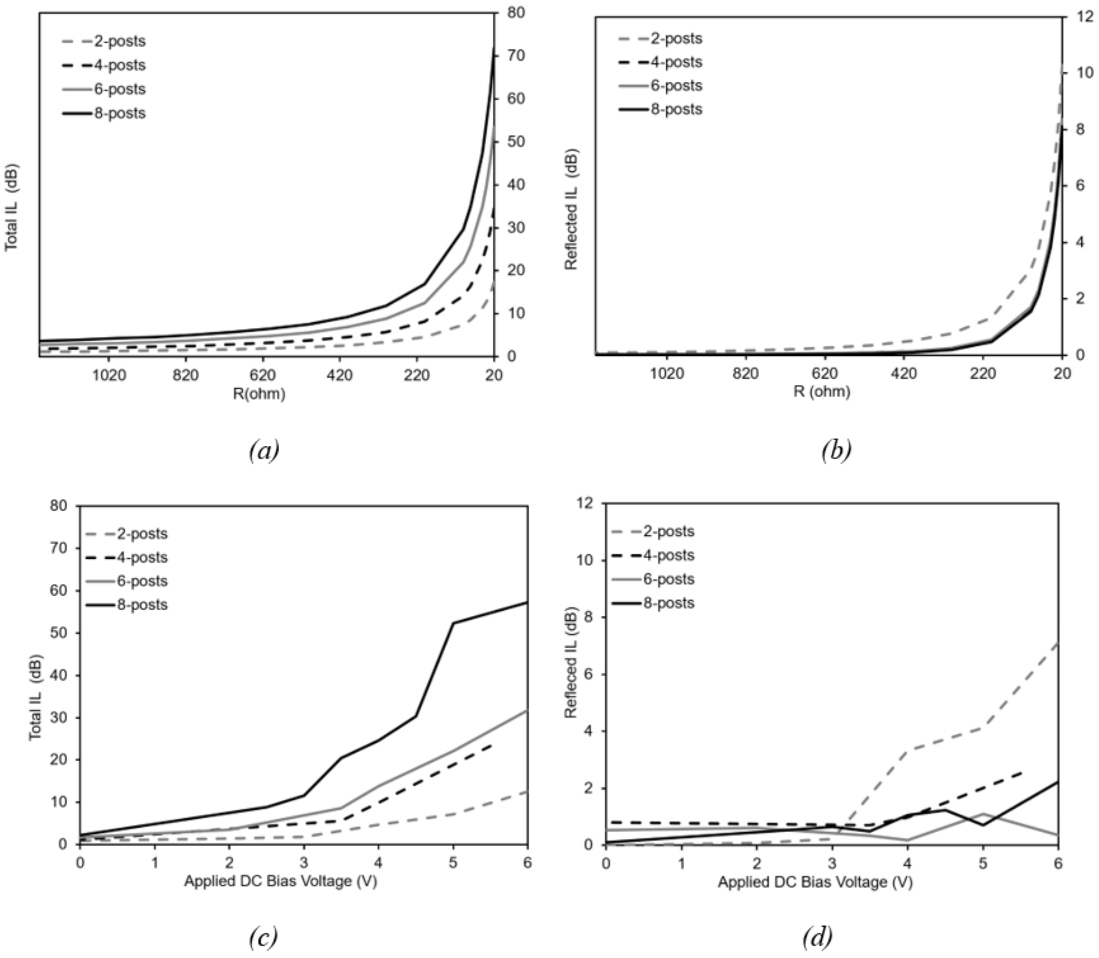

(a) *(b)*

(c) *(d)*

Figure 71: Total and reflective insertion loss for the Tunable attenuators with increasing number of posts: (a)&(b) simulated values with assigned graphene resistance; (c)&(d) Measured values with applied DC Bias voltage.

This resulted in an optimized design in each step and in the end an ultimate optimized design. The performance indicators show a gradual increase in performance which demonstrates this evolution.

A comparison of the total insertion loss and its reflective part for both the simulated and measured results have been reported in the *Figure 71*. Specifically, the simulated results of the *Figure 71(a)* and *Figure 71(b)* are shown with assigned graphene resistance values corresponding to the values of graphene resistance measured with the applied bias voltages as shown in the *Figure 71(c)* and *Figure 71(d)*. It can be seen that there has been a considerable increase in the total insertion loss while going from attenuator based on 2-posts to the one with 8-posts. The maximum attenuation as seen goes from approximately 20 dB to more than 50 dB, which is almost 4-folds increase. To the advantage of the design it is pertinent to mention as reported in the *Figure 71(d)*, that the only considerable increase in the reflective attenuation is when the number of posts are increased from 2-pairs to 4-pairs. Going further from 2-pairs to 4-pairs, the reflective attenuation is kept constant while the total insertion loss is drastically increased.

Chapter 4

Tunable Graphene Phase Shifter

Phase shifters are microwave components used to provide desirable phase change in the transmission scattering parameter, S21 in a two-port network. Phase shifters bear fundamental importance in a wide range of microwave systems like electronically steerable antennas of phase array systems, frequency translators and in adjusting phase noise caused by power amplifiers. The far more common application of phase shifter is in phased array antenna system. Each component of the antenna array needs an excitation signal with a different phase. Since the excitation to each of the radiating components should bear a gradual phase shift therefore the use of a phase shifter in such case is of primary importance.

The two most important characteristics of a phase shifter are: i.) the differential phase change and ii.) the insertion loss variation. The former should be as maximum as possible with the later as minimum as possible. Another main characteristic is the bandwidth and the response of a phase shifter in its bandwidth, the flatter it is the better. The three main control mechanisms of phase shifters are electronic, mechanical and magnetic. While there are a number of ways to implement a phase shift in passive components, the easiest way in order to introduce a phase shift in a signal is through switches and transmission lines as in the case of a trombone line which is a mechanically elongating transmission line causing variable phase shift. The principle of its operation is that, the signal transmitting through a longer transmission line would possess a higher phase value than a shorter one and will be shifted in phase as compared to the first one. Electronically controlled phase shifters are the most common since they can be easily embedded into transmitter/receiver systems.

The use of novel materials for phase shifters is not new. The concept of varactor diodes for phase shift have now been deployed in materials having the same capacitive variation effect for innovative phase shifters. The capacitance of such materials usually changes by an applied bias voltage which is then translated into a phase change. Nonlinear dielectrics and ferroelectrics based on materials like Barium Strontium titanite (BST) [71], [72] and Hafnium Oxide (HFO_2) [73] have also been used in a number of configurations as dielectrics and as thick and thin films for electronically tunable phase shifters. Schottky diodes based on graphene have also shown to provide phase shift as in [74]. In this chapter, we will deal with a new and very simple technique in order to exploit the resistance variation property of graphene in order to obtain an electronically tunable phase shifter.

4.1 Design of the Phase Shifter

The larger dimensions and technological simplicity of FLG make it suitable for use in microwave circuitry and phase shifter is no exception. The introduction of a delay in a transmission line causes a shift in the phase of the transmission signal. For this purpose, the FLG based phase shifter is composed of a 50 ohm two-post transmission line connected to a stub through a tapered line and FLG depositions. A change in the resistance of the FLG by the introduction of a Bias voltage causes a net change of reactance at the end of the taper. This introduces a delay in the transmitting signal causing a phase shift. The tapered line is separately analyzed through simulations for providing a maximum change in reactance upon a change in graphene resistance. A prototype of the optimized design in the frequency band of 5-6 GHz is fabricated and measured results are discussed.

The design of the phase shifter proposed is as shown in the *Figure 72*. The phase shifter is designed on a Taconic RF-35 substrate. The substrate has relative dielectric permittivity, $\varepsilon r = 3.5$ and loss tangent, $\tan \delta = 0.0018$. The thickness of the substrate is, $h=1.52$ mm. The phase shifter comprises of a stub and a two-port transmission line. The detailed design of the stub is as shown in *Figure 73*. The two-port transmission line has a width of 3026 mm corresponding to line impedance of 50 **Ω**. The stub comprises of a tapered section, FLG and a shorted stub. The stub width is 1 mm corresponding to 100 **Ω** characteristic impedance. The stub is shorted at one end by the help of a grounded via that has a diameter of 1 mm. The other end of the stud is connected to FLG that has length, $g=0.66$ mm and width, $w=1$mm.

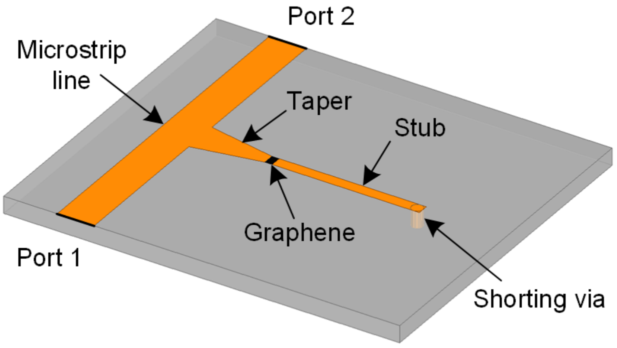

Figure 72: Geometry of the graphene-based tunable phase shifter.

4.2 Design of Tunable Stub

The stub comprises of a tapered line connected to a shorted stub via FLG as shown in *Figure 73*. The tapered line is of similar width as the transmission line at one end and of width equal to the shorted stub width, w at the other. The tapered line has length, L_2. The shorted stub has length, L_1 and width, w. The stub input impedance is Z_{in}. For electronic tuning, the FLG resistance is to be exploited by an applied bias voltage, therefore the lengths of the tapered line, L_2 and the shorted stub, L_1 need to be optimized so as to get a maximum variation of $Im\{Z_{in}\}$ when the FLG resistance is varied by a DC bias. Simultaneously, the variation in $Re\{Z_{in}\}$ is kept as low as possible in order to limit the insertion loss.

For optimization of the lengths, L_1 and L_2 according to the above-mentioned criterion, simulations are carried out assigning them a range of different values. The simulations are performed by the help of commercial Finite element modelling tool, HFSS. Both the imaginary and real part of input impedance, Zin are plotted against graphene resistance (ranging from 0 to 1500 Ω, assigned as sheet resistance) at the frequency of 5 GHz, which is the design frequency of the phase shifter. The analysis is based on assigning four different possible values to L_2 for each value of L_1. This process is repeated for four different values of L_1 and a total of 16 different combinations are considered as shown in the *Figure 74*. The best case among the lot is the one for which the variation in $Re\{Z_{in}\}$ is minimum and the variation in $Im\{Z_{in}\}$ is maximum for the range of graphene resistance. The best case is the one with L_1=12 mm and L_2=6 mm. It is evident that increasing the length of the taper result in lower reflections and thus minimal variation in $Re\{Z_{in}\}$.

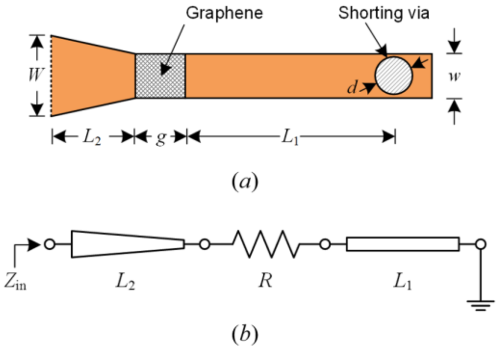

Figure 73: Detail of the microstrip stub integrated with the graphene pad: *(a)* Geometry of the stub (dimensions in mm: L1=12, L2=6, g=0.66, d=0.8, w=1, W=3.26); *(b)* Equivalent circuit.

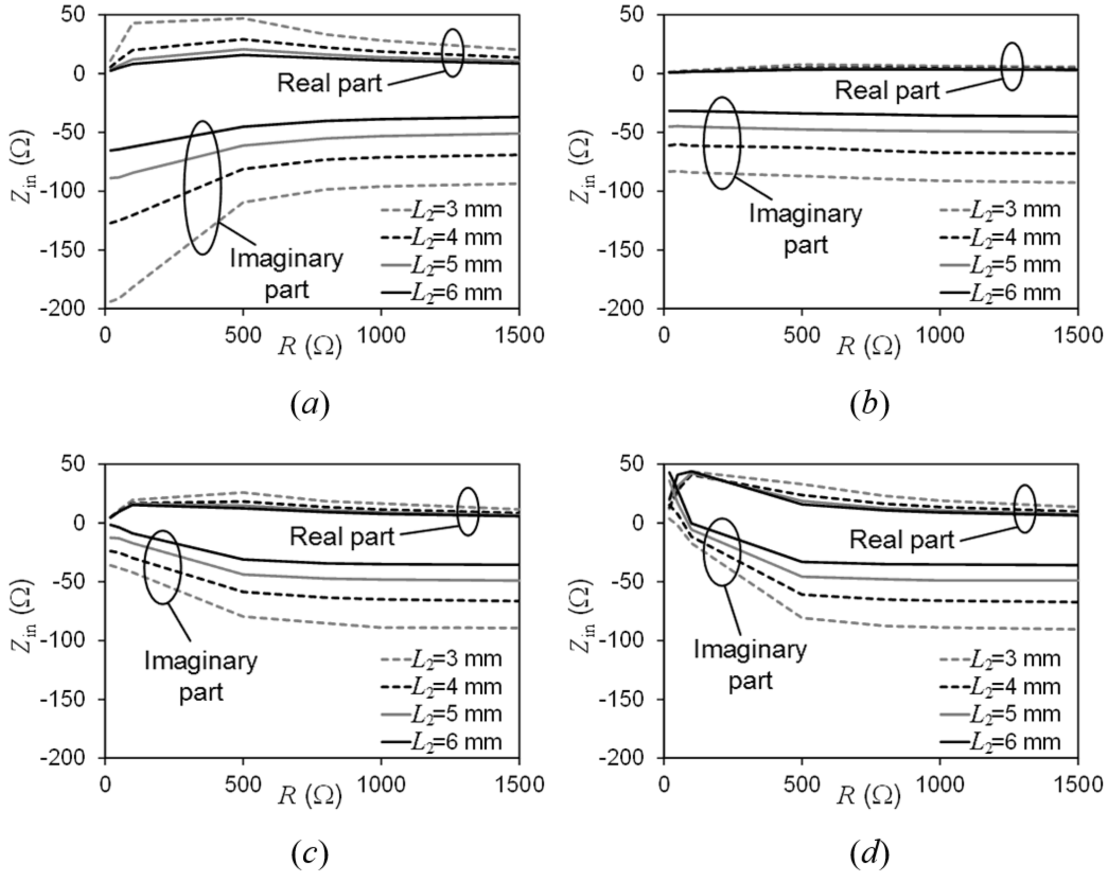

Figure 74: Real and imaginary part of Zin versus the graphene resistance for different values of the stub length L1 and the taper length L2, at the frequency of 5 GHz: (a) L1=6 mm; (b) L1=9 mm; (c) L1=12 mm; (d) L1=15 mm.

4.3 Simulation Results of the Phase Shifter

The optimized dimensions of the stub are used in simulating the entire phase shifter by the help of HFSS. The transmission phase and amplitude are plotted in the desired frequency band with assigned graphene sheet resistance equivalent to the measured DC resistance of graphene. The maximum acquired phase shift in the frequency range of 5 GHz to 6 GHz is 40 deg with a maximum additional transmission loss of 4dB as shown in the *Figure 75(a) and Figure 75(b)*.

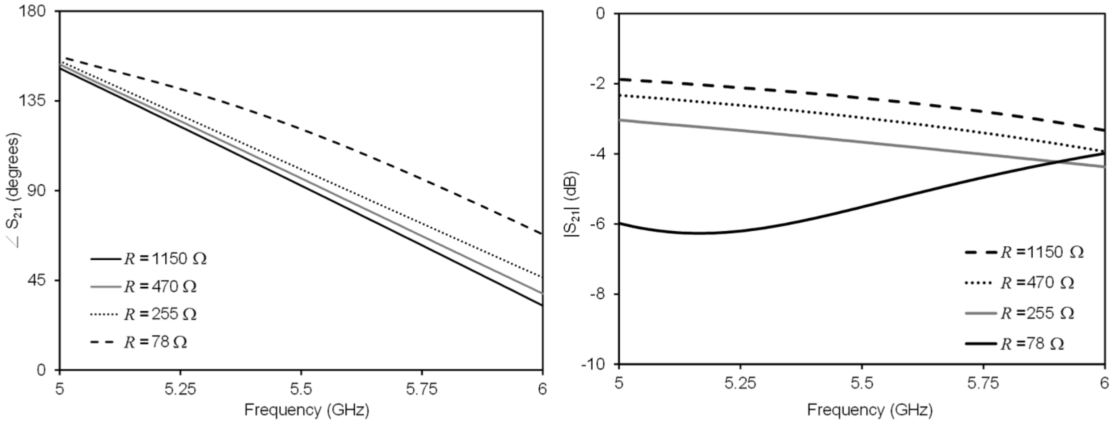

(a) *(b)*

Figure 75: Simulated scattering parameters of the phase shifter: (a) Simulated phase of S21; (b) Simulated amplitude of S21

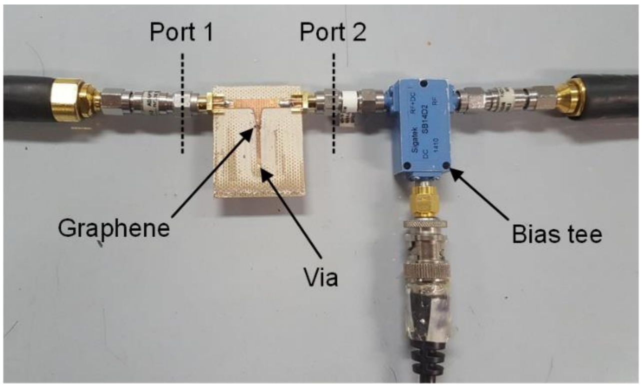

Figure 76: Measurement setup of the tunable phase shifter, with position of the reference ports.

4.4 Prototype and Measured Results

A prototype of the simulated structure is fabricated by the help of an LPKF micro milling machine. The via connecting the stub and ground plane is realized by filling it with conductive paste. FLG is deposited in the designated slot. The FLG is acquired by the process described in detail in the section 3.1 and [68], [75].

The measurement setup is as shown in *Figure 76*. The tunable FLG phase shifter is connected to the ports of a VNA. Biasing is performed by the help of a commercial broadband biastee. The bias voltage is applied between the port and ground plane since the stub is connected to the ground plane at one end. At each value of applied DC bias, both the DC current drawn by the FLG and the transmission between the ports is measured. The resistance of the FLG is calculated from the applied DC voltage and the current drawn by (Rg=Vbias/Idc). For each value of the applied DC bias, the values of DC current drawn and FLG resistance is shown in the Table I. As expected the resistance of FLG is decreased by increasing the applied DC bias voltage. The value of FLG resistance reported at 0 V DC bias voltage is measured by an ohm meter without any biasing. At 0 V applied DC bias voltage, the resistance of FLG is 1150 Ω, which is lowered to 78 Ω when the applied voltage is increased to 5 V.

Simultaneous measurements of the transmission scattering, S21 are carried out at each value of applied DC bias in the frequency band of 5 GHz to 6 GHz by a VNA. The VNA is pre-calibrated at the ports indicated in *Figure 76*. The placement of the ports is so as to remove any effects of the biastee. The measured transmission scattering, S21 versus frequency is as shown in the *Figure 77.* Both, the amplitude and phase are indicated. The phase and amplitude show a stable variation for the entire frequency band. In order to compare measured and simulated results, the simulated results of the *Figure 75(a) and Figure 75(b)* are at corresponding applied DC bias voltages as in the measured results of *Figure 77(a) and Figure 77(b).* These can also be compared by the help of Table I.

TABLE I – GRAPHENE RESISTANCE VERSUS VOLTAGE

V_{bias} (V)	I_{dc} (A)	R (Ω)
0	===	1150*
3.5	0.0074	473
4	0.0157	255
5	0.064	78

* Measured by using an ohm meter.

The maximum differential phase shift varies between 43 deg and 35 deg. The variation of insertion loss is from 2dB to 3dB. The maximum insertion loss variation occurs at 5V.

The proposed phase shifter is compared to similar phase shifters [71-74] [71][72][73][74]in the Table II. The FLG phase shifter provides comparable values in terms of phase shift, insertion loss and frequency bandwidth. The figure of merit is also indicated which is the ratio of the phase shift in deg to the insertion loss in dB.

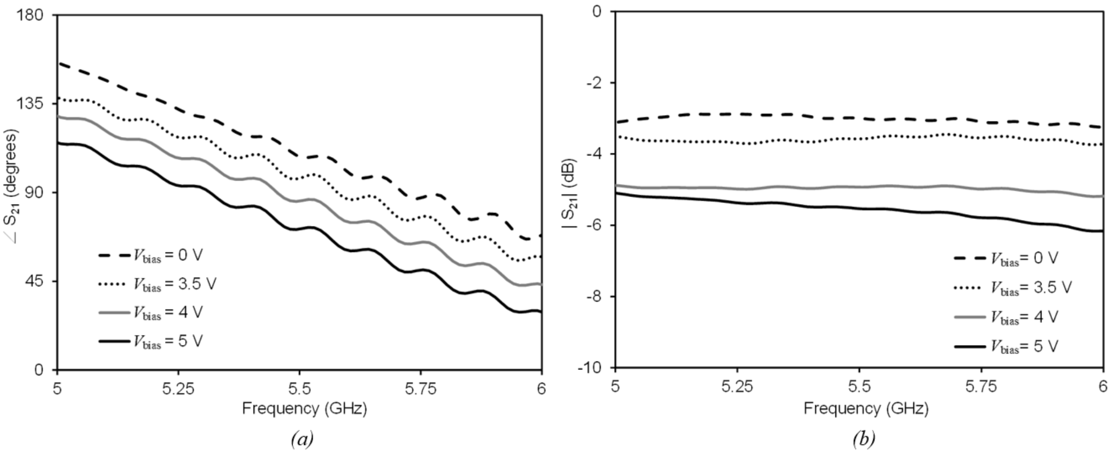

Figure 77: Measured scattering parameters of the phase shifter: *(a)* Measured phase of S21; *(b)* Measured amplitude of S21

TABLE II – COMPARISON OF NANOMATERIAL-BASED PHASE SHIFTERS

	Graphene Schottkey [74]	HfO_2 [73]	BST Thick-Film [71]	BST Thin-Film [72]	FLG Phase Shifter
Insertion Loss (dB)	5-10	14-6	1.2	3.3	3
Frequency band (GHz)	40-65	1-10	2-3	10	5-6
Phase (deg)	20	30	70	97	35-43
FOM (deg/dB)	6.5	1.67	58.2	29	14.3
Maximum Applied Voltage (V)	5	3	100	400	5

Conventionally, ferroelectrics are used to exploit their variable capacitive properties for phase shifters as in [71]. The voltage requirements of ferroelectrics are very high and they also operate at a very narrow frequency band therefore FLG phase shifter is a good alternative. As an example, the phase shifter of [76] provides only 20 deg of differential phase at 5 V. Another very useful characteristic of FLG phase shifter is that they can be deployed at a smaller scale keeping a constant aspect ratio unlike conventional phase shifter that are bulky.

4.5 Conclusions

In this chapter an electronically tunable FLG-based phase shifter is discussed by the help of simulated and measured results. The structure of the phase shifter is composed of a two-port transmission line connected to a shorted stub via FLG and a tapered line. The stub lengths are optimized for maximum phase shift and minimum insertion loss variation. The phase shifter provides more than 40 deg of phase shift with an added insertion loss of less than 3 dB in the frequency band of 5 GHz to 6 GHz

Even though the results obtained in this chapter are modest yet the fact that the insertion loss variation for this phase shifter is minimum therefore a cascade of a number of such structures can be put together in order to obtain higher values of phase shift. The design of the stub opens paves way for other tunable passive components based on graphene. An example of which is the FLG based tunable planar antenna which will be discussed in the following chapter. Another important impact of a combination of the attenuator presented in the Chapter 3 and the Phase shifter presented here can be used as a combination in order to design tunable graphene modulator which will also be discussed in the last chapter.

Chapter 5

Reconfigurable Graphene Antenna

Antenna tuning and reconfiguration is the requirement of a number of wireless communication systems since the maximization of connectivity is sought after due to the integration of a number of radiating elements into one platform [77]. There are several reconfiguration property requirements of a modern-day communication systems but the three main reconfiguration properties are the frequency of radiation, the radiation pattern and the polarization. Depending on the requirements of the system a combination of one or more of these properties can be required. It is however important that after the reconfiguration a number of the antenna basic characteristics including gain and impedance matching.

One of the most important form of an antenna reconfiguration is the reconfiguration of its radiating frequency. The antenna proposed in this chapter deals with such kind of reconfiguration. A number of methods can be adopted for achieving the reconfiguration of an antenna radiating frequency. The several techniques adopted can be classified into four main categories: Electrical reconfiguration, optical reconfiguration, Mechanical reconfiguration and material change reconfiguration. Electrical reconfiguration deals with the change of an electrical parameter (e.g. DC voltage) applied to an antenna in order to achieve reconfiguration while mechanical deals with the change of a mechanical parameter related to the antenna (e.g a mechanical switch). Optical reconfiguration deals with the operation of an optically operated switch and material change reconfiguration is the switching or modification of a material attached to an antenna [78], [79].

Conventionally, Electrical reconfiguration is obtained by the switching operation of PIN diodes by an applied DC voltage. This in turn changes the antenna currents and thus results in the change of the radiating frequency of an antenna. The graphene antenna proposed here and as published by the author in [14] is based on a similar principle. A DC bias is applied to the graphene antenna and a reconfiguration of the radiating frequency is achieved. The variation of graphene resistance can be exploited in the design of frequency tunable antennas [13], [80]. In such antennas, the frequency where the antenna exhibits the best input matching and the maximum gain can be modified electronically, by changing the voltage applied to the FLG. It is desired for tunable antennas to have large frequency tunability and limited gain degradation.

The tunable graphene antenna is composed of an inset fed patch antenna connected to FLG which are in turn connected to a shorted stub. The design of the antenna is as shown in *Figure 78*. The radiating frequency of the tunable graphene antenna can be modified by changing the FLG impedance through and applied DC bias voltage. The current flowing in the stub is altered as a result which modifies the resonating frequency of the antenna. A similar design of a tunable patch antenna, based on carbon nanotubes, was proposed in [78], [79].

5.1 Design of the tunable graphene antenna

The proposed antenna of the *Figure 78* can be modelled as a planar antenna connected to a variable impedance on its radiating edge. The variation in the impedance is caused by the applied bias voltage across the FLG. The shorted stub can be divided into three segments: the short segment of line next to the antenna, the FLG and the shorted stub connected to the grounded via. The relation between the impedance variation of the shorted stub (comprising a short segment of stub, FLG and shorted stub) and the resistance of the FLG is derived in the analysis that follows.

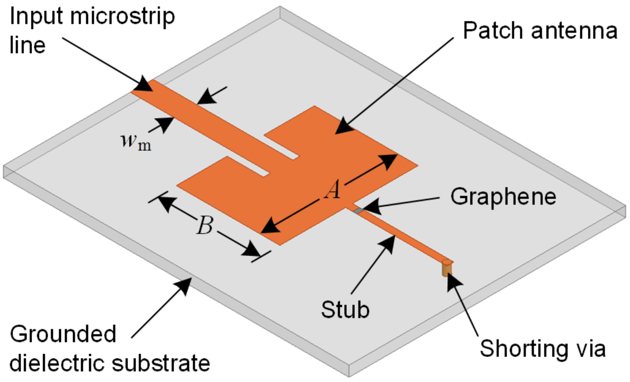

Figure 78: Geometry of Graphene tunable planar antenna *[14]*.

5.1.1 Stub Optimization

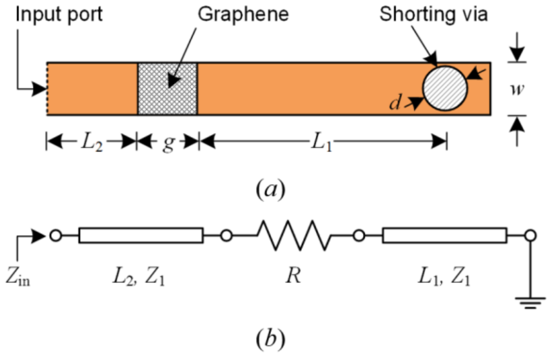

Figure 79: Microstrip shorted stub with the graphene pad: (a) Geometry of the stub; (b) Equivalent transmission line model *[14]*.

The different variables involved in the design of the stub setup are: the length, L_2 of the segment of line next to the radiating edge of the patch, the impedance of the line represented by Z_1 and the length of the segment of the line after the FLG connected to the grounded via represented by L_1. A detailed depiction of this setup is as shown in *Figure 79*(a). The impedance of the both the line segments is kept the same for sake of simplicity. FLG are deposited in the interconnection between the two line segments and has dimensions *gxw*.

The equivalent transmission line representation of the stub is as shown in *Figure 79(b)*. A section of transmission line connected to ground at one end of length, L1 is connected to a resistance (representing graphene) at the other end. Graphene can be modelled as a lumped resistor with resistance R=ρ g/w, ,ρ being the graphene resistivity which is tunable by an applied DC bias voltage as shown in section 3.2 and in [15]. Graphene resistance is connected to another piece of transmission line that has length L2 and is connected to the input port bearing impedance Zin. Both transmission line segments bear the same characteristic impedance, Z1. The input impedance of the complete stub, Zin is given by

$$Z_{\text{in}} = Z_1 \frac{R + jZ_1 \tan\beta L_1 + jZ_1 \tan\beta L_2}{Z_1 + j(R + jZ_1 \tan\beta L_1)\tan\beta L_2} \quad (7)$$

where β represents the propagation constant of the transmission lines at the operating frequency.

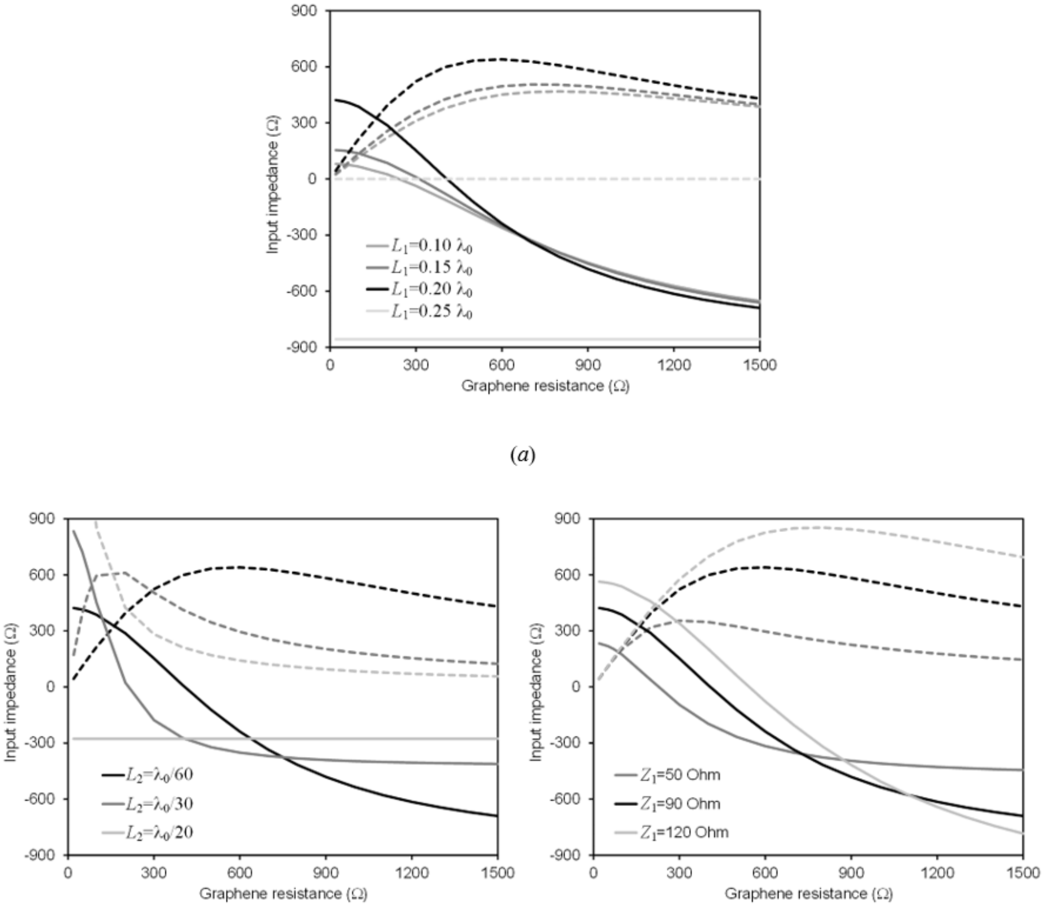

(a)

(b)

(c)

Figure 80: Variation of input impedance of the stub versus the resistance of the graphene pad at 5 GHz (solid line correspond to the real part of the input impedance Zin, and dashed lines denote the imaginary part): (a) For different values of L1 (with $L_2=\lambda_0/60$, , $Z_1=90\ \Omega$); (b) For different values of L_2 (with $L_1=0.2\lambda_0$, $Z_1=90\ \Omega$); (c) For different values of Z_1 (with $L_1=0.2\lambda_0$, $L_2=\lambda_0/60$) *[14]*.

The three different variables to optimize are L1, L2 and Z1. In order to have maximum tunability and minimum gain degradation it is necessary to have a maximum variation of the reactive part of Zin while keeping the real part as stable as possible as the graphene resistance, R is varied. The variables are thus changed one at a time and the impact of Zin is observed in *Figure 80*. The analysis is performed at the radiating frequency of the antenna which in this case is 5GHz. The impact of each of the variables is discussed in the following.

The impact of the change in L1, keeping $L_2=\lambda_0/60$ (where λ_0 is the wavelength at the operation frequency of 5GHz) and $Z_1=90\ \Omega$ is as shown in the *Figure 80*(a). The values of L1 are varied from 0.1 λ_0 to 0.25 λ_0. At L1=0.25 λ_0, which is quarter wavelength, the change in graphene resistance does not have any impact on Zin and is constant for all values. as no current flows across the graphene resistor. Reducing L1 slightly(L1=0.2λ_0) results in a drastic change in the imaginary part of Zin (represented by solid lines) and the real part of Z_{in} (represented by dashed lines) is varied slightly for the range of graphene resistance values. Further reducing the value of L_1 to $0.15\lambda_0$ and $0.1\lambda_0$ result in a reduced variation in the imaginary part Zin. The optimum value chosen for L_1 is thus $L_1=0.2\ \lambda_0$.

A similar approach is adopted for finding out optimum value so L_2. For this analysis L_1 is kept $0.2\ \lambda_0$ and Z_1 is kept at 90Ω. Real and imaginary part of Zin is plotted versus graphene resistance for three different lengths of $\lambda_0/60$, $\lambda_0/30$ and $\lambda_0/20$ as shown in *Figure 80*(b). The variation of real and imaginary parts of Zin for the range of graphene resistance show a maximum variation in the imaginary part of Zin for the case of $L_2=\lambda_0/60$ with minimum impact on its real part. As a result, the optimum case for this length is $L_2=\lambda_0/60$.

The third variable in this optimization is that of the characteristic impedance of the line, Z_1. The impact of the line impedance, Z_1 on the input impedance, Z_{in} is as shown in the *Figure 80*(c). For this case the values of lengths of the line segments are fixed at $L_1=0.2\ \lambda_0$ and $L_2=\lambda_0/60$. The analysis has been carried out for three values of Z_1: 50Ω, 90Ω and 120Ω. Low values of the line impedance result in a larger shift in the imaginary part of Zin but since the minimum realizable case is that of 90Ω therefore it is considered as the optimum case.

To sum up, the optimum values as a result of the analysis are: $L_1=0.2\ \lambda_0$, $L_2=\lambda_0/60$ and $Z_1=90\Omega$.

5.1.2 Patch Antenna Design

The optimized dimensions of the stub are used in the complete setup of the tunable antenna comprising an inset fed patch antenna and the optimized stub of the previous section. The complete setup is simulated by the help of Ansys HFSS. For simulations, the FLG is modelled as a resistive sheet with assigned value of resistivity, ρ ($\Omega/\square$). The substrate is a Taconic RF-35 dielectric substrate with permittivity $\varepsilon r=3.5$, loss tangent $\tan\ \delta=0.0018$. The thickness of the substrate is h=1.52 mm, and metal thickness is t=35 μm.

The dimensions of the patch antenna are designed so as to resonate at the frequency of 5 GHz. As a result, the patch has length B=15 mm and width A=20 mm as shown in *Figure 78*. The antenna is inset fed with a 50-Ω microstrip line of width wm=3.26 mm. The inset has a length of 5.25 mm and width 1.00 mm. The stub has the optimized dimensions of width, w=1 mm (90 Ω). The lengths of the line segments are $L_1=12$ mm and $L_2=1$ mm corresponding to $0.2\ \lambda_0$ and $\lambda_0/60$ respectively at 5GHz. The line segment L_1 is shorted at one end with a grounded via that has diameter, d=1 mm. The FLG connecting the line segments has length, g=0.66 mm and width, w=1 mm.

Simulation of the tunable antenna result in the return loss (|S11|) versus frequency for various values of graphene resistance as shown in the *Figure 81*. The radiating frequency of the antenna is shifted by varying the input impedance of the stub through a change in the FLG resistance. The presence of the stub is most felt when the FLG resistance is low, thus shifting the radiating frequency of the antenna lower than its design value.

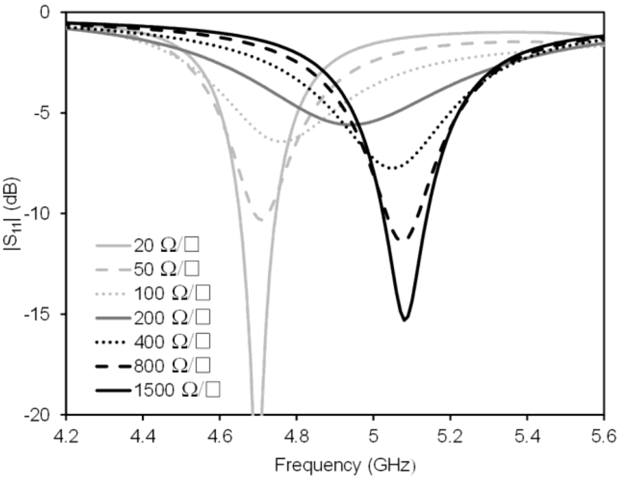

Figure 81: Scattering parameter |S11| of the antenna versus frequency, for different values of graphene resistivity ρ *[14]*.

When the FLG resistance is high the antenna resonates at its design frequency and it is as if the stub is not there. At FLG resistivity, ρ=1500 Ω/□, the antenna resonates at 5.08 GHz while at a lower FLG resistivity of ρ=20 Ω/□, the antenna resonates at 4.7 GHz, resulting in a total shift of 380 MHz as shown in *Figure 81*.

5.2 Measured Results

A prototype of the simulated antenna was fabricated as shown in the *Figure 82*(a). The prototype was fabricated by the help of an LPKF micro milling machine. Subsequently, the FLG were deposited in the designated gap on the prototype according to the technique described in section 3.1. The DC bias voltage was applied between the antenna feed line and the ground plane since the stub end is grounded and thus the DC voltage reaches the FLG. The DC bias voltage was supplied by the help of commercial bias tees that guaranteed broadband performance in the frequency band. The biastees were connected at one end to the port of a vector network analyzer and simultaneous measurements of the antenna return loss were carried out.

Measured results of the return loss, |S11| versus the frequency for different applied DC bias voltages are as shown in *Figure 82*(b). Without any applied bias voltage, the FLG bear high resistance and the antenna resonates at 5.05 GHz. As the DC bias is increased the radiating frequency is lowered and reaches 4.50 GHz at 5 V. The total shift in the resonant frequency is 550 MHz for an applied bias voltage of 5 V. This shift in frequency is larger than the 380 MHz of the simulated structure.

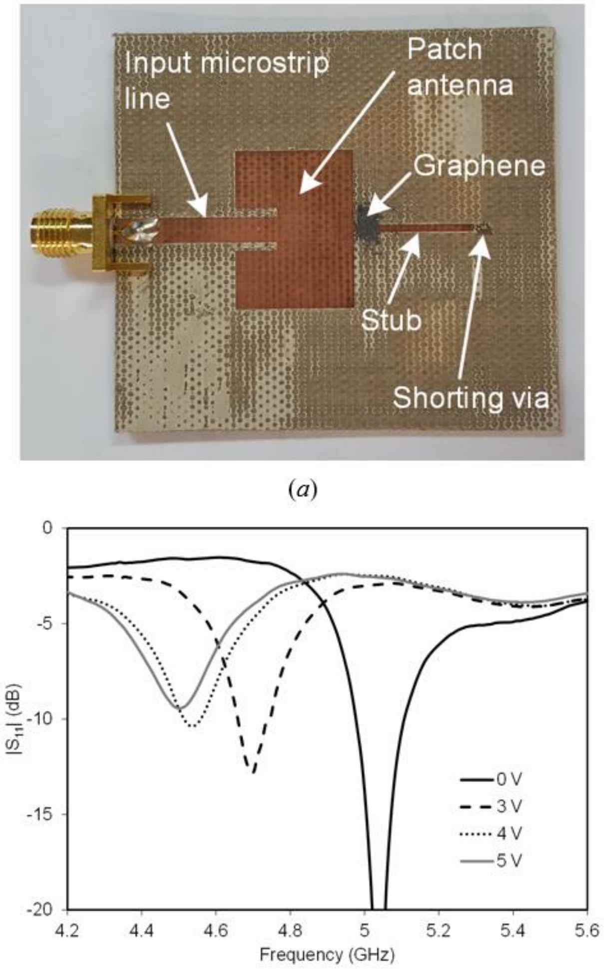

(*a*)

(*b*)

Figure 82: Experimental verification of the tunable patch antenna: *(a)* Prototype of the antenna; *(b)* Scattering parameter |S11| of the antenna versus frequency, for different values of bias voltage *[14]*.

The more-than-expected shift in the radiating frequency of the antenna can be as a result of the larger dimensions of the FLG depositions in the fabricated prototype than in the simulated structure. In order to investigate this hypothesis, the structure was simulated post measurements assigning larger dimensions (as compared to the initial dimensions of *Figure 78*) to the FLG depositions as shown in *Figure 83(a).* In this analysis two different dimensions are considered, one with a 100% increase and another one with a 200% increase. As shown in the *Figure 83(b,* in the 100% increased dimensions' case the frequency shift is slightly increased as compared to the initial simulations while in the 200% increased dimensions' case the frequency shift is almost 550 MHz, which is similar to that of the measured structure. The actual dimensions of the FLG in the prototype are similar to the 200% increased FLG dimensions case.

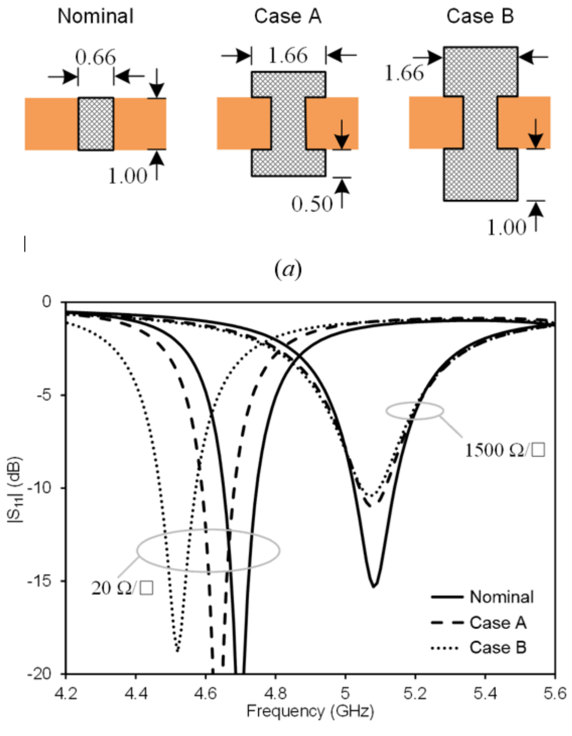

Figure 83: Post-fabrication simulation: (a) Geometry of the considered cases; (b) Frequency response of the antenna for different graphene pad size *[14]*.

As a result, it is deduced that the extra-shift of the resonant frequency comes with the reduced FLG resistance due to a larger amount of depositions than the initial simulated structure.

The gain of an antenna is an important figure of merit and thus the gain of the tunable antenna was measured in order to evaluate the impact of tuning of the gain degradation. A standard gain antenna was connected at one end of the VNA while at the other end the FLG tunable antenna was connected and the transmission was measured for all the applied bias voltages (FLG resistivity). The unknown in this case was the gain of the tunable FLG antenna since the gain of the standard gain antenna was known. For all the applied bias voltages, the gain of the tunable FLG antenna was calculated using the Friis equation. The simulated and measured values of gain is as reported in the Tab I for the applied bias voltages. As expected, the measured gain is slightly less than the simulated gain. The gain degradation for the different applied bias voltages is less than 2dB.

TABLE III
SIMULATION AND MEASUREMENT OF THE ANTENNA GAIN [14]

Simulation			Measurement		
Resistivity (Ω/☐)	Frequency (GHz)	Gain (dB)	Voltage (V)	Frequency (GHz)	Gain (dB)
1500	5.08	2.2	0	5.05	2.38
300	4.88	0.95	3	4.69	1.97
20	4.52	0.7	5	4.50	0.76

5.3 Conclusions

To conclude, a tunable antenna based on few layer graphene is presented in this chapter. The tunable antenna comprises of an inset fed planar antenna, two segments of transmission lines and FLG. One of the segments of the transmission line is shorted at one end and is connected to the other segment via the FLG, a setup referred to as the stub. The lengths and widths of the two sections of transmission lines are optimized so as to provide maximum variation in the imaginary part of the input impedance of the stub with a variation of FLG resistance. A variation in the reactance at the radiating edge of the patch antenna tends to shift the radiating frequency from its design frequency. This phenomenon is exploited in order to design tunable patch antenna. The resistance of the FLG is varied by an applied bias voltage resulting in a variable reactance at the radiating edge of the patch antenna providing electronic tuning of the antenna.

Without any applied DC bias, the antenna radiates at a frequency of 5.07 GHz. As the applied bias voltage is increased the radiating frequency is lowered and reaches a minimum value of 4.5 GHz for a DC bias of 5 V. The gain is reduced from 2.5 dB at 5.07 GHz with 0V applied to the FLG to 0.7 dB at 4.5 GHz with 5V applied to the FLG.

Chapter 6

Conclusions and Future Perspectives

This doctoral thesis is about the use of graphene for microwave tunable passive components. It opens a new paradigm in the use of innovative and cost-effective methods for producing tunable microwave components based on graphene. Specifically, it paves the way for future key components of microwave and wireless communication systems such as attenuators, phase shifters and antennas. A review of the state-of-the-art microwave passive components based on graphene in terahertz and microwaves is also provided.

The integration of a number of components on a transmitter receiver system requires functional materials of nanometric scale. The use of innovative nanomaterials for designing state of the art microwave components is not new. The signature property of monolayer graphene that can be exploited for tunable microwave components is its electronically tunable resistance. This property is valid for dimensions as large as mm/cm to as small as micro and nanometers keeping a constant aspect ratio. The big challenge in research on future communication systems is to cost effectively design, implement and measure such proposed components. To this aim, in this thesis few layer graphene is deployed in the design of tunable attenuators, phase shifter and antenna. The advantage of using FLG is its cost effectiveness, technological simplicity and eco friendliness unlike most nanomaterials.

A new design of tunable graphene attenuator was proposed based on shunt grounded vias with connected to FLG flakes and microstrip line. The grounded vias were symmetrically placed on each side of the microstrip line with two ports. The design, even though of not very high structural complexity resulted in superior functionality both in terms of dynamic range of insertion loss and the reflective insertion loss. The number of vias were then increased for improved functionality. With the increase in the number of vias, emerging structural parameters were optimized. It was noticed that increasing the number and optimizing the design provided better functionality. The total insertion loss improved but not only that, the reflective part of the total insertion loss was also reduced as a result. Subsequently, the number of the vias were further increased to a total of eight and optimization of structural parameters performed. Simulations were performed for the optimization while fabrication of prototype and measurements were performed which were in good agreement to the simulated results. For the final case of eight vias connected to FLG, a total of more than 65 dB insertion loss was measured with reflective insertion loss as low as 2dB.

Phase Shifter being a vital component of a communication system was also made incorporating FLG flakes. The tunable resistance value was converted to a tunable reactance value by the help of a stub composed of tapered line connected to FLG and a shorted line. The various lengths and widths of the line were optimized so as to provide maximum shift in reactance when the change in FLG resistance would occur by an applied DC bias voltage. Subsequently, the optimized stub with variable reactance was connected to a two-port 50 Ω transmission line, the transmission on which would cause a phase shift by an applied DC voltage across the FLG. The maximum phase shift obtained was 43 degree with insertion loss variation of 3 dB. The concept can be applied to a number of such units connected in cascade since the insertion loss is not very high. A combination of the phase shifter and attenuator can be used in the design of a tunable modulator based on a combination of amplitude and phase variation.

The concept of the phase shifter was applied to a tunable patch antenna. Conventionally, tunable antennas are design with PIN diode which work on the principle of change in capacitance with an applied voltage bias which changes the antenna currents that can be exploited in the design of tunable antennas. In this thesis, FLG accompanied by a shorted stub optimized for maximum reactance change were deployed in a microstrip antenna. The change in the FLG resistance would cause a reactance change on the radiating edge of the patch antenna mimicking a PIN diode. The change in reactance would cause the antenna to radiate at a frequency lower than its frequency of radiation. A total shift of 450 MHz was measured at an applied DC bias voltage of 5V with limited gain degradation.

The future work suggested in this thesis is to combine the concepts of the attenuator and the phase shifter and design a QAM modulator based on both amplitude and phase change. For this purpose, a slight improvement in the phase shifter is required but that can be easily achieved by putting of a number of phase shifters proposed in this work in cascade. The proposed modulator would trace a number of points as bits on a grid, each representing a specific amplitude and phase change. Each of the point on the grid would be traceable by a specified applied DC bias voltage at specific points on the modulator. This is explained in detail in the Appendix A. Appendix B explains in detail the functionality of an energy harvester based on graphene Self switching diode.

Appendix A

Graphene Based Modulator Design

The concept of the tunable attenuator of the Chapter 3 and that of the Phase shifter of Chapter 4 can be combinedly applied to design a Quadrature amplitude modulator (QAM). The concept of QAM is that a single point on the grid of a QAM modulator describes a specific amplitude of the signal with a specified phase shift as shown in the *Figure 84*. It can be rightly described as a mixture of both amplitude and phase modulation.

Since the phase shift provided by the phase shifter of chapter 4 is only 43° therefore it is not possible to cover all the angles of the 16 QAM. However, the design can be improved by a cascade of based on a similar concept. Putting the amplitude modulator along with the cascade design of the phase sifter the complete modulator design is as shown in the *Figure 85*: Simulation results with only four different values of the graphene resistance shows very promising results. The total phase shift has been increased to more than 160° with the amplitude variation of more than 50 dB at the frequency of 4 GHz. The bandwidth of the design is not very wide but this is just a preliminary design and has the potential of further improvement. The simulation results of the amplitude variation of the graphene modulator with four different graphene resistance is as shown in the *Figure 86*:

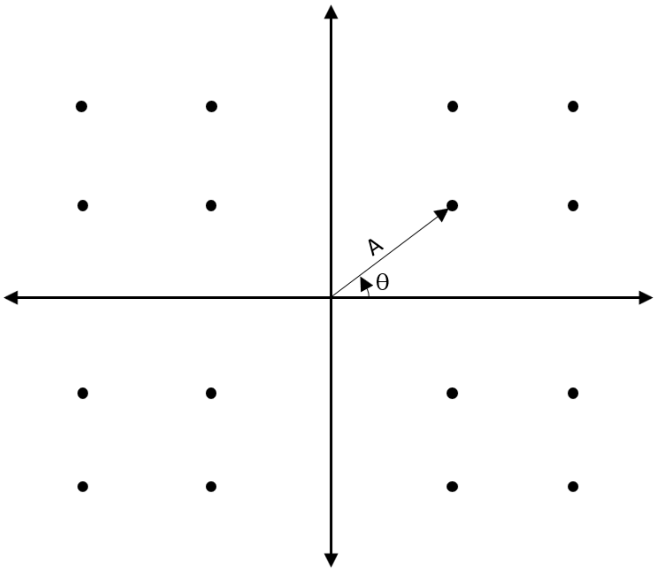

Figure 84: 16 QAM design with amplitude A and Phase theta

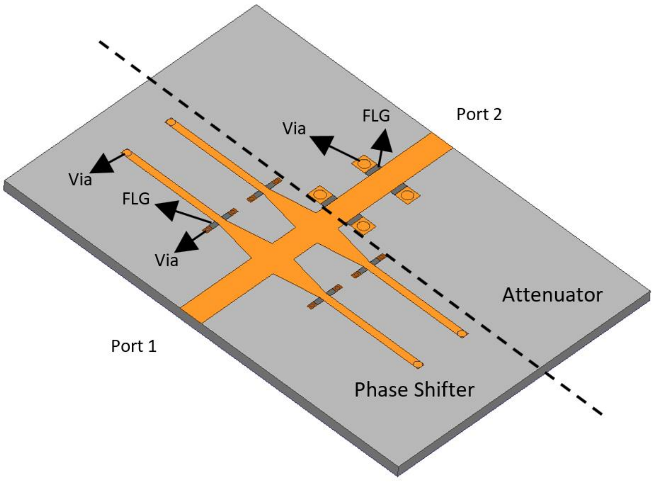

Figure 85: Graphene based modulator design: a combination of the attenuator and the phase shifter.

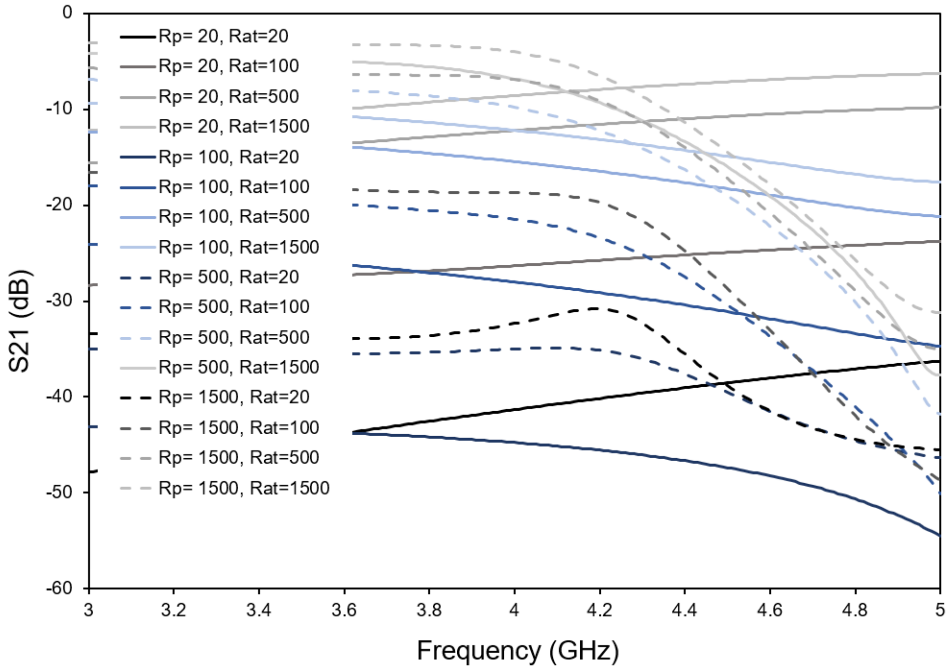

Figure 86: Simulation results of the attenuation with four values of assigned graphene resistance.

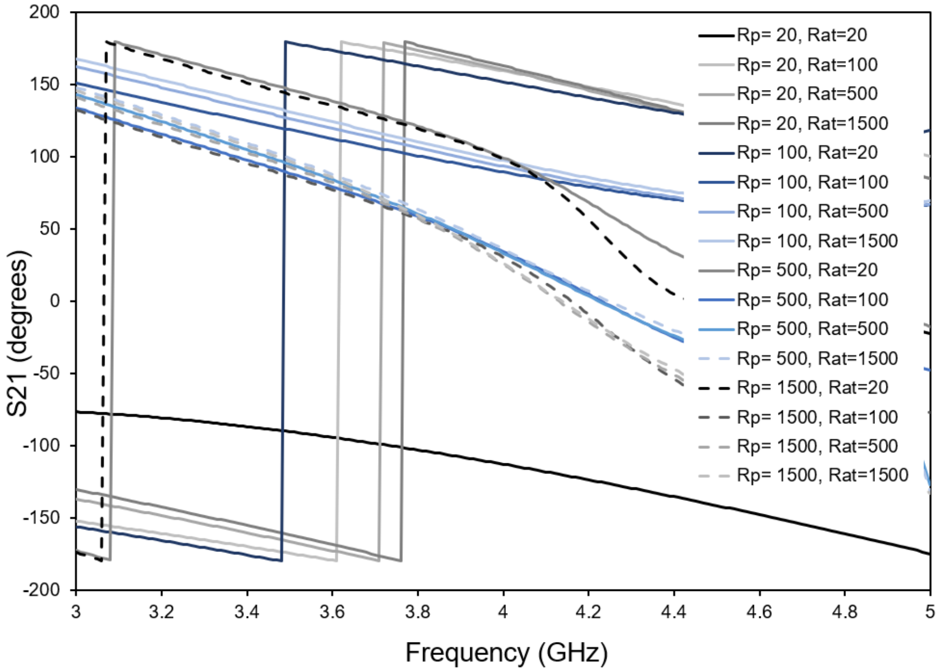

Figure 87: Simulation results of the phase shift provided by the graphene modulator with assigned graphene resistance.

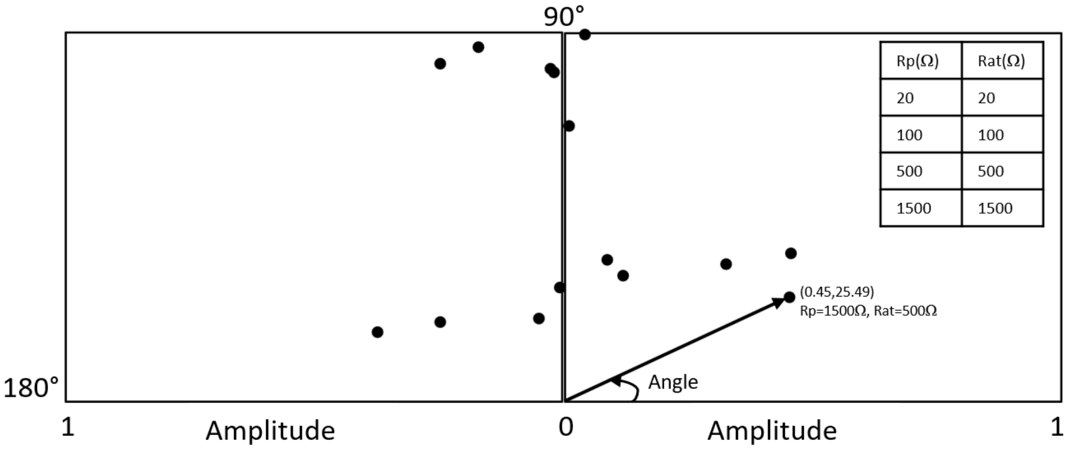

Rp(Ω)	Rat(Ω)
20	20
100	100
500	500
1500	1500

Figure 88: Graphene modulator grid with only four assigned graphene resistance values.

In the *Figure 86*, Rp is the resistance value assigned to the phase shifter side of the modulator while Rat is the assigned value of resistance to the attenuator side as dividedly shown in the *Figure 85*. The simulation results showing a change in the phase shift is as shown in the *Figure 87*. A combination of the amplitude and phase shift in the form of a grid is as shown in the *Figure 88*: The graphene resistance for both the phase shifter and the attenuator for one of the cases is also shown. It is to be noted here that for the sake of simplicity only 4 different values of graphene resistance for each of the attenuator and phase shifter part are considered. Practically, there is no limit on the graphene resistance as it changes with the applied bias voltage and a much higher number of points can be generated.

Appendix B

Graphene Energy Harvester

Detection of low-power signals is a very important issue in the field of radar applications in the microwave frequency range [81]. The upcoming 5G communications are the backbone of internet-of-things (IoT) working in the range 1–100 GHz. Specifically, some bands are of great importance, such as 2.5 GHz, 28 GHz or 60 GHz: the first one is the well-known ISM – industrial, scientific, medical – band; the 28 GHz band has been permitted for 5G use; finally, the available spectrum around 60 GHz allows high-rate, unlicensed wireless communications [82]. The self-powering of many objects ("things") is a must for the development of IoT, as it paves the way to future 5G IoT scenarios [83-85] . In this respect, electromagnetic (EM) detection in the super high frequency band (SHF, 3–30 GHz) is an active research area, as it is based upon different antenna geometries, all equipped with a diode able to rectify the EM signal ("rectennas" [86]). New materials are used for classic Schottky diodes included in rectennas (like diamond and graphene [87], [88]). Self-switching diodes (SSD) are planar semiconductor diodes, used especially for THz applications [89]. Their working principle is based on a nonlinear current flow (through nanometer-sized parallel channels) controlled by field-effect phenomena. The SSD is a geometrical diode: no junctions are necessary, hence no doping (which has detrimental effects in case of graphene monolayers). The geometrical design parameters of the SSD are crucial for the optimization of its performance. In detail, the width of the channel is given by lithographic constraints in the semiconductor process, whereas the channel length and the number of channels are the main objects of the design process that lend themselves to design and optimization. Up to now, SSD detectors have successfully been realized deploying various materials, such as graphene for microwave and millimeter waves [90], [91], reduced graphene oxide/ZnO, InP/InGaAs/InP, AlGaN/GaN and InAs [92-94] , and the most promising results have been obtained with GaAs SSDs (NEP of 330 pW/√Hz at 1.5 THz). Nevertheless, no attempt has been made to integrate an SSD with a radiating system, in order to demonstrate its effective capability of detecting microwave energy. The aim here is to fill this gap by presenting the fabrication and experimental characterization of a patch antenna array integrated with a graphene SSD (GSSD), for EM detection applications in the 28 GHz band.

B.1 Graphene Self Switching Diode: Modelling, Fabrication and Performance:

Since a SSD is a two-terminal geometrical diode, the fabrication is performed with minimal process steps. An SSD can be modelled very simply as a two-dimensional field-effect transistor (FET), with short-circuited gate and drain, made of N narrow channels in parallel [95]. Its nonlinear I-V behavior can be used for detection of radio frequency signals. First, the geometric layout of the GSSD able to guarantee the best trade-off between nonlinearity and current values of the I-V characteristic is investigated. The GSSD can be modelled as a capacitive divider with quantum capacitance C_q and substrate capacitance C_s in series. Each channel couples capacitively to the applied drain bias voltage (V_d) via C_q and C_s. The modeling is presented in [91] and we have $I_d \approx N\mu_{eff} C_s \frac{w}{\ell} |V_d - V_D| V_d$, where N is the number of channels, μ_{eff} is the effective channel mobility (of graphene), w is the distance between adjacent channels, ℓ is the length of the channel and V_D is the Dirac voltage (here, set equal to zero). After an optimization process to achieve the highest nonlinearity and the maximum value for I_d at low values of the DC bias voltage, N=12, w_0=w=100 nm and ℓ=1.1 μm (the width is given by lithographic constraints in the fabrication process) was obtained. This means that the whole GSSD is made of 12 channels in parallel, which entails that the currents flowing along the single channels sum up, thus increasing the total current of the device. The reference substrate is a 4-inch high-resistivity silicon/silicon dioxide (HRSi/SiO_2) wafer, with thickness of 525 μm/300 nm (respectively); the HRSi has a nominal resistivity of 10,000 Ω·cm. In order to properly measure the GSSDs in DC and in microwaves, a coplanar waveguide (CPW) structure was used with open stubs of different lengths (namely 300, 500, 700 and 900 μm), in order to provide different reactance values suitable to optimize the impedance matching to 50 Ω in correspondence of the port connected to the antenna array. This guarantees the maximum power transfer from the array (which harvests the electromagnetic – EM – energy) to the diode (which detects/rectifies the signal coming from the array). The CPW ports in ground-signal-ground (GSG) configuration have dimensions of 60-100-60 μm, optimized for standard 150-μm-pitch GSG probe tips. As regards the fabrication of the GSSDs, first the graphene monolayer was fixed in the diodes' location using two rectangular metal pads. The diodes were patterned by e-beam lithography using PMMA 950k as electron resist and O_2 plasma etching). To remove the graphene from the wafer surface, the diodes were covered by a negative electron resist – hydrogen silsesquioxane (HSQ) – that was also patterned by e-beam lithography, defining rectangular protective areas on top of the diodes and the residual graphene was etched away in oxygen plasma.

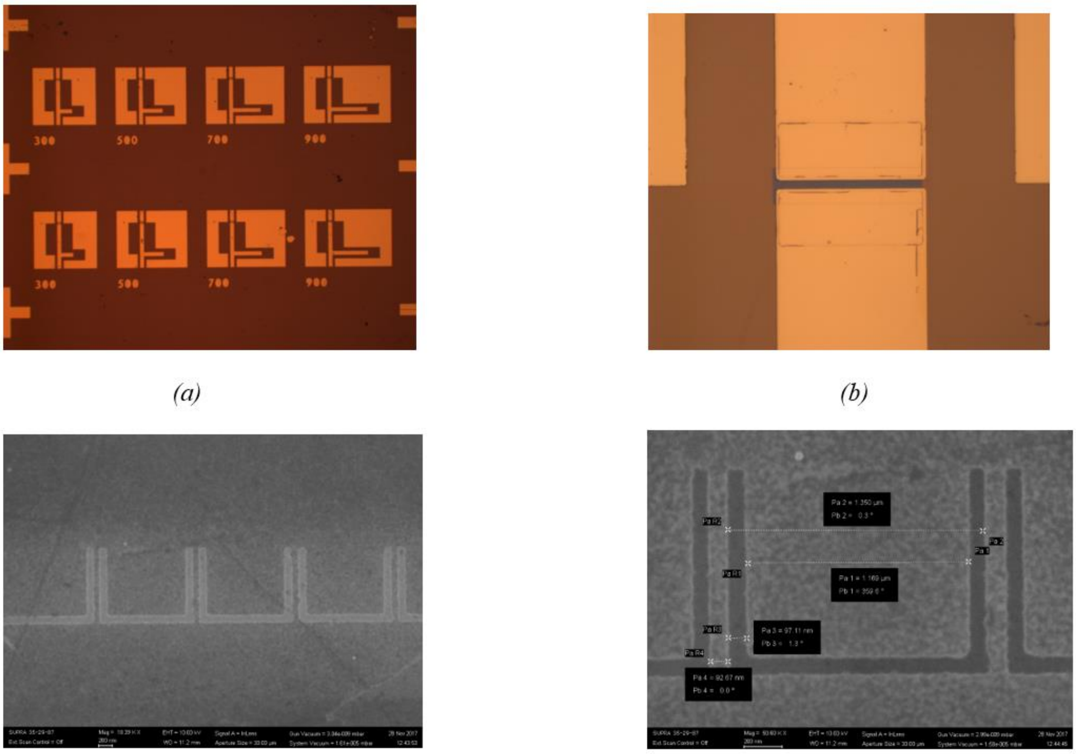

(a) (b) (c) (d)

Figure 89: Fabrication of the GSSDs with stubs in CPW technology: (a) optical picture of 8 devices with different stub's lengths; (b) magnification of diode's area with the HSQ thin film on the graphene monolayer; (c) SEM image of the GSSD with four channels in parallel; (d) magnification of two channels in parallel with main dimensions.

The fabricated devices are shown in *Figure 89*. In detail, *Figure 89(a)* is an optical picture of the CPW-based devices with stubs of different lengths (denoted by the numbers under each device), whereas *Figure 89(b)* is a magnification of the diode area (with the HSQ thin film on the graphene monolayer) and *Figure 89(c) (d)* are SEM images of the GSSD with (c) four channels and (d) a magnification (with main dimensions) of two channels.

Figure 90 shows the measured I-V characteristic of the fabricated GSSD. All measurements were carried out using a Keithley SCS 4200 station (enclosed in a Faraday cage) with all channels connected to low noise amplifiers. The maximum DC current value is about ±1.2 mA at ±3 V. The values of frequency-dependent equivalent resistance (R_{eq}) and capacitance (C_{eq}) of the diode (as calculated as an equivalent R-C parallel circuit were also extracted, as seen from the port directly connected to the GSSD): in this case, in the band of interest (i.e. 26–30 GHz) the average value of the resistance is around 264 Ω (which can be considered, with a good approximation, the combination of the total parasitic linear resistance $R_{s,tot}$ and of the intrinsic nonlinear resistance R_i that represents the electrical nonlinearity of the GSSD [96]), whereas the average value for the capacitance is around 68.36 fF.

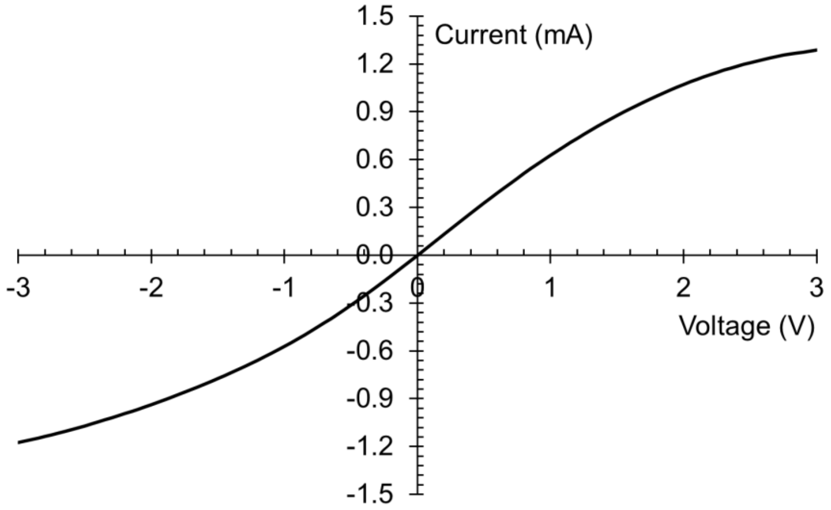

Figure 90: Measured I-V characteristic of the generic GSSD

It has to be stressed that all the measurements were carried out at room temperature (T=290 K).The differential resistance of the diode R_D (defined as $R_D=\partial V_d/\partial I_d$) spans the range 1.48–5 kΩ. The yield rate of the fabrication is very high (over 90% of the fabricated devices exhibit show the same I-V characteristic), and we observed that the GSSDs burn out between ±6 V and ±7 V of applied DC bias voltage: for this reason, the bias to the diodes were not exceeded over ±3 V, also due to a linearization of the I-V characteristic and a consequent saturation of its performance. Since graphene monolayer is a semimetal exhibiting ambipolar transport, from the measured I-V curve it results that the GSSD works for both positive and negative values of the DC bias. This was reported previously [90] and can be interpreted by considering two main interacting phenomena, i.e. the charge neutrality near zero bias ($V_d \approx V_D$) and the current saturation at high bias values. At zero bias, the measured voltage responsivity at 28 GHz (when the GSSD is fed from a 50 Ω impedance with an input power of 0.87 dBm or 1.22 mW) is $\beta_{50\Omega}$=7.04 V/W and the corresponding noise equivalent power ($NEP_{50\Omega}$) is $NEP_{50\Omega} = \sqrt{4K_BTR_{D0}}/\beta_{50\Omega}$ [96], where K_B is Boltzmann’s constant and R_{D0} is the zero-bias differential resistance. In the present case, we obtained $NEP_{50\Omega}$=691.56 pW/√Hz, which is of the same order of magnitude of the actual state-of-the-art for GSSDs [90]. Since the detection sensitivity for weak AM signals can be improved by biasing the diode (in order to move the operating point slightly closer to a higher nonlinearity – in either forward or reverse conduction), we measured the maximum value of DC bias voltage able to maximize $\beta_{50\Omega}$: it was found that the voltage responsivity at 28 GHz is the highest possible, with $\beta_{50\Omega}$=96.16 V/W for a bias of V_d=-1.35 V.

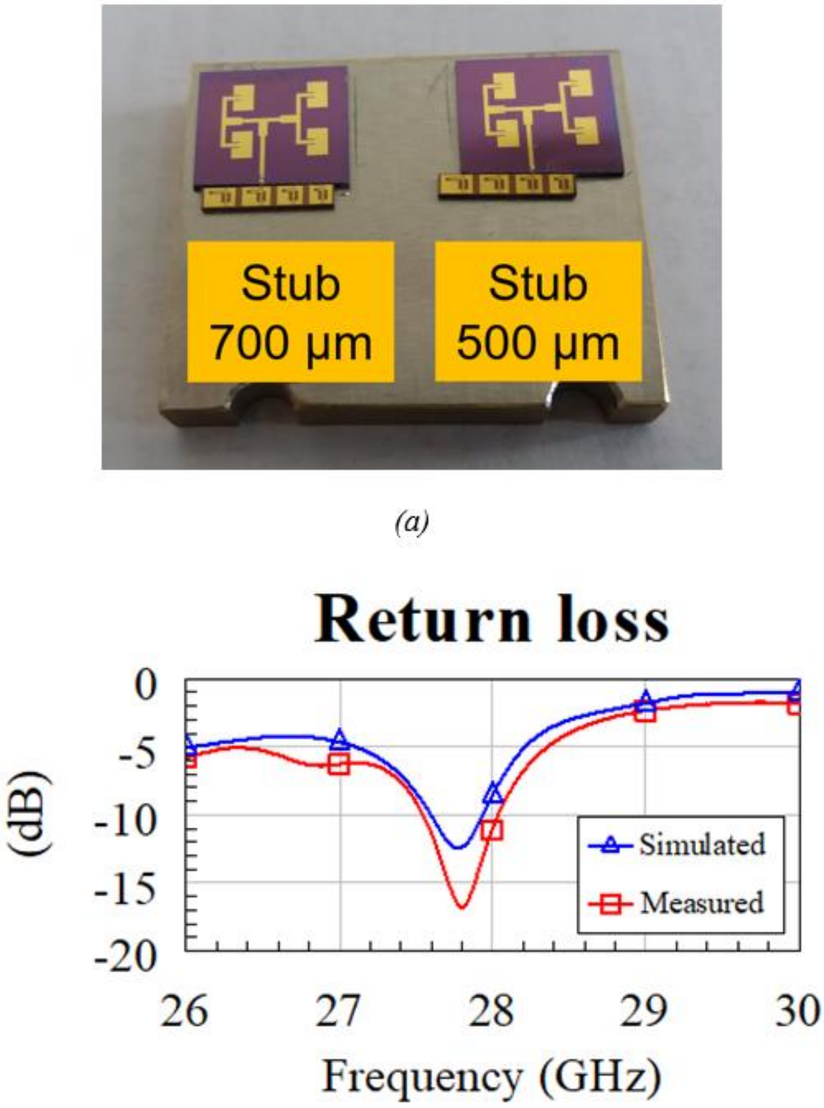

(a)

(b)

Figure 91: (a) Fabricated rectenna prototypes assembled on the same metal support, each one with a GSSD in CPW but with different stub's lengths; (b) simulated (solid blue line with triangles) and measured (solid red line with squares) return loss of the standalone patch antenna array.

B.2 Integration of Antenna Array with GSSD:

The radiating element is a 4-element patch antenna array *Figure 91* fabricated by means of optical lithography. The metallization is a 500 nm thick gold layer. The antenna metallization was deposited and patterned by means of a lift-off process. The array configuration is 2×2, the length and width of each patch antenna being L=1.5 mm (x-direction) and W=2.206 mm (y-direction), respectively, while the spacing between antennas is about $0.51\lambda_0$ in the x-direction and about $0.37\lambda_0$ in the y-direction, with $\lambda_0 \approx 10.71$ mm the free-space wavelength at 28 GHz. These dimensions provide the optimal broadside radiation and in-phase excitation of all the radiating elements. The reference array input impedance of 50 Ω is guaranteed by a microstrip line with a width of 300 µm. The array ensures a higher gain (i.e. about 8.1 dB from EM simulations) with respect to the single patch. Two arrays were placed on the same metal support, each array connected to a GSSD with different stub length, namely 500 µm and 700 µm, in order to verify the different effect of stub's length on power transfer from the array to the diode. It was found that the antenna-GSSD matching is enhanced with the 500-µm-long stub. The array-GSSD electrical connection is guaranteed by two 17 µm diameter gold wires (soldered in parallel) and by a silver conductive paste polymerized by heating at 120 °C for 1 hour. The simulated and measured return loss ($|S_{11}|$) of the standalone array are shown in *Figure 91(b)*. The resonance occur at 27.8 GHz with a very good agreement between simulations and measurements. The measured voltage standing wave ratio (VSWR) is about 1.34 and the -10 dB fractional bandwidth is about 1.76%.

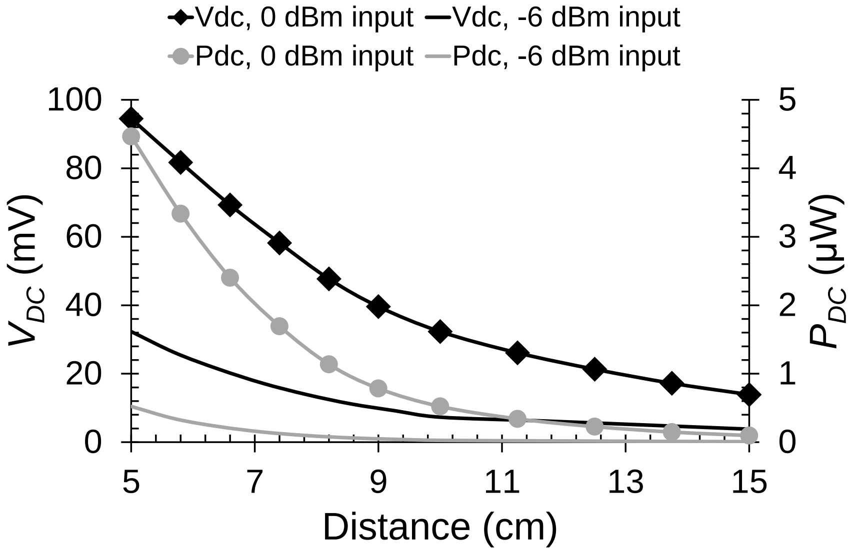

Figure 92: Measured DC voltage (in mV, left axis, black lines) and power (in µW, right axis, grey lines) as a function of the distance (in cm) between transmitter and proposed detector, for two values of the power input to transmitter.

The measurement setup for the RF characterization comprises an Agilent analog signal generator, connected to a horn antenna (“transmitter”, Ka band, gain of 24 dBi), excited by a 28 GHz sinusoidal carrier modulated by a square AM signal of frequency f_{AM}=1 kHz. The transmitter was put at various distances from the rectenna, connected to a Tektronix oscilloscope through a 2 kΩ resistor, representing the output load of the rectenna. This value of resistance was chosen as it is very close to the differential resistance of the GSSD, thus enhancing the output DC signal. No optimization was carried out for the capacitive part of rectenna’s load, useful to smooth out the output ripple and store the rectified energy. In order to verify the effect of a DC bias on the diode, an Agilent power Supply was also used. By moving the transmitter between 5 and 15 cm (both in the far field region) of distance from the rectenna, the effective RF input power to the GSSD is in the range (-3.26 dBm)–(-18.80 dBm). The calculated voltage responsivity $\beta_{50\Omega}$ for different values of the DC bias gives the proof that negative values provide a clear enhancement of the responsivity w.r.t. positive ones, due to diode’s asymmetry, with a maximum value of 96.16 V/W at 28 GHz for V_d=-1.35 V. Finally, in *Figure 92* the measured DC voltage V_{DC} (in mV) and power P_{DC} (in μW) is presented as a function of the distance (in cm) between transmitter and rectenna, for V_d=-0.66 V and for two values of the power input to the transmitter (i.e. 0 dBm and -6 dBm). The maximum values are V_{DC}=94.5 mV and P_{DC}=4.47 μW at 5 cm distance, whereas the minimum values are V_{DC}=3.8 mV and P_{DC}=7 nW at 15 cm distance. Beyond V_d=-0.66 V, the performance of the GSSD does not change due to saturation of the I-V characteristic. Moreover, higher values of RF input power seem to affect graphene’s atomic structure, causing a degradation of diode’s performance (and a decreasing of V_{DC}). Hence, the proposed rectenna represents a good candidate for very low power applications, e.g. for low-voltage processors consuming 35.4 pW in standby mode and 226 nW in active mode [97] or for low-current (tens of nA) sensors used in IoT devices [98].

List of Publications

2015/2016

C1 **M. Yasir**, P. Savi, M. Giorcelli, and A. Tagliaferro, "Comparative analysis of MWCNTs nanocomposites at Microwave frequency," *15th IEEE Mediterranean Microwave Symposium,* Lecce, Italy, December 2015.

C2 **M. Yasir**, S. Bistarelli, A. Cataldo, M. Bozzi, L. Perregrini, and S. Bellucci, "Innovative tunable microstrip attenuators based on few-layer graphene flakes," *16th IEEE Mediterranean Microwave Symposium,* Abu Dhabi, UAE, Nov. 2016. (**BEST STUDENT PAPER AWARD WINNER.**)

2016/2017

J1 P. Savi, **M. Yasir**, M. Giorcelli, and A. Tagliaferro, "The effect of carbon nanotubes concentration on complex permittivity of nanocomposites," *Progress in Electromagnetics research M*. Vol. 55 n. 1, pp. 203-209, ISSN 1937-8726, Jan. 2017

J2 **M. Yasir**, S. Bistarelli, A. Cataldo, M. Bozzi, L. Perregrini, and S. Bellucci, "Enhanced Tunable Microstrip Attenuator Based on Few Layer Graphene Flakes," *IEEE Microwave and Wireless Components Letters* Vol. 27(4), pp. 332-334, Apr. 2017

J3 **M. Yasir**, P. Savi, S. Bistarelli, A. Cataldo, M. Bozzi, L. Perregrini, and S. Bellucci, "A Planar Antenna with Voltage-Controlled Frequency Tuning Based on Few-Layer Graphene," *IEEE Antennas and Wireless Propagation Letters* Vol. 16(1), pp. 2380-2383, Jun. 2017

C3 **M. Yasir**, S. Bistarelli, A. Cataldo, M. Bozzi, L. Perregrini, and S. Bellucci, "Highly tunable and large bandwidth attenuator based on few-layer graphene," *2017 IEEE MTT-S International Microwave Workshop Series on Advanced Materials and Processes for RF and THz Applications (IMWS-AMP),* Pavia, Italy, Sep. 2017.

2017/2018

C4 **M. Yasir**, S. Bistarelli, A. Cataldo, M. Bozzi, L. Perregrini, and S. Bellucci, "Tunable and input-matched attenuator based on few-layer graphene," *2017 47th European Microwave Conference (EuMC),* Nuremberg, Germany, Oct. 2017.

C5 M. Aldrigo, **M. Yasir**, S. Iordanescu, D. Vasilache, A. Dinescu, M. Dragoman and M. Bozzi, "Graphene self-switching diodes for sub-millimetre wave harvesting applications," *2018 Workshop on Compound Semiconductor Devices and Integrated Circuits held in Europe (WOCSDICE)*, Bucharest, Romania, May. 2018.

J4 **M. Yasir**, S. Bistarelli, A. Cataldo, M. Bozzi, L. Perregrini, S. Bellucci, "Tunable Phase Shifter Based on Few-Layer Graphene Flakes," *IEEE Microwave and wireless component letters*, Vol. 29, No. 1, pp. 47-49, Jan. 2019

J5 **M. Yasir**, M. Aldrigo, M. Dragoman, A. Dinescu, M. Bozzi, S. Iordanescu, D. Vasilache, "Integration of antenna array and self-switching graphene diode for detection at 28 GHz," *IEEE Electron Device letters*, 2018 **(In review)**

References

[1] M. Sharon and S. Maheshwar , Graphene An Introduction to the fundalmentals and Industrial Applications, Massachusetts: Scrivener Publishing, 2015.

[2] K. S. Novoselov, A. K. Geim, S. V. Morozov, D. Jiang, Y. Zhang, S. V. Dubonos, I. V. Grigorieva and A. A. Firsov, "Electric Field Effect in Atomically thin Carbons," *Science,* vol. 306, no. 5696, pp. 666-669, 2004.

[3] J. H. Chen , C. Jang, S. Xiao, M. Ishigami and M. S. Fuhrer MS, "Intrinsic and extrinsic performance limits of graphene devices on SiO2," *Nature Nanotechnology,* vol. 3(4), pp. 206-209, 2008.

[4] E. Y. Andrei, G. Li and X. Du, "Electronic properties of graphene: a perspective from scanning tunneling microscopy and magnetotransport.," *Reports on progress in Physics; physical scoiety Great Britain,* vol. 75(5), p. 056501, 2012.

[5] A. K. Geim and K. S. Novoselov, "The rise of graphene," *Nat. Mater.,* vol. 6, p. 183–191, 2007.

[6] H. Mehdi , S. Arezoomandan, H. Condori and B. S. Rodriguez, "Graphene terahertz devices for communications applications," *Nano Communication Networks,* vol. 10, p. 68–78, 2016.

[7] M. Wang and E.-H. Yang, "THz applications of 2D materials: Graphene and beyond," *Nano-Structures & Nano-Objects,* vol. 15, p. 107–113, 2018.

[8] B. Sensale-Rodriguez, R. Yan, M. M. Kelly, T. Fang, K. Tahy, W. S. Hwang, D. Jena, L. Liu and H. G. Xing, "Broadband graphene terahertz modulators enabled by intraband transitions.," *Nature Communications,* vol. 17, no. 3, p. 780, 2012.

[9] P. Weis, J. L. Garcia-Pomar, M. Höh, B. Reinhard, A. Brodyanski and R. Marco, "Spectrally Wide-Band Terahertz Wave Modulator Based on Optically Tuned Graphene," *ACS Nano,* vol. 6, no. 10, p. 9118–9124, 2012.

[10] M. Bozzi, L. Pierantoni and S. Bellucci, "Applications of Graphene at Microwave Frequencies," *RADIOENGINEERING,* vol. 24, no. 3, pp. 661-669, 2015.

[11] A. A. Pesetski, J. E. Baumgardnera, E. Folk, J. X. Przybysz, J. D. Adam and H. Zhang, "Carbon nanotube field-effect transistor operation at microwave frequencies," *Applied Physics Letters,* vol. 88, p. 113103, 2006.

[12] N. Meng, J. F. Fernandez, O. Lancry, E. Pichonat, D. Vignaud, G. Dambrine and H. Happy, "RF characterization of epitaxial graphene nano ribbon field effect transistor," in *IEEE MTT-S International Microwave Symposium*, Baltimore (MD, USA), 2011.

[13] M. Dragoman, D. Neculoiu, Alina-Cristina, A.-C. Bunea, G. Deligeorgis, M. Aldrigo, D. Vasilache, A. Dinescu, G. Konstantinidis, D. Mencarelli, L. Pierantoni and M. Modreanu, "A tunable microwave slot antenna based on graphene," *Applied Physics Letters,* vol. 106, no. 15, p. 153101, 2015.

[14] M. Yasir, P. Savi, S. Bistarelli, A. Cataldo, M. Bozzi, L. Perregrini and S. Bellucci, "A Planar Antenna With Voltage-Controlled Frequency Tuning Based on Few-Layer Graphene," *IEEE Antennas and Wireless Propagation Letters,* vol. 16, no. 1, pp. 2380-2383, 2017.

[15] L. Pierantoni, D. Mencarelli, M. Bozzi, R. Moro, S. Moscato, L. Perregrini, F. Micciulla, A. Cataldo and S. Bellucci, "Broadband Microwave Attenuator Based on Few Layer Graphene Flakes," *IEEE Transactions on Microwave Theory and Techniques*, vol. 63, no. 8, p. 2491, 2015.

[16] S. Bellucci, F. Micciulla, V. M. Levin, Y. S. Petronyuk, L. A. Chernozatonskii, P. P. Kuzhir, A. G. Paddubskaya, J. Macutkevic, M. A. Pletnev, V. Fierro and A. Celzard , "Microstructure, elastic and electromagnetic properties of epoxy-graphite composites," *AIP Advances,*, vol. 5, p. 067137, 2015.

[17] M. Dragoman and D. Dragoman, 2D Nanoelectronics; Physics and Devices of Atomically Thin Materials, 6330 Cham, Switzerland: Springer International Publishing AG, 2017.

[18] L. Changgu, W. Xiaoding, W. K. Jeffrey and J. Hone, "Measurement of the elastic properties and intrinsic strength of monolayer graphene.," *Science*, vol. 321, no. 5887, pp. 385-388, 2008.

[19] A. A. Balandin, S. Ghosh, W. Bao, I. Calizo, D. Teweldebrhan, F. Miao and C. N. Lau, "Superior thermal conductivity of single-layer graphene.," *Nano Lett.*, vol. 8, no. 3, pp. 902-907, 2008.

[20] B. Sukang, K. Hyeongkeun, L. Youngbin, X. Xiangfan, P. Jae-Sung, Y. Zheng, B. Jayakumar, L. Tian, K. R. Hye, S. I. Young, K. Young-Jin, K. S. Kwang,

Ö. Barbaros, A. Jong-Hyun, H. H. Byung and S. Iijima, "Roll-to-roll production of 30-inch graphene films for transparent electrodes," *Nature Nanotechnology,* vol. 5, pp. 574-578, 2010.

[21] A. H. Castro Neto, F. Guinea, N. M. R. Peres, K. S. Novoselov and A. K. Geim, "The electronic properties of graphene," *Rev Mod Phys*, vol. 81, p. 109–162, 2009.

[22] K. S. Novoselov, A. K. Geim, S. V. Morozov, D. Jiang, M. I. Katsnelson, I. V. Grigorieva, S. V. Dubonos and A. A. Firsov, "Two-dimensional gas of massless Dirac fermions in graphene," *Nature*, vol. 438, p. 197, 2005.

[23] Y. B. Zhang, Y. W. Tan, H. L. Stormer and P. Kim, "Experimental observation of the quantum Hall effect and Berry's phase in graphene," *Nature*, vol. 438, p. 201, 2005.

[24] A. C. Ferrari and a. et, "Science and technology roadmap for graphene, related two-dimensional crystals, and hybrid systems," *Nanoscale,* vol. 7, p. 4598, 2015.

[25] S. M. Rao, J. J. F. Heitz, T. Roger, N. Westerberg and D. Faccio, "Coherent control of light interaction with graphene," *Optics letters,* vol. 39, no. 18, pp. 5345-5347, 2014.

[26] Z. Sun, A. Martinez and F. Wang, "Optical modulators with 2D layered materials," *Nature Photonics,* vol. 10, p. 227–238, 2016.

[27] A. Tsuneya, Z. Yisong and S. Hidekatsu, "Dynamical Conductivity and Zero-Mode Anomaly in Honeycomb Lattices," *J. Phys. Soc. Jpn.*, vol. 71, pp. 1318-1324, 2002.

[28] B. Sensale-Rodriguez, T. Fang, R. Yan, M. M. Kelly, D. Jena, L. Liu and H. G. Xing, "Unique prospects for graphene-based terahertz modulators," *APPLIED PHYSICS LETTERS*, vol. 99, p. 113104, 2011.

[29] X. He and S. Kim, "Tunable terahertz graphene metamaterials," *Carbon*, vol. 86, p. 229–237, 2015.

[30] A. Tredicucci and M. S. Vitiello, "Device concepts for graphene-based terahertz photonics," *IEEE J. Sel. Top. Quantum Electron,* vol. 20, no. 1, p. 130–138, 2014.

[31] M. Tamagnone, A. Fallahi, J. R. Mosig and J. Perruisseau-Carrier, "Fundamental limits and near-optimal design of graphene modulators and non-reciprocal devices," *Nat. Photonics,* vol. 8, p. 556–563, 2014.

[32] T. Otsuji, V. Popov and V. Ryzhii, "Active graphene plasmonics for terahertz device applications.," *J. Phys. D: Appl. Phys.*, vol. 47, p. 094006, 2014.

[33] P. Y. Chen, H. Huang, D. Akinwande and A. Alù, "Graphene-based plasmonic platform for reconfigurable terahertz nanodevices.," *ACS Photonics*, vol. 1, no. 8, p. 647–654, 2014.

[34] P. Y. Chen and A. Alu, "Terahertz metamaterial devices based on graphene nanostructures," *IEEE Trans. Terahertz Sci. Technol.*, vol. 3, no. 6, p. 748–756, 2013.

[35] S. H. Lee, H. D. Kim, H. J. Choi, B. Kang, Y. R. Cho and B. Min, "Broadband modulation of terahertz waves with non-resonant graphene meta-devices," *IEEE Trans. Terahertz Sci. Technol.*, vol. 3, no. 6, p. 764–771, 2013.

[36] L. Ju, B. Geng, J. Horng, C. Girit, M. Martin, Z. Hao, H. A. Bechtel, X. Liang, A. Zettl, Y. R. Shen and F. Wang, "Graphene plasmonics for tunable terahertz metamaterials,," *Nature Nanotechnol.,* vol. 6, p. 630–634, 2011.

[37] B. Sensale-Rodriguez, R. Yan, M. Zhu, D. Jena, L. Liu and H. G. Xing, "Efficient terahertz electro-absorption modulation employing graphene plasmonic structures.," *Appl. Phys. Lett.*, vol. 101, no. 26, p. 261115, 2012.

[38] S. F. Shi, B. Zeng, H. L. Han, X. Hong, H. Z. Tsai, H. S. Jung, A. Zettl, M. F. Crommie and F. Wang, "Optimizing broadband terahertz modulation with hybrid graphene/metasurface structures," *Nano Lett.*, vol. 15, no. 1, p. 372–377, 2015.

[39] A. Novitsky, A. M. Ivinskaya, M. Zalkovskij, R. Malureanu, P. U. Jepsen and A. V. Lavrinenko, "Non-resonant terahertz field enhancement in periodically arranged nanoslits.," *J. Appl. Phys.,* vol. 112, p. 074318, 2012.

[40] Q.-Y. Wen, W. Tian, Q. Mao, Z. Chen, W.-W. Liu, Q.-H. Yang, M. Sanderson and H.-W. Zhang, "Graphene based all-optical spatial terahertz modulator," *Sci Rep.*, vol. 4, p. 7409, 2014.

[41] G. Liang, X. Hu, X. Yu, Y. Shen, L. H. Li, A. G. Davies, E. H. Linfield, H. K. Liang, Y. Zhang, S. F. Yu and Q. J. Wang, "Integrated Terahertz Graphene Modulator with 100% Modulation," *ACS Photonics*, vol. 2, p. 1559−1566, 2015.

[42] S. H. Lee, M. Choi, T.-T. Kim, S. Lee, M. Liu, X. Yin, H. K. Choi, S. S. Lee, C.-G. Choi, S.-Y. Choi, X. Zhang and B. Min, "Switching terahertz waves with gate-controlled active graphene metamaterials," *Nature Mater.,* vol. 11, p. 936–941, 2012.

[43] Q. Li, Z. Tian, X. Zhang, R. Singh, L. Du, J. Gu, J. Han and W. Zhang, "Active graphene–silicon hybrid diode for terahertz," *Nature Communications,* vol. 6, p. 7082, 2015.

[44] B. Vasić, M. M. Jakovljević, G. Isić and R. Gajić, "Tunable metamaterials based on split ring resonators and doped graphene," *Appl. Phys. Lett.,* vol. 103, p. 011102, 2013.

[45] H. T. Chen, W. J. Padilla, M. J. Cich, A. K. Azad, R. D. Averitt and J. T. Antoinette, "A metamaterial solid-state terahertz phase modulator," *Nat. Photonics,* vol. 3, p. 148, 2009.

[46] P. Y. Chen, C. Argyropoulos and A. Alu, "Terahertz antenna phase shifters using integrally-gated graphene transmission-lines," *IEEE Trans. Antennas and Propagation,* vol. 61, no. 4, p. 1528–1537, 2013.

[47] R. R. Nair, P. Blake, A. N. Grigorenko, K. S. Novoselov, T. J. Booth, T. Stauber, N. M. Peres and A. K. Geim, "Fine structure constant defines visual transparency of graphene," *Science,* vol. 320, no. 5881, p. 1308, 2008.

[48] V. Ryzhii, A. A. Dubinov, T. Otsuji, V. Mitin and M. S. Shur, "Terahertz lasers based on optically pumped multiple graphene structures with slot-line and dielectric waveguides.," *J. Appl. Phys.,* vol. 107, p. 054505, 2010.

[49] T. Watanabe, T. Fukushima, Y. Yabe, S. A. Tombet, A. Satou, A. A. Dubinov, V. Y. Aleshkin, V. Mitin, V. Ryzhii and T. Otsuji, "The gain enhancement effect of surface plasmon polaritons on terahertz stimulated emission in optically pumped monolayer graphene," *New J. Phys.,* vol. 15, no. 7, p. 075003, 2013.

[50] V. Ryzhii, M. Ryzhii, V. Mitin and T. Otsuji, "Toward the creation of terahertz graphene injection laser.," *J. Appl. Phys.,* vol. 110, p. 094503, 2011.

[51] L. Prechtel, L. Song, D. Schuh, P. Ajayan, W. Wegscheider and A. W. Holleitner, "Time-resolved ultrafast photocurrents and terahertz generation in freely suspended graphene," *Nature Commun.,* vol. 3, p. 646, 2012.

[52] M. Dyakonov and M. Shur, "Shallow water analogy for a ballistic field effect transistor: New mechanism of plasma wave generation by dc current," *Phys. Rev. Lett.*, vol. 71, p. 2465, 1993.

[53] A. N. Grigorenko, M. Polini and K. S. Novoselov, "Graphene plasmonics," *Nature Photon.*, vol. 6, p. 749–758., 2012.

[54] L. Britnell, R. V. Gorbachev, A. K. Geim, L. A. Ponomarenko, A. Mishchenko, M. T. Greenaway, T. M. Fromhold, K. S. Novoselov and L. Eaves, "Resonant tunnelling and negative differential conductance in graphene transistors," *Nature Commun.*, vol. 4, pp. 1794-1-5, 2013.

[55] V. Ryzhii, T. Otsuji, V. Y. Aleshkin, A. A. Dubinov, M. Ryzhii, V. Mitin and M. S. Shur, "Voltage-tunable terahertz and infrared photodetectors based on double graphene-layer structures," *Appl. Phys. Lett.*, vol. 104, p. 163505, 2014.

[56] L. Vicarelli, M. S. Vitiello, D. Coquillat, A. Lombardo, A. C. Ferrari, W. Knap, M. Polini, V. Pellegrini and A. Tredicucci, "Graphene field-effect transistors as room-temperature terahertz detectors," *Nature Mater.*, vol. 11, p. 865–871, 2012.

[57] J. Yan, M.-H. Kim, J. A. Elle, A. B. Sushkov, G. S. Jenkins, H. M. Milchberg, M. S. Fuhrer and H. D. Drew, "Dual-gated bilayer graphene hot-electron bolometer," *Nature Nanotechnol.*, vol. 7, p. 472–478, 2012.

[58] X. Cai, A. B. Sushkov, R. J. Suess, M. M. Jadidi, G. S. Jenkins, L. O. Nyakiti, R. L. Myers-Ward, S. Li, J. Yan, D. K. Gaskill, T. E. Murphy, H. D. Drew and M. S. Fuhrer, "Sensitive room-temperature terahertz detection via the photothermoelectric effect in graphene," *Nature Nanotechnol.*, vol. 9, p. 814–819, 2014.

[59] V. P. Gusynin, S. G. Sharapov and J. P. Carbotte, "On the universal ac optical background in graphene," *New Journal of Physics*, vol. 11, p. 095013, 2009.

[60] J. S. Moon, D. Curtis, M. Hu, D. Wong, C. McGuire, P. M. Campbell, G. Jernigan, J. L. Tedesco, B. VanMill, R. Myers-Ward, C. Eddy and J. K. Gaskill, "Epitaxial-Graphene RF Field-Effect Transistors on Si-Face 6H-SiC Substrates," *IEEE Electron Device Letters*, vol. 30, no. 6, pp. 650-652, 2009.

[61] Y. Lin, K. A. Jenkins, A. Valdes-Garcia, J. P. Small, D. B. Farmer and P. Avouris, "Operation of Graphene Transistors at Gigahertz Frequencies," *Nano Lett.*, vol. 9, no. 1, pp. 422-426, 2009.

[62] F. Schwierz, "Graphene transistors," *Nature nanotechnology*, vol. 5, pp. 487-496, 2010.

[63] Y. M. Lin, C. Dimitrakopoulos, K. A. Jenkins, D. B. Farmer, H. Y. Chiu, A. Grill and P. Avouris, "100-GHz transistors from wafer-scale epitaxial graphene," *Science*, vol. 327, p. 662, 2010.

[64] L. Liao, Y. C. Lin, M. Bao, R. Cheng, J. Bai, Y. Liu, Y. Qu, K. L. Wang, Y. Huang and X. Duan, "High-speed graphene transistors with a self-aligned nanowire gate," *Nature*, vol. 467, pp. 305-308, 2010.

[65] D. Mencarelli, M. Dragoman, L. Pierantoni, T. Rozzi and F. Coccetti, "Design of a coplanar graphene-based nano-patch antenna for microwave applications.," in *International Microwave Symposium*, Seattle (WA, USA), 2013.

[66] K. Batrakov, P. Kuzhir, S. Maksimenko, A. Paddubskaya, S. Voronovich, P. Lambin, T. Kaplas and Y. Svirko, "Flexible transparent graphene/polymer multilayers for efficient electromagnetic field absorption," *Scientific Reports*, vol. 4, p. 7191, 2014.

[67] A. Q. Zhang, W. B. Lu, Z. G. Liu, H. Chen and B. H. Huang, "Dynamically Tunable Substrate-Integrated Waveguide Attenuator Using Graphene.," *IEEE Transactions on Microwave Theory and Techniques*, vol. 66, no. 6, pp. 3081-3089, 2018.

[68] A. Dabrowska, S. Bellucci, A. Cataldo, F. Micciulla and A. Huczko, "Nanocomposites of epoxy resin with graphene nanoplates and exfoliated graphite: Synthesis and electrical properties," *Phys. Status Solidi*, vol. 251, no. 12, p. 2599–2602, 2014.

[69] M. Yasir, S. Bistarelli, A. Cataldo, M. Bozzi, L. Perregrini and S. Bellucci, "Enhanced Tunable Microstrip Attenuator Based on Few Layer Graphene Flakes," *IEEE Microwave and Wireless Component Letters*, vol. 27, no. 4, pp. 332-334, 2017.

[70] M. Yasir, S. Bistarelli, A. Cataldo, M. Bozzi, L. Perregrini and S. Bellucci, "Tunable and input-matched attenuator based on few-layer graphene," in *47th European Microwave Conference (EuMC)*, Nuremberg, Germany, 2017.

[71] W. Hu, D. Zhang, M. J. Lancaster, T. W. Button and B. Su, "Investigation of Ferroelectric Thick-Film Varactors for Microwave Phase Shifters," *IEEE*

Transactions on Microwave Theory and Techniques, vol. 55, no. 2, pp. 418-424, 2007.

[72] M. Haghzadeh, C. Armiento and A. Akyurtlu, "All-Printed Flexible Microwave Varactors and Phase Shifters Based on a Tunable BST/Polymer," *IEEE Transactions on Microwave Theory and Techniques,* vol. 65, no. 6, pp. 2030-2042, 2017.

[73] M. Dragoman, M. Modreanu, I. M. Povey, S. Iordanescu, M. Aldrigo, C. Romanit, D. Vasilache, A. Dinescu and D. Dragoman, "Very large phase shift of microwave signals in a 6 nm HfxZr1-xO2 ferroelectric at ±3V," *Nanotech,* vol. 28, p. 38LT04, 2017.

[74] M. Dragoman, G. Deligeorgis, A. Muller, A. Cismaru, D. Neculoiu, G. Konstantinidis, D. Dragoman, A. Dinescu and F. Comanescu, "Millimeter wave Schottky diode on graphene monolayer via asymmetric metal contacts," *J. Appl. Phys.,* vol. 112, p. 084302, 2012.

[75] A. Maffucci, F. Micciulla, A. Cataldo, G. Miano and S. Bellucci, "Bottom-up realization and electrical characterization of a graphene-based device," *Nanotechnology,* vol. 27, p. 095204, 2016.

[76] Y. Jiang, X. Q. Lin, B. Wang and C. Tang, "Theoretical analysis and design of a compact analogue phase shifter with constant low insertion loss," *Electron. Lett.,* vol. 54, no. 8, pp. 517-519, 2018.

[77] J. Costantine, Y. Tawk, S. E. Barbin and C. G. Christodoulou, "Reconfigurable Antennas: Design and Applications," *Proceedings of the IEEE,* vol. 103, no. 3, pp. 424-437, 2015.

[78] K. Naishadham, "An investigation on the tuning of a microstrip patch antenna using carbon nanotube thin films," in *IEEE Antennas Propagation Symposium (APS 2014),* Memphis, USA, 2014.

[79] P. Savi, K. Naishadham, A. Bayat, M. Giorcelli and S. Quaranta, "Multi-Walled Carbon Nanotube Thin Film Loading for Tuning Microstrip Patch Antennas," in *10th European Conference on Antennas (EuCAP),* Davos, Switzerland, 2016.

[80] C. Nunez-Alvarez, R. Cheung and J. Thompson, "Performance Analysis of Hybrid Metal-Graphene Frequency Reconfigurable Antennas for the Microwave

Regime," *IEEE Transactions on Antennas and Propagation,* vol. 65, no. 4, pp. 1558 - 1569, 2017.

[81] S. Vishwakarma, V. Ummalaneni, M. Iqbal, A. Majumdar and S. Ram, "Mitigation of through-wall interference in radar images using denoising autoencoders," in *2018 IEEE Radar Conference (RadarConf18)*, 2018.

[82] S. K. Yong and C. C. Chong, "An overview of multigigabit wireless through millimeter wave technology: Potentials and technical challenges," *EURASIP Journal on Wireless Communications and Networking,* vol. 2007, p. 078907, 2006.

[83] D. Bandyopadhyay and J. Sen, "Internet of things: Applications and challenges in technology and standardization," *Wireless Pers. Commun.,* vol. 58, no. 1, p. 49–69, 2011.

[84] O. Galinina, h. Tabassum, K. Mikhaylov, K. Andreev, E. Hossain and Y. Koucheryavy, "On feasibility of 5G-grade dedicated RF charging technology for wireless-powered wearables," *IEEE Wireless Communications,* vol. 23, no. 2, p. 28–37, 2016.

[85] A. Costanzo and D. Masotti, "Energizing 5G: Near- and Far-Field Wireless Energy and Data Transfer as an Enabling Technology for the 5G IoT," *IEEE Microwave Magazine,* vol. 18, no. 3, p. 125–136, 2017.

[86] G. Moddel and S. Grover, Rectenna Solar Cells, New York: Springer, 2013.

[87] T. Oishi, N. Kawano and S. Masuya, "Diamond Schottky Barrier Diodes With NO2 Exposed Surface and RF-DC Conversion Toward High Power Rectenna," *IEEE Trans. Electron Dev. Lett.,* vol. 38, no. 1, p. 87–90, 2017.

[88] M. Dragoman and M. Aldrigo, "Graphene rectenna for efficient energy harvesting at terahertz frequencies," *Appl. Phys. Lett.,* vol. 109, p. 113105 , 2016.

[89] P. Sangaré, G. Ducournau, B. Grimbert, V. Brandli, M. Faucher, C. Gaquière, A. Íñiguez-de-la-Torre, I. Íñiguez-de-la-Torre, J. F. Millithaler, J. Mateos and T. González, "Experimental demonstration of direct terahertz detection at room temperature in AlGaN/GaN assymmetric nanochannels," *J. Appl. Phys.,* vol. 113, p. 093116, 2013.

[90] A. Westlund, M. Winters, I. G. Ivanov, J. Hassan, P. -Å. Nilsson, E. Janzén, N. Rorsman and J. Grahn, "Graphene self-switching diodes as zero-bias microwave detectors," *J. Appl. Phys.,* vol. 106, p. 093116 , 2015.

[91] M. Winters, M. Thorsell, W. Strupiński and N. Rorsman, "High frequency electromagnetic detection by nonlinear conduction modulation in graphene nanowire diodes," *J. Appl. Phys.*, vol. 107, p. 143508 , 2015.

[92] S. Bhatnagar, R. Kumar, M. Sharma and B. K. Kuanr, "Reduced graphene Oxide/ZnO nanostructures based rectifier diode," *AIP Conference Proc.*, vol. 1832, p. 050060, 2017.

[93] C. Balocco, a. M. Song, M. Åberg, A. Forchel, T. González‖, J. Mateos, I. Maximov, M. Missous, A. A. Rezazadeh, J. Saijets, L. Samuelson, D. Wallin, K. Williams, L. Worschech and H. Q. Xu, "Microwave Detection at 110 GHz by Nanowires with Broken Symmetry," *Nano Lett.*, vol. 5, no. 7, pp. 1423-1427, 2005.

[94] A. Westlund, P. Sangaré, G. Ducournau, P. -Å. Nilsson, C. Gaquière, L. Desplanque, X. Wallart and J. Grahn, "Terahertz detection in zero-bias InAs self-switching diodes at room temperature," *Appl. Phys. Lett.*, vol. 103, p. 133504, 2013.

[95] A. Westlund, P. Sangaré, G. Ducournau, I. Iñiguez-de-la-Torre, P. -. Å. Nilsson, C. Gaquière, L. Desplanque and X. Wallart, "Optimization and Small-Signal Modeling of Zero-Bias InAs Self-Switching Diode Detectors," *Solid-State Electronics*, vol. 104, pp. 79-85, 2015.

[96] A. Westlund, I. Iñiguez-de-la-Torre, P. -Å. Nilsson, T. González, J. Mateos, P. Sangaré, G. Ducournau, C. Gaquière, L. Desplanque, X. Wallart and J. Grahn, "On the effect of δ-doping in self-switching diodes," *Appl. Phys. Lett.*, vol. 105, p. 093505 , 2014.

[97] S. Hanson, M. Seok, Y. -S. Lin, Z. Foo, D. Kim, Y. Lee, N. Liu, D. Sylvester and D. Blaauw, "A low-voltage processor for sensing applications with picowatt standby mode," *IEEE J. Solid-State Circuits*, vol. 44, p. 145–154, 2009.

[98] H. Jayakumar, K. Lee, W. S. Lee, A. Raha, Y. Kim and V. Raghunathan, "Powering the internet of things," in *Proc. of the 2014, International Symposium on Low Power Electronics and Design (ISLPED)* , 2014.

[99] B. Sensale-Rodriguez, R. Yan, S. Rafique, M. Zhu, W. Li, X. Liang, D. Gundlach, V. Protasenko, M. M. Kelly, D. Jena, L. Liu and H. G. Xing, "Extraordinary control of terahertz beam reflectance in graphene electro-absorption modulators," *Nano Lett.*, vol. 12, no. 9, p. 4518–4522, 2012.